Physics Reports 501 (2011) 1–74

Contents lists available at ScienceDirect

Physics Reports

journal homepage: www.elsevier.com/locate/physrep

Map-based models in neuronal dynamics

B. Ibarz [a], J.M. Casado [b], M.A.F. Sanjuán [c,*]

[a] Center for Neural Science, New York University, New York, NY 10003, USA
[b] Area de Física Teórica, Universidad de Sevilla, E-41080 Sevilla, Spain
[c] Departamento de Física, Universidad Rey Juan Carlos, E-28933 Móstoles, Madrid, Spain

ARTICLE INFO

Article history:
Accepted 16 December 2010
Available online 24 December 2010
editor: M.L. Klein

Keywords:
Map-based
Discrete-time
Neuron models
Neural networks
Nonlinear dynamics

ABSTRACT

Ever since the pioneering work of Hodgkin and Huxley, biological neuron models have consisted of ODEs representing the evolution of the transmembrane voltage and the dynamics of ionic conductances. It is only recently that discrete dynamical systems – also known as maps – have begun to receive attention as valid phenomenological neuron models. The present review tries to provide a coherent perspective of map-based biological neuron models, describing their dynamical properties; stressing the similarities and differences, both among them and in relation to continuous-time models; exploring their behavior in networks; and examining their wide-ranging possibilities of application in computational neuroscience.

Contents

1. Introduction 2
   1.1. Modeling in neuroscience 2
   1.2. Map-based versus ODE-based models 6
2. Map-based neuron models 8
   2.1. Two-dimensional, fast–slow, spiking–bursting models 8
      2.1.1. The Izhikevich model 10
      2.1.2. The Rulkov model 12
      2.1.3. The Courbage–Nekorkin–Vdovin (CNV) model 15
      2.1.4. The Chialvo model 17
   2.2. One-dimensional bursters 18
   2.3. The Nagumo–Sato and Aihara models 19
   2.4. The netlet model 22
3. Dynamic properties of isolated map-based neuron models 23
   3.1. Bursting and adaptation 23
   3.2. Resonance, oscillations, and the integrator versus resonator trade-off 28
   3.3. Chaos 31
   3.4. Stochastic coherence and stochastic resonance 35
4. Network behavior of map-based neuron models 38
   4.1. Synchronization of spiking map-based neurons 38
   4.2. Synchronization of bursts 43
   4.3. Interplay between network topology and dynamics 50
5. Modeling with map-based neurons 58

* Corresponding author.
E-mail addresses: borja.ibarz@nyu.edu (B. Ibarz), casado@us.es (J.M. Casado), miguel.sanjuan@urjc.es (M.A.F. Sanjuán).

0370-1573/$ – see front matter © 2010 Elsevier B.V. All rights reserved.
doi:10.1016/j.physrep.2010.12.003

5.1. Fitting the models to real neurons ... 58
5.2. Modeling learning and behavior ... 61
5.3. Modeling cognitive processes ... 68
6. Summary and conclusion ... 70
Acknowledgements ... 71
References ... 71

1. Introduction

Neurons, the basic elements of nervous systems, are highly structured and complex cells. Their elementary constituents and processes have been studied for more than a century, and, although many important details remain to be pinned down, enough understanding has been gained to build mathematical models that closely agree with their observed behavior [1–5].

As with any other macroscopic physical system, a natural mathematical model for a neuron is a field of real-valued properties (for example, membrane voltage) extended over space and time, ruled by a set of partial differential equations (PDEs). However, computational, analytical and theoretical factors can make discretization advisable.

- Discretization in *space* is common practice in computational neuroscience. The neuron is divided up into a finite number of compartments, and the PDEs turn into sets of ordinary differential equations (ODEs). ODE-based biological neuron models have been the standard since the ground-breaking work of Hodgkin and Huxley [6].
- Discretization in *time* transforms the ODEs into discrete dynamical systems, or maps. The state is updated in steps corresponding to finite time intervals. It is this type of discretization that distinguishes the models which are the object of the present review.
- Discretization of the *field values* makes sense once space and time have been discretized. The resulting model is a finite-state automaton.

Discrete-time models have a long tradition in the physics of complex systems [7–11], and in the field of artificial neural networks [12], but it is only recently that they have begun to receive attention as valid models of biological neurons. This review is concerned with map-based, biological neuronal models. The rest of this introductory section provides a basic background on neuron modeling, and some context that will be helpful to those more familiar with the ODE-based formulation.

1.1. Modeling in neuroscience

Fig. 1 is a cartoon of the procedure to build a fairly detailed neuron model. Measurements of electrical properties, such as membrane conductance and time constant, are carried out at the soma and at selected points of dendrites and axon, whose detailed arborizing geometry can be semi-automatically traced [13,14]. Genetic, pharmacological and immunohistochemical probes help determine the distribution of different kinds of channel proteins [15], whose behavior can be studied by means of single-channel recording [16]. With all these data in hand, the cell is divided into a number of compartments small enough to be considered electrically homogeneous, each compartment modeled as a lumped-element circuit, where (nonlinear) resistors, capacitors and sources account for membrane and channel properties; additional variables for ion concentrations may control these elements. Accurate models of synapses can also be easily integrated in this scheme to build networks. The popular neuronal simulation software packages NEURON [17] and GENESIS [18] are based on this bottom-up methodology.

The merits of detailed neuron models cannot be exaggerated. However, it is not always true that the more detail we put into a model the better answers we get from it. The main shortcomings of this approach are:

- It is not possible to actually measure all the parameters involved in a model with hundreds of compartments. Usually parameters are set blindly around reasonable values obtained from particular neurons under particular experimental conditions, or guessed from indirect evidence.
- The model can be just as hard to understand as the real system. With a one-to-one correspondence between real neuron and model components, no insight is gained into general principles of neural function.
- The level of detail has to be limited anyway at some point. The cellular-level model might need to be turned subcellular or molecular, and include organelles, genetic expression and extracellular medium dynamics. Processes with time scales differing in several orders of magnitude might need to be simulated. Many simplifying assumptions are inevitable.
- The computational requirements are very high.

For all the above reasons, a complementary approach is often used: build simple models that do away with inessential details and retain only the relevant functionality of the neuron. One of the features that is most frequently dropped is geometry; this leads to conductance models with a single or very few compartments. The spatial structure of the neuron is replaced by a dimensionless system with a single value of membrane voltage, and a topology of connections, possibly including delays, that reflects the actual distribution of synapses. The form of the single compartment equations is worth

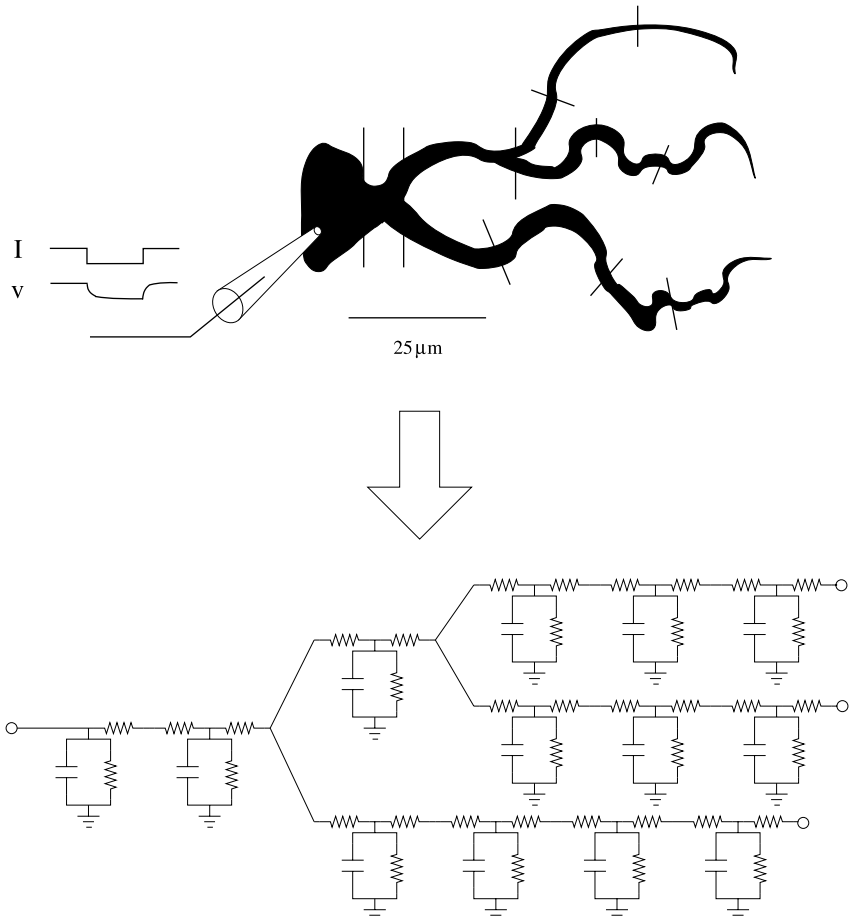

Fig. 1. Modeling a neuron. Electrical, chemical and morphological properties are measured. The neuron is then divided up into small compartments, and the measured or inferred properties of each compartment are translated into standard conductance models (in the figure, only the simplest passive properties are represented). Alternatively, cable models with spatially varying parameters may be used. Inspired by [18].

looking at, since it helps understand the origin of the models which are the object of this review. Typical equations for these so-called Hodgkin–Huxley-type models are [3]:

$$c_m \frac{dv}{dt} = -g_L(v - E_L) + \sum_j I_{m,j} + \sum_j I_{\text{syn},j}, \tag{1}$$

where $v(t)$ is membrane voltage, c_m represents membrane capacitance, g_L is the passive conductance of leak currents with reversal potential E_L, and $I_{m,j}$ and $I_{\text{syn},j}$ are intrinsic membrane currents and synaptic currents, respectively; all of them per unit area. These currents follow equations of the form:

$$I_j = -g_{\max,j} m_j^{M_j} h_j^{H_j} (v - E_{r,j}), \tag{2}$$

where $g_{\max,j}$ is the maximal conductance for the given current, m_j and h_j are dynamic variables for the activation and inactivation of the channels that allow it to flow, constant exponents M_j and H_j depend on the number of subunits regulating activation and inactivation, and $E_{r,j}$ is the reversal potential associated with the particular ion or ions that make up the current. The equations for the dynamics of m_j and h_j come from either deterministic or stochastic reaction schemes with transition rates or probabilities that depend on voltage, ionic concentrations, and, in the case of synaptic currents, neurotransmitter concentrations.

An example of what can be achieved with these models in a modest desktop computer is shown in Fig. 2, where 10 s of the activity of 4 out of 225 cells of a network that models thalamo-cortical interaction [19] are represented. The model consists of four layers, each containing a different type of neuron (thalamic relay, reticular, pyramidal and interneurons). Each neuron has an average of 10 variables and connects to an average of 30 other neurons. The simulation took half an hour to run in a 2 GHz computer with an integration time step of 0.01 ms. In spite of its simplicity, the model reproduces typical oscillatory rhythms in the sleep–wake transition and is useful in assessing the effects of modulators and anesthetics on the thalamo-cortical system [20].

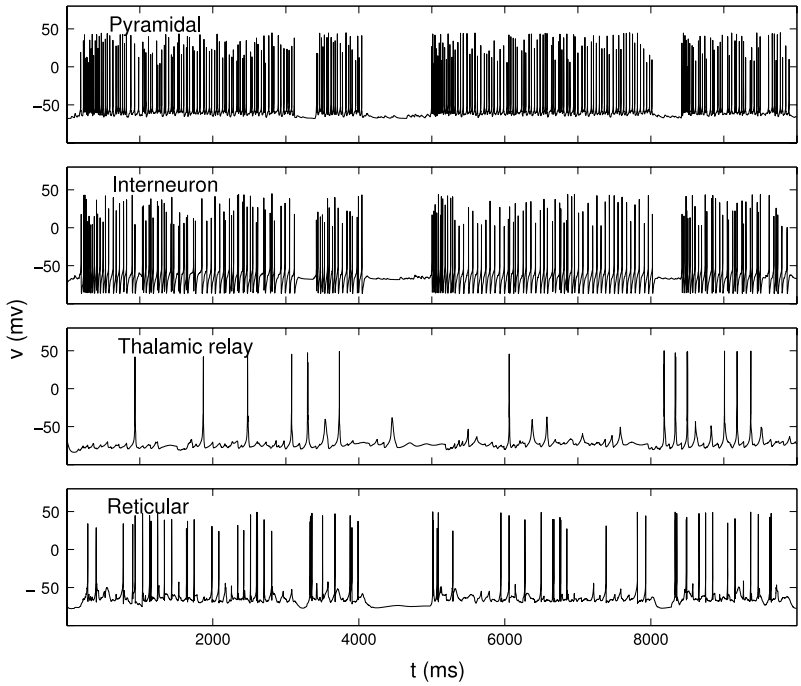

Fig. 2. Time evolution of the membrane voltage of four different kinds of conductance-based, single-compartment (for reticular and thalamic relay cells) or double-compartment (for interneurons and pyramidal cells) models, part of a 225-neuron toy model of the thalamo-cortical system [19].

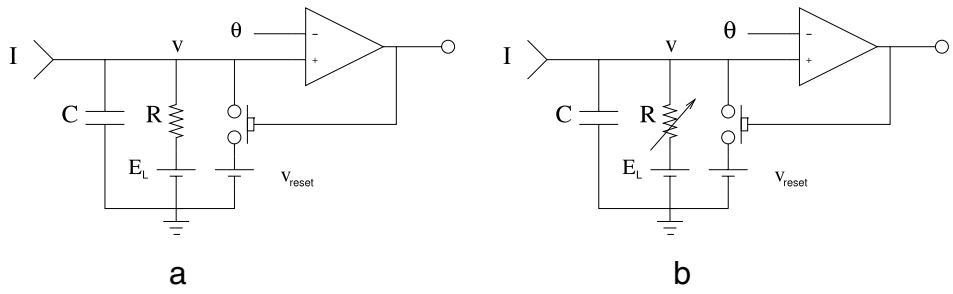

Fig. 3. Equivalent circuits of (a) the leaky integrate-and-fire (LIF) model, and (b) the nonlinear leaky integrate-and-fire model. They only differ in the linear or nonlinear character of the discharge resistor.

But even this degree of simplification is not enough for many purposes. In networks such as the one that produced Fig. 2 it is very hard to estimate the correct values of most parameters, as even slight variations produce very noticeable changes in the firing rhythms. Besides, the simulation of thousands of these neurons still calls for a supercomputer.

Therefore further simplification may be called for, which is what the integrate-and-fire family of models, and particularly its most popular member, the leaky integrate-and-fire (LIF) model, provides [2]. This model is still conductance-based, but it dispenses with all variables except membrane voltage. In fact, the cell membrane behaves precisely as a capacitor that passively discharges through a resistor, representing the ionic channels, and may be charged by external currents (synaptic events, for example). The key to the neuroscientific interest of the model is its threshold-and-reset mechanism: if voltage reaches a threshold value θ, the capacitor instantaneously discharges to a reset level v_{reset} and the neuron is said to have fired a spike. Thus the action potential, for the sake of which at least three dynamic variables are necessary in the Hodgkin–Huxley models of Eq. (1), is represented as a point event. This is a reasonable simplification, since the action potential is considered a stereotyped response in most contexts.

An electric circuit equivalent to the LIF model, according to the previous description, is depicted in Fig. 3(a). Its equations are:

$$\begin{aligned} &\tau \dot{v}(t) = -(v(t) - E_L) + RI, \\ &v(t^+) = v_{\text{reset}} \quad \text{if } v(t^-) = \theta. \end{aligned} \tag{3}$$

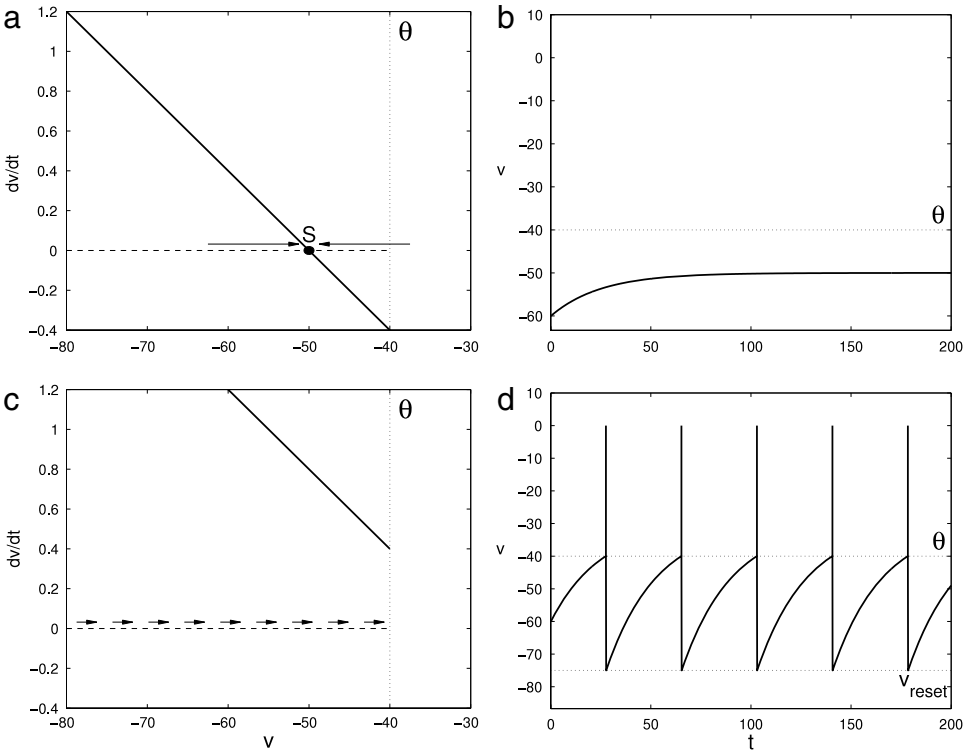

Fig. 4. (a) Phase portrait of the LIF model of Eqs. (3) with $v_{\text{reset}} = -75$, $E_L = -70$, $\theta = -40$, $R = 20$, $\tau = 25$ and $I = 1$. S is the stable equilibrium point. Arrows indicate the direction of the flow. The neuron is in the quiescent, or resting, regime. (b) Voltage trajectory of the system in (a). (c) Same as in (a), but with $I = 2$. The neuron is in the periodic spiking regime. (d) Voltage trajectory of the system in (c) At each reset time, a vertical line has been drawn to mark a spike.

Here $\tau = RC$ is the time constant of the system and, as in Eq. (1), E_L represents the reversal potential of the so-called leak current, which is the voltage level the neuron tends to in the absence of external input I. The model is extremely simple to analyze: it has a globally attracting stable equilibrium point at $v = E_L + RI$, but if it is located beyond θ (that is, if $RI > \theta - E_L$) it effectively disappears due to the threshold mechanism and the system follows a periodic trajectory: the neuron spikes periodically. Phase portraits [21] and trajectories both in the spiking and quiescent regimes are presented in Fig. 4. Observe that voltage and time units are arbitrary, although the particular values of parameters have been selected for v to be in the range of the real membrane potential in millivolts and time in milliseconds.

The model can be significantly improved replacing the discharge resistor by a nonlinear component, as in Fig. 3(b). For example, a resistor with a hyperbolic characteristic $R(V)$ will produce the quadratic integrate-and-fire (QIF) model [2] of equations

$$\begin{aligned} &\tau \dot{v}(t) = k(v(t) - v_r)(v(t) - v_c) + rI, \\ &v(t^+) = v_{\text{reset}} \quad \text{if } v(t^-) = \theta. \end{aligned} \tag{4}$$

The meaning of parameters in these equations is best understood by means of the phase diagrams of Figs. 5(a) and (c). For $I = 0$, two equilibrium points exist: one stable at $v = v_r$, another unstable at $v = v_c$ (supposing $v_r < v_c$ and $k > 0$). If v_{reset} is below v_c, all trajectories will end up at v_r (quiescent state). Notice, however, that in this regime the neuron is *excitable*: if the initial voltage is above v_c (due, for example, to a transitory perturbation) the neuron will produce one spike before going to rest [Fig. 5(b)]. On the other hand, if I grows above the value $I_{sn} = k(v_c - v_r)^2/4r$, both equilibrium points disappear through a saddle–node bifurcation and the neuron begins to spike periodically.

The advantage of nonlinear LIF models over their linear counterparts is tightly linked to the saddle–node bifurcation that allows transition from silence to spiking and vice versa. This bifurcation is the same that can be found in conductance-based models of the type that has come to be known as Type I [22]. These neurons can spike at arbitrarily low frequencies when the external current I is arbitrarily close to the saddle–node value I_{sn}, with frequency growing proportional to $\sqrt{I - I_{sn}}$. These are universal, elementary properties of saddle–node bifurcations [23]. When the voltage passes the bifurcation level, it grows superexponentially toward the spike threshold [compare the upwards convex curves that initiate spikes in Figs. 5(d) or 7(d) to the downwards concave curves of Figs. 4(d) or 6(d)]. The correct modeling of spike initiation has important consequences: while a LIF model with adaptive threshold is able to reproduce, with a precision of 2 ms, 75% of the spikes generated by a real cortical neuron in response to random injected currents, nonlinear IF models, and, in particular, the exponential integrate-and-fire (EIF) model [24], raise this percentage to 90% [25].

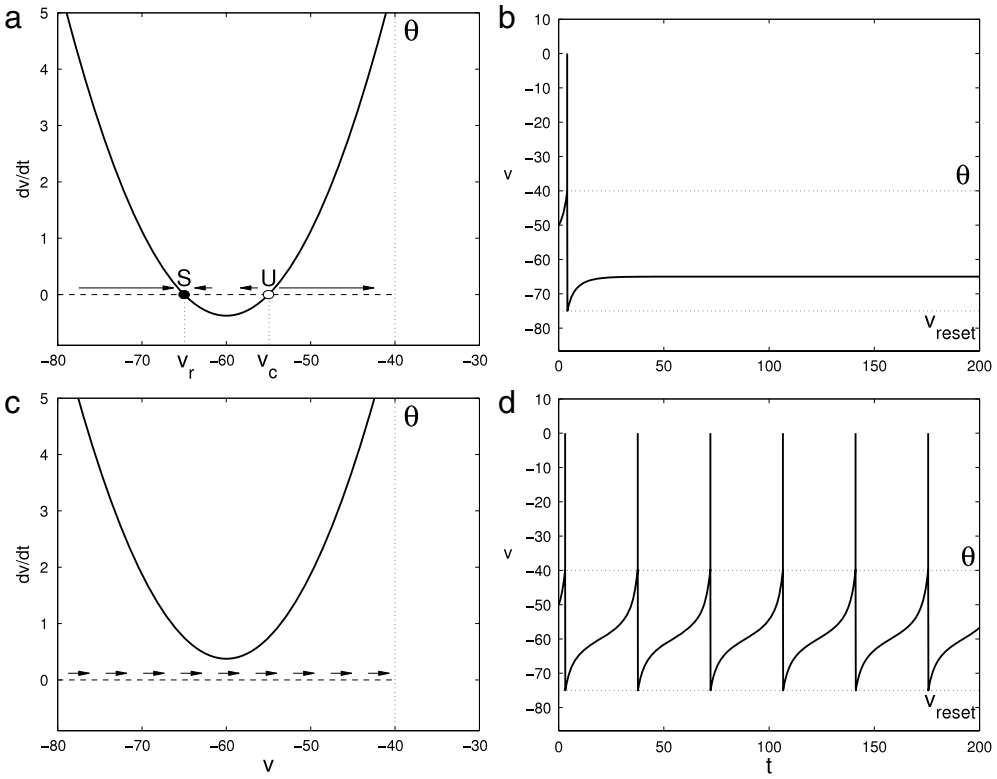

Fig. 5. (a) Phase portrait of the QIF model of Eqs. (4) with $v_{\text{reset}} = -75$, $v_r = -65$, $v_c = -55$, $\theta = -40$, $\tau = 66$, $k = 1$, $r = 25$ and $I = 0$. S is the stable, U the unstable equilibrium point. Arrows indicate the direction of the flow. The neuron is in the quiescent or resting regime. (b) Voltage trajectory of the system in (a). (c) Same as in (a), but with $I = 2$. The neuron is in the periodic spiking regime. (d) Voltage trajectory of the system in (c) At each reset time, a vertical line has been drawn to mark a spike.

Among single neuron models, those in the LIF family are highly abstract. Some of their parameters do not immediately correspond to biophysical properties; they reproduce observed behaviors of neurons while neglecting most of the underlying mechanisms. For this reason they are called *phenomenological*, as opposed to *mechanistic*, or biophysically detailed. The map-based neuron model objects of this review all fall near the phenomenological end of the spectrum.

1.2. Map-based versus ODE-based models

So far we have introduced neuron models described by ordinary differential equations (ODEs). As already mentioned in the introductory remarks, discretization of time in biological neuron modeling is a relatively recent development. The ODEs are substituted by maps, which update the state of the system from one time step to the next.

We can trace the origin of most map-based neuron models to two main sources:

- Event discretization. The action potential, a paradigmatic all-or-nothing event with a duration that is very short compared to the time scale of other neuronal processes, is a natural source of discretization. In some models, such as those of the family that begins with the classical McCulloch–Pitts [26], going through Nagumo–Sato [27,28] and Aihara [29], the only information considered relevant is whether a spike is present or absent during a certain time interval. In some instances [30,31], a map is derived directly by means of a Poincaré section from a continuous-time flow [23], the section being taken at spike initiation. Finally, the threshold-and-reset mechanism of integrate-and-fire models is a form of discretization: the flow of the variables during a spike is ignored, and the state of the system jumps from its pre-spike to its post-spike value. Incorporating this jump in a map-based formulation is straightforward.
- Discretization of ODE-based models through numerical integration. As with any nonlinear system, except in the very few cases where closed-form solutions can be arrived at, ODEs have to be integrated numerically in discrete steps to obtain precise trajectories. Usually, the merits of the resulting map are considered only to discuss the accuracy and convergence of the numerical method. However, in the case of neuron models, the desire to use time steps as big as possible in order to simulate networks of thousands of neurons, together with the above-mentioned natural drive for discretization provided by the action potential, has led modelers to establish the discrete equations on their own as their preferred neuron model. Besides, the map-based formulation has led to variants that could hardly have arisen from integration of an ODE; the chaotic Rulkov model (see Section 2.1.2) is a case in point.

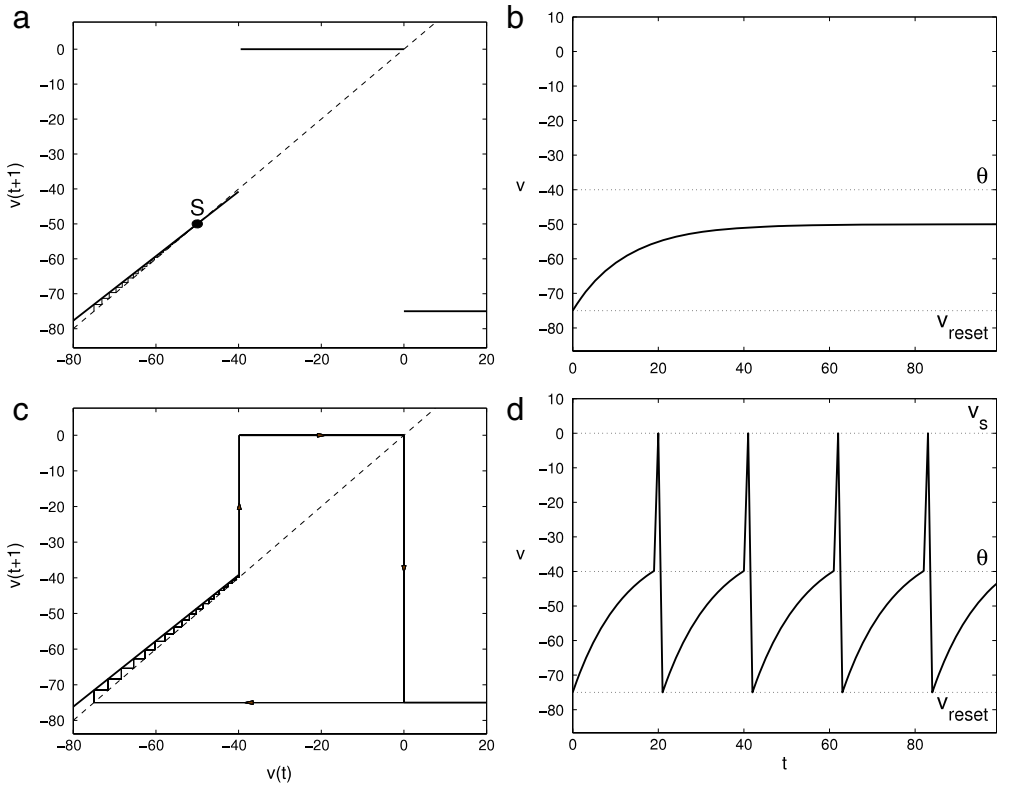

Fig. 6. (a) First return map of the map-based LIF model of Eqs. (5) with the same parameters as in Fig. 4, discretization step $\Delta t = 2$ and spike level $v_s = 0$. S is the stable fixed point. A cobweb of the first 100 samples of the orbit in (b) is superimposed on the diagram. The neuron is in the quiescent or resting regime. (b) Voltage orbit of the system in (a). (c) Same as in (a), but with $I = 2$. The neuron is in the periodic spiking regime. (d) Voltage orbit of the system in (c).

Let us have a close look at some discrete neuron maps that can be derived from the simplest ODE-based models. The LIF neuron introduced in Section 1.1 has a straightforward exact discretization, except for the threshold crossing, which would require a variable reset level to give an accurate correspondence [32]. The discretization yields a map-based model $v(t+1) = F[v(t)]$, where

$$F(v) = \begin{cases} kv + (1-k)(RI + E_L) & \text{if } v < \theta, \\ v_s & \text{if } \theta < v < v_s, \\ v_{\text{reset}} & \text{if } v \geq v_s. \end{cases} \tag{5}$$

Parameter correspondence with the continuous-time model of Eq. (3) is $k = e^{-\frac{\Delta t}{\tau}}$, where Δt is the discretization step. A slight modification with respect to continuous time is that this discrete-time model explicitly represents spikes as a (high) voltage value v_s, and that the spike occupies a finite interval of one time step. Observe that the mapping $F(v)$ includes both the subthreshold linear dynamics and the discontinuous spike generation process; seamless incorporation of threshold and reset mechanisms is a convenient feature of map-based models. First return maps [33,34] and orbits in the spiking and quiescent regimes are presented in Fig. 6. Note how the spikes in Fig. 6(d) are now part of the orbit, occupying one time step, and that the time axis represents discrete time steps. Otherwise, the behavior is indistinguishable from its continuous-time counterpart.

The nonlinear IF model also admits an exact discretization, except for the threshold crossing round-off error, to yield a map $v(t+1) = F[v(t)]$ where

$$F(v) = \begin{cases} f(v) + \mu(v, I) & \text{if } v < \theta, \\ v_s & \text{if } \theta < v < v_s, \\ v_{\text{reset}} & \text{if } v \geq v_s. \end{cases} \tag{6}$$

In this case, $f(v)$ and $\mu(v, I)$ depend in a nontrivial manner on the voltage characteristic of the nonlinear resistor in Fig. 3, but in building discrete-time models it is preferable to use simple forms rather than attempt to match their continuous-time counterparts exactly. Thus, a quadratic $f(v)$ and constant μ produce the map-based QIF model, which as we shall see lies at the heart of several important map-based models. In Fig. 7 its return map and two orbits are depicted. As in the continuous-time case, stability is lost through a saddle–node bifurcation when I grows. In contrast, in the LIF models the fixed point simply vanishes due to threshold crossing.

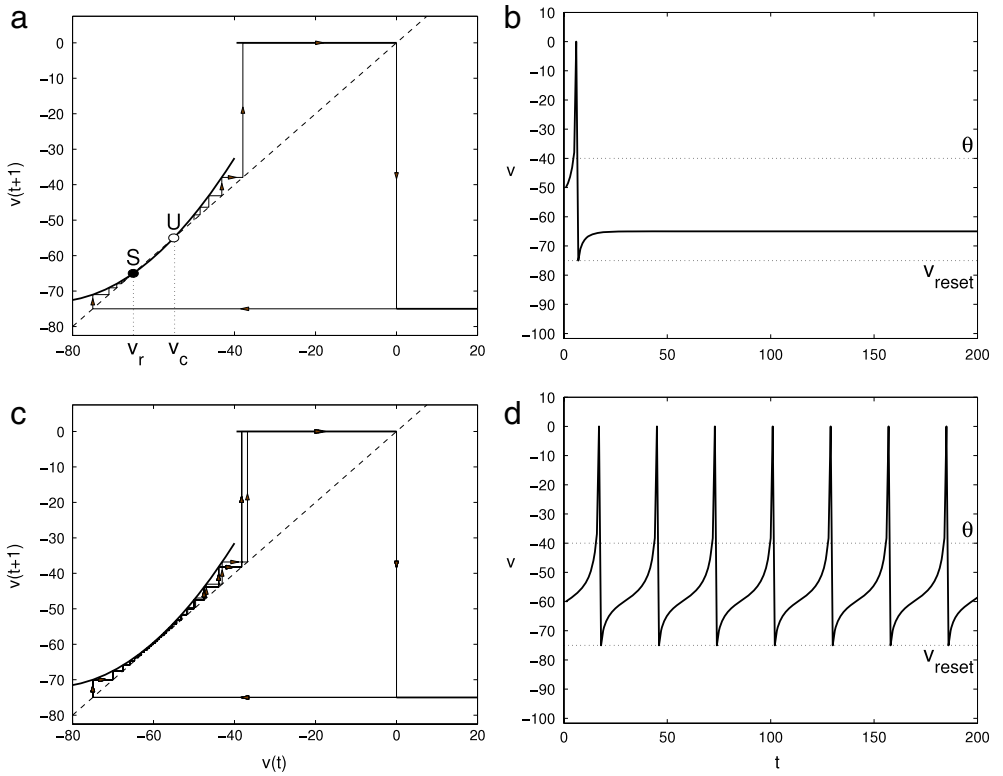

Fig. 7. (a) First return map of the map-based QIF model of Eqs. (6), with $f(v) = v + k(v - v_r)(v - v_c)$ and $\mu(v, I) = I$, $k = 0.02$, $I = 0$ and all other parameters as in Fig. 5. S is the stable, U the unstable fixed point. A cobweb of the first 200 samples of the orbit in (b) is superimposed on the diagram. The neuron is in the quiescent or resting regime. (b) Voltage orbit of the system in (a). (c) Same as in (a), but with $I = 1$. The neuron is in the periodic spiking regime. (d) Voltage orbit of the system in (c).

We have obtained the IF maps by mere numerical integration of the ODE-based models. The feature that gives away that a map-based model is the numerical integration of a continuous-time counterpart is the closeness of its return map to the diagonal; this is evident in the above discretizations, except for the discontinuity due to the threshold-and-reset mechanism. In contrast, intrinsically map-based, 1-D models have first return maps that significantly deviate from the diagonal. As an example, Fig. 8 shows the first return map and an orbit of the chaotic Rulkov neuron model (see Section 2.1.2). A quick comparison with Fig. 7 reveals that in this model the hard threshold-and-reset discontinuity has been replaced by a continuous unimodal return map, which gives rise to chaotic behavior. Other intrinsically map-based models are those proposed by Chialvo [35] (see Section 2.1.4), Courbage et al. [36] (see Section 2.1.3), Cazelles et al. [37], Aguirre et al. [38] (see Section 2.2) and Aihara et al. [29] (see Section 2.3). Discrete maps are less constrained than ODE-based, continuous systems, where oscillations need at least two dimensions, and chaos requires three [23]. In maps (and also hybrid, ODE-based systems with jumps, such as those of the IF family), both features are possible with just one variable. This can be an advantage, in that it provides great flexibility at minimal cost, as the cited models attest; but also a curse when oscillations or chaos are unwanted side-effects, as will be explained in Section 3.3).

2. Map-based neuron models

In this section we shall review the map-based neuron models that have become most popular in recent years. Most derive, to a lesser or greater extent, from the IF family. A particular extension of the IF idea consisting of the addition of a second, slow variable to regulate the voltage dynamics has proven particularly useful for modeling purposes, and we devote Section 2.1 to discuss its variants. We have considered it helpful to begin with the models that are closest to the well-known, ODE-based LIF formulation, and gradually move towards more abstract, purely map-based cases.

2.1. Two-dimensional, fast–slow, spiking–bursting models

Discretizations of one-variable IF models, such as those introduced in Section 1.2, have exerted limited appeal, mainly theoretical [39–42], in recent modeling research. The reason is that IF models are already extremely simple, and discretization does not offer any computational advantage. However, an extension of the IF model to two variables has gained wide acceptance as a versatile and convenient map-based alternative to continuous-time spiking–bursting models.

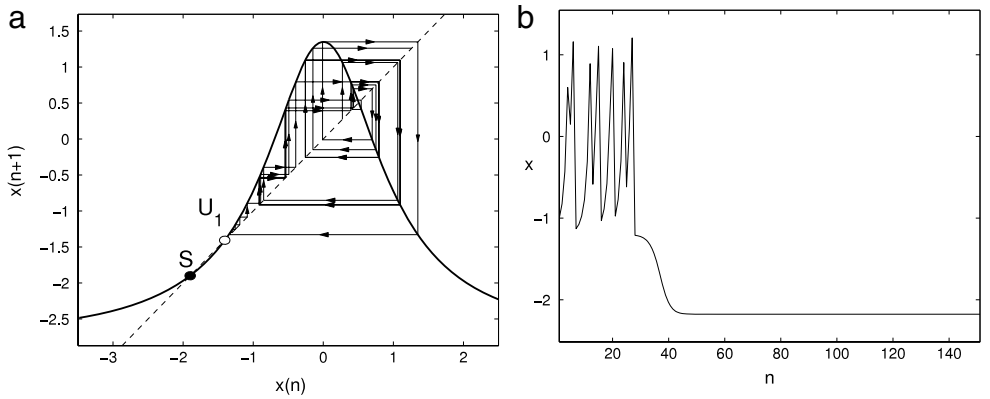

Fig. 8. (a) First return map of the x variable of the chaotic Rulkov map-based model [Eq. (18)], with $\alpha = 4.15$ and $y = -2.8$. S is the stable fixed point, U_1 is an unstable fixed point. A cobweb of the orbit in (b) is superimposed on the diagram. The neuron is in the quiescent or resting regime. (b) x-variable orbit of the system in (a).

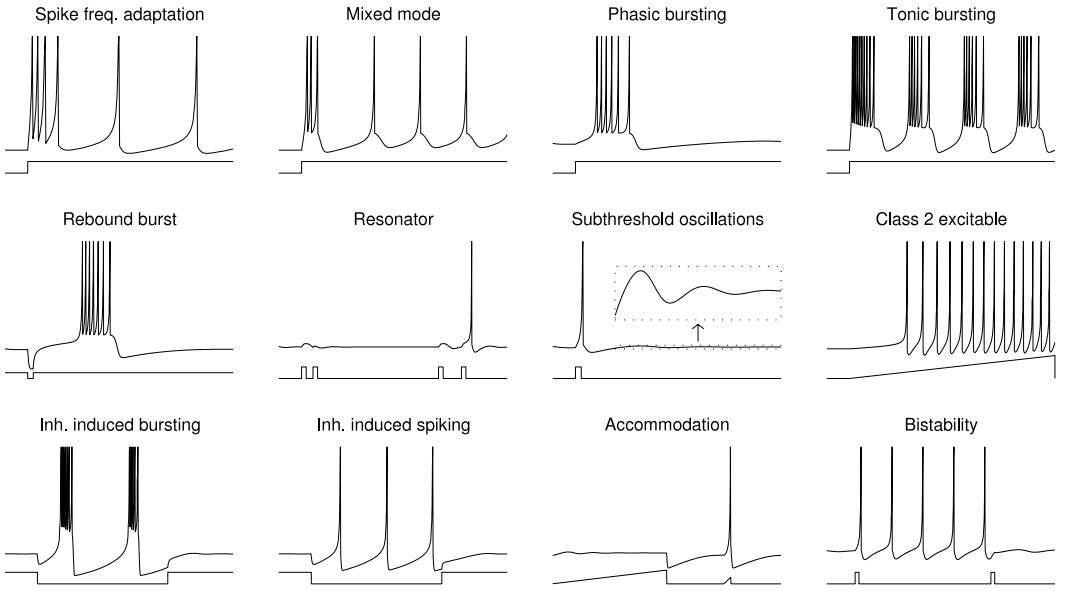

Fig. 9. A set of neuronal behaviors that cannot be reproduced by nonlinear integrate-and-fire models. In each case, the lower trace represents external injected current while the upper trace is the neuron voltage. All these behaviors can be simulated in two-dimensional map-based models. The code generating this figure is from [43]. It is freely available at www.izhikevich.com.

Indeed, the limitations of one-variable IF models become evident when trying to reproduce certain types of dynamics which are intrinsic to neurons and therefore should originate from autonomous properties of the model, without recourse to ad hoc external stimulation. These include such salient neuronal features as spike frequency adaptation (instead of periodic spiking), Type II excitability [as opposed to Type I [22]], bursting, subthreshold oscillations and resonance. In Fig. 9 an array of such behaviors is represented. The key to most of them is the separation of two different time scales corresponding to two different variables. In fact, the addition of a second, slow variable to a map-based IF model transforms it into a highly versatile neuron type that has found widespread acceptance in recent literature. All the examples of Fig. 9 have been generated by the same two-dimensional map-based model [44]. Although bursting, and, more generally, slow and fast time scales, can be achieved in one-dimensional models (Section 2.2), one-dimensional bursting maps do not have parameters that can be easily related to conductance neuron models and have not met widespread acceptance. The two-dimensional models described in this section, on the contrary, are easy to adapt to different applications and to relate to standard continuous-time conductance-based models. An thorough study of this family of models, in its ODE formulation, can be found in [45,31].

Two-dimensional map-based models derived from the IF family conform to the following generic equations:

$$\begin{aligned} v(t+1) &= F[v(t), I \pm u(t)], \\ u(t+1) &= u(t) \mp \epsilon \cdot [v(t) - qu(t) - \sigma], \end{aligned} \tag{7}$$

where $F(v, I \pm u)$, very much as in the nonlinear IF model of Eq. (6), is a function that embodies the subthreshold behavior of the voltage,

$$F(v, I \pm u) = f(v) + I \pm u, \tag{8}$$

and also includes a threshold and reset mechanism to produce spikes. We will specify this mechanism and also the form of the nonlinear function $f(v)$ for particular models of this family. First we shall take a look at the generic properties common to all models under Eqs. (7) and (8). The v variable, as in IF models, stands for transmembrane voltage; the added variable, u, is usually called a *recovery* or *adaptation* variable, due to its role in adaptation and bursting, or simply a *slow variable*, because of the time scale difference. The condition for separation of time scales is that ϵ should be a small parameter. This implies $\epsilon \ll 1$, because $F(v, I \pm u)$ is of the order of unity in most of the phase space. Besides, both ϵ and q must be positive if the orbits are to remain bounded. With positive ϵ, the reciprocal effects of v and u on each other go in opposite directions. For example, if the sign of the u term in $F(v, I \pm u)$ is positive, and hence the sign of the $\mp\epsilon[v(t) - qu(t) - \sigma]$ term in the equation for $u(t+1)$ is negative, an increase in u will entail an increase in v that in turn, with ϵ being positive, will limit the increase in u. As for q, a positive value produces an asymptotically stable behavior of u for constant v.

Therefore, with $0 < \epsilon \ll 1$, variations of the recovery variable u are much slower than those of v. This warrants the separation of the system into two subsystems. The so-called *fast subsystem* consists of the voltage equation alone, with variable u considered as a fixed parameter γ:

$$v(t+1) = F[v(t), I \pm \gamma]. \tag{9}$$

On the other hand, the *slow subsystem*, consisting of the u equation alone, now turned into parameter γ, evolves according to average values of v. If, for example, for each value of u in a certain region v follows a N-periodic orbit $V(u, i)$, $i = 1, \ldots, N$, the evolution of u can be approximated by

$$\gamma(t+1) \approx \gamma(t) \mp \epsilon \left[\frac{1}{N} \sum_{i=1}^{N} V(\gamma, i) - q\gamma(t) - \sigma \right]. \tag{10}$$

This can be seen as a discrete-time counterpart of the perturbation method of averaging [46]. This standard analysis technique has many applications in nonlinear dynamics [47] and has been extensively used for the purposes of theoretical neuroscience [48], because neuronal dynamics often involves slow-changing variables. Besides, since in the family of models under study the slow variable u enters the v equation additively, its variations merely shift upwards or downwards the return map of the fast subsystem (9); this allows an intuitive understanding of bursting and adaptation, as explained in Section 3.1.

Neuron models that fit the generic description of Eq. (7) have been proposed independently by different authors in the past few years. Their differences lie mainly in the choice of the nonlinear function $f(v)$ and the values of parameters ϵ and q. The most relevant are those advanced by Izhikevich [43,44], by Rulkov [49,50], by Courbage et al. [36], and by Chialvo [35].

2.1.1. The Izhikevich model

The Izhikevich model is originally continuous-time [43], but Euler discretization with a time step of 1 ms [44] transforms it into the map

$$\begin{aligned} v(t+1) &= F[v(t), I - u(t)], \\ u(t+1) &= \begin{cases} u(t) + a \cdot [bv(t) - u(t)], & \text{if } v(t) < 30, \\ u(t) + d, & \text{if } v(t) \geq 30, \end{cases} \end{aligned} \tag{11}$$

where

$$F(v, I) = \begin{cases} \min(0.04v^2 + 6v + 140 + I, 30), & \text{if } v < 30, \\ c, & \text{if } v \geq 30. \end{cases} \tag{12}$$

Smaller discretization time steps may be required depending on the application, merely resulting in a scaling down of I, $F(v, I - u)$, u and b.

In Eqs. (11) and (12), v is membrane voltage, in millivolts, and u is the slow recovery (or adaptation) variable. The values of parameters of the generic model (7) that correspond to the Izhikevich model are $\epsilon = ab \ll 1$, $q = 1/b$ and $\sigma = 0$. Therefore, $a > 0$ is the small parameter that separates time scales. Note also that parameter c stands for the reset voltage. The nonlinear subthreshold function of Eq. (8) is obviously $f(v) = 0.04v^2 + 6v + 140$. The slow subsystem includes an interesting addition to the generic model: when a spike is fired, the slow variable undergoes a sudden jump of value equal to parameter d. Effects of spiking upon the slow processes of the neuron can thus be incorporated, providing further modeling flexibility. An excellent reference for the role of this parameter is [31].

Notice that the return map of the fast subsystem is precisely that of the QIF model. It is displayed for convenience, for a particular value of the slow variable u, in Fig. 10(b); compare it to Fig. 7(a). However, since the full model is two-dimensional, it cannot be captured in this return map. A phase plane representation of nullclines, as in Fig. 10(c), is more appropriate. The phase plane [21] is the plane where all possible values of the two variables of the system are represented; in the Izhikevich system it is the u–v plane. Nullclines are the lines in the phase plane where each variable is left unchanged by one iteration

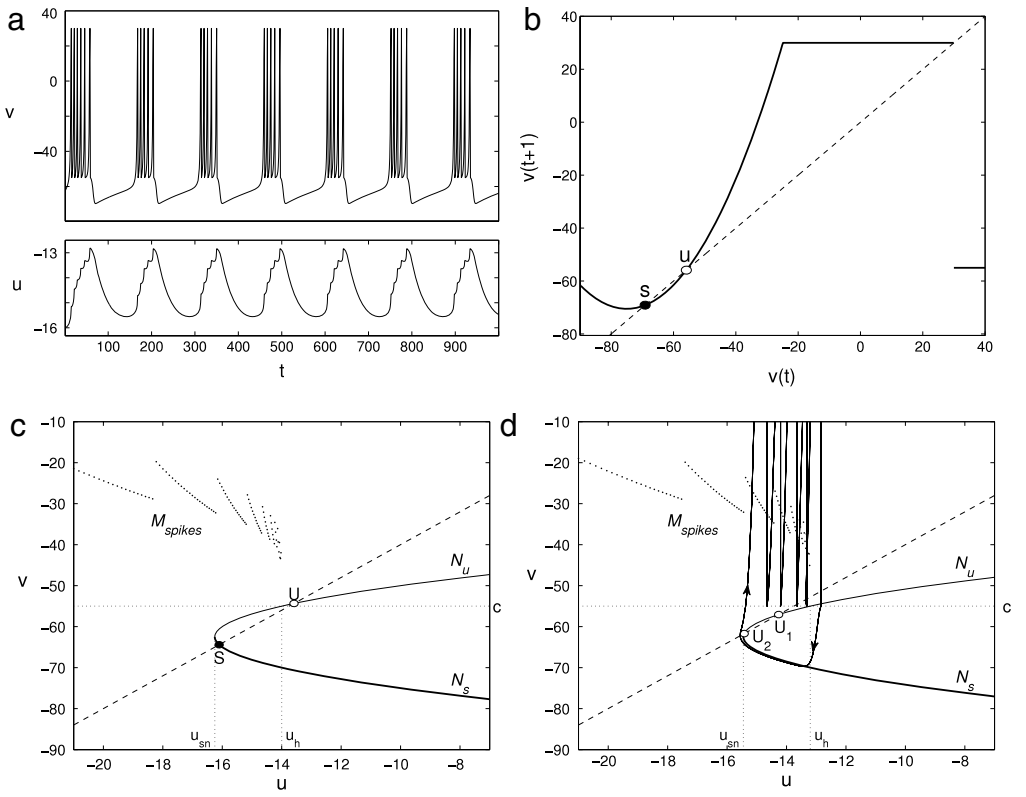

Fig. 10. (a) Time evolution of the Izhikevich model variables in a bursting orbit. Parameter values are $a = 0.02$, $b = 0.25$, $c = -55$, $d = 0$. $I = 0.8$. (b) First return map of the fast subsystem, when $u - I = -14.5$. s and u refer to stable and unstable fixed points of the subsystem. (c) and (d) Nullcline diagrams for two different values of input excitation I. The parabolic fast nullcline is divided into its two branches, N_s and N_u, according to the stability of the corresponding fixed points of the fast subsystem; they meet at the saddle–node vertex, at $u = u_{sn}$. The dashed straight line is the slow nullcline, and the dotted horizontal line represents the reset voltage level $v = c$. M_{spikes} stands for the manifold of average values of spiking cycles of the fast subsystem at each fixed value of u; u_h stands for the value of u for the homoclinic spiking orbit. In (c), $I = 0$, the fixed point of the full system S is stable; in (d), $I = 0.8$, the fixed point U is unstable, the orbit in (a) is superimposed on the diagram.

of the map; they are the curves of fixed points of each subsystem, considering the other variable as a fixed parameter. In the Izhikevich model, the nullcline corresponding to the fast subsystem is readily obtained by equating $v(t+1)$ to $v(t)$ in Eq. (11). This yields the following curve in the phase plane:

$$u = 0.04v^2 + 5v + 140 + I \quad \text{if } v < 30.$$

Thus the fast subsystem nullcline is a parabola that shifts leftwards or rightwards in the phase plane if I decreases or increases [compare Fig. 10(c) and (d)]. The two-branched nullcline implies that, for each value of u to the right of the vertex, the fast subsystem has two fixed points, as in Fig. 10(b), one stable, the other unstable. Correspondingly, the branches of the parabolic nullcline can be classified as stable (N_s) and unstable (N_u). The vertex of the parabola is at the saddle–node bifurcation of the fast subsystem. Values of u to the right of the vertex correspond to the situation depicted in Fig. 7(c), where the fixed points have vanished.

On the other hand, the slow subsystem nullcline is a slanted straight line. When the state is above this line, u increases; when below, u decreases. Parameter b sets the slope of this nullcline; its role will be discussed in Section 3.2. The points where the fast and slow subsystem nullclines intersect are the fixed points of the full, two-dimensional system.

The dotted, piecewise continuous manifold labeled M_{spikes} in Figs. 10(c) and (d) represents average values of the spike cycles of the fast subsystem. Its discontinuities correspond to changes in the period of the cycles. This manifold is useful to intuitively predict the orbits of the full system. When, as in the figure, M_{spikes} lies completely above the slow nullcline, u will steadily increase along any spiking orbit up to $u = u_h$, where the reset voltage level $v = c$ intersects N_u, forming a homoclinic orbit of the fast subsystem. If instead M_{spikes} intersects the slow nullcline, as in Fig. 26(c), the full system may end up in a spiking orbit around the value of u of the intersection.

The Izhikevich map can have up to two fixed points. The character of these points changes with the external input current I, as shown in Figs. 10(c) and (d). The difference between the two figures is a horizontal shift of the manifolds associated to the fast subsystem (N_s, N_u and M_{spikes}). When I is low, as in Fig. 10(c), where $I = 0$, one fixed point is stable, while the other is a saddle. The stable fixed point, in this case, is globally attracting, since even orbits that begin spiking will, due to

the position of the slow nullcline below M_{spikes}, end up falling on N_s and following an orbit a-close to it up to S. The neuron is then quiescent, and excitable: a perturbation that kicks v above the unstable branch of the fast nullcline will elicit a spike.

If I increases, the manifolds shift rightwards and S loses stability through a Neimark–Sacker bifurcation when

$$I_{NS,\text{Izh}} = 16.25 - 62.5b + 6.25\left(b^2 - \frac{(b-a)^2}{(1-a)^2}\right).$$

This is a-close to the value where the slow nullcline intersects the N_s–N_u vertex. A diagram of this bifurcation can be seen in Fig. 32(a). It is worth pointing out that S ceases to be globally attracting at a slightly lower value of I because the Neimark–Sacker bifurcation is subcritical (unless $b > 1 + a$ [51]). After the bifurcation, S turns into an unstable focus U_2. Thus the two fixed points continue to exist, but now they are both unstable [Fig. 10(d), $I = 0.8$]. The system is forced into a spiking or bursting orbit. Such orbits will be discussed in Section 3.1. Fig. 28(a) shows how the transition depends on the value of the reset voltage c.

2.1.2. The Rulkov model

There are at least three variants of this model, first proposed by N.F. Rulkov. For purposes of clarity, we will refer to the first one as the *non-chaotic Rulkov model* [50], the second one as the *supercritical Rulkov model* [52] (which is also non-chaotic), and the third one as the *chaotic Rulkov model* [49].

The non-chaotic Rulkov model This model [50] is defined by the equations

$$\begin{aligned} x(n+1) &= F[x(n), y(n) + I], \\ y(n+1) &= y(n) - \mu[x(n) - \sigma], \end{aligned} \tag{13}$$

where

$$F(x,y) = \begin{cases} \alpha(1-x)^{-1} + y, & \text{if } x \le 0, \\ \alpha + y, & \text{if } 0 < x < \alpha + y, \\ -1, & \text{if } x \ge \alpha + y. \end{cases} \tag{14}$$

We see that this is the model of Eqs. (7) and (8) with $\epsilon = \mu \ll 1$, $q = 0$ and $f(x) = \alpha(1-x)^{-1}$. Parameter σ can be identified in both models (although in its original formulation [50], the Rulkov model uses $\sigma' = \sigma + 1$). The reset level is fixed at $x_{\text{reset}} = -1$. The role of the parameter α will be explained later. As an aside, let us point out that the fact that the variables of the Rulkov model are called x and y instead of v and u, and that time is designated by n and not t, and is due to the purely phenomenological approach that Rulkov suggests in his publications. While in the Izhikevich model, described in Section 2.1.1, each time step is meant to represent 1 ms of real time, and variable v stands for membrane voltage in millivolts, in the Rulkov model no claim is made about its relation to physical quantities, other than x being directly related to membrane voltage and time steps being uniform. The precise conversion is left unspecified. In some works [53,54] the author suggests, from comparisons with Hodgkin–Huxley models, an equivalence of $\Delta t = 0.5$ ms per time step, and scaling

$$v(n)\ [\text{mV}] = \frac{-50}{1-\sqrt{\alpha}}x(n),$$

so that the spiking threshold, which lies at $x = 1 - \sqrt{\alpha}$, corresponds to -50 mV, and the peak of spikes is $+50$ mV for $\alpha = 4$. A similar correspondence can be found in [55], which we comment on in Section 5.2.

Fig. 11 represents a typical bursting orbit, the return map of the fast subsystem, and the nullcline diagram for two different values of the excitation parameter σ. The return map is again nonlinear integrate-and-fire. As for the full system, a comparison of Figs. 10(c) and (d) with Figs. 11(c) and (d) reveals many common features, but also some interesting differences. The rightward orientation of the vertex of the fast nullcline is due to the choice of the plus sign in the alternative of the fast subsystem (9). This means that variable y has an excitatory character, while u in the Izhikevich model is inhibitory. Since these variables are purely phenomenological, the distinction is immaterial. More importantly, we see that the slow nullcline, $x = \sigma$, is horizontal, and not slanted as in the Izhikevich model. This is due to the lack of a y-dependent term in the equation for the increments of variable y: the slow variable has no tendency of its own, neither to stabilize nor to explode. It is *neutrally stable*. Besides, the Rulkov model has only one fixed point, at the intersection of the slow and fast nullclines. In the singular $\mu \to 0$ limit, this point is stable if it lies on N_s, and unstable otherwise. More precisely, the change in stability takes place due to a Neimark–Sacker bifurcation whose condition is

$$\sigma_{N-S} = x_{N-S} = 1 - \sqrt{\frac{\alpha}{1-\mu}}, \tag{15}$$

which, as anticipated, is μ-close to the vertex of the fast nullcline,

$$x_{sn} = 1 - \sqrt{\alpha}. \tag{16}$$

This helps us understand the role of σ as a modulating external excitation. It can be assimilated to slow changes in the conductance of ionic channels. This parameter is absent from the Izhikevich model (where $\sigma = 0$, as we know) for the

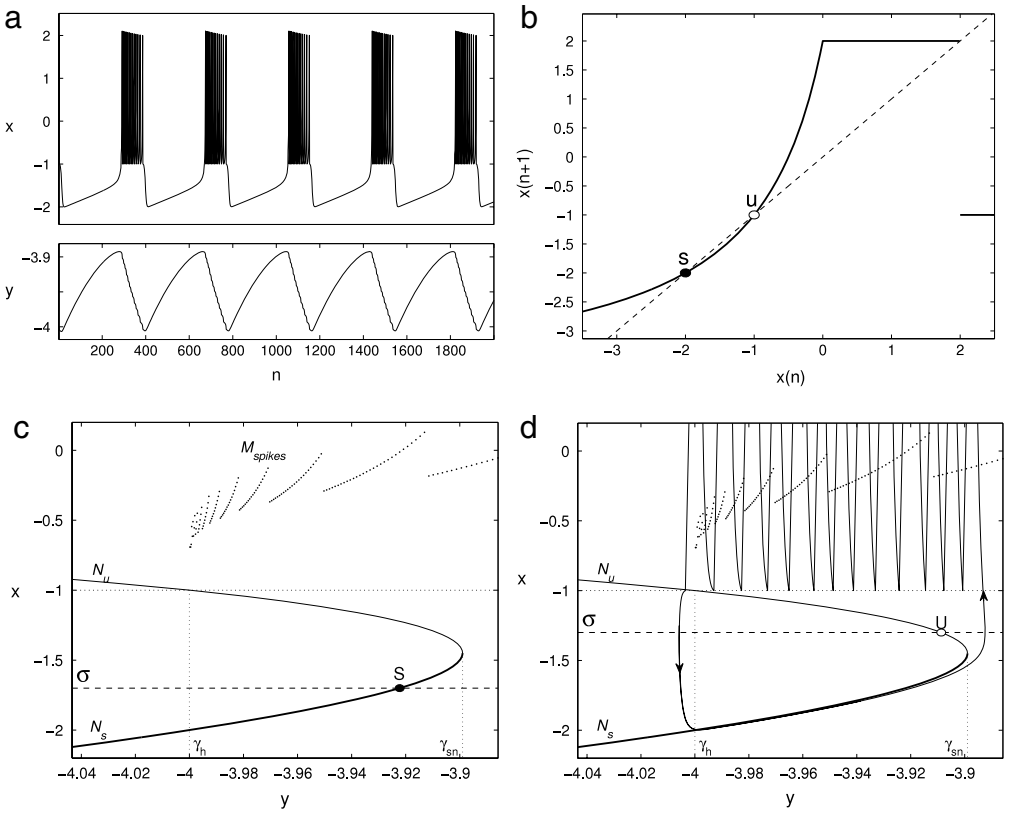

Fig. 11. (a) Time evolution of the Rulkov model of Eqs. (13) along a burtsting orbit. Parameter values are $\alpha = 6$, $\sigma = -1.3$ and $I = 0$. (b) First return map of the fast subsystem, when $y = -4$. s and u refer to stable and unstable fixed points of the subsystem. (c) and (d) Nullcline diagrams for two different values of input excitation σ. The parabolic fast nullcline is divided into its two branches, N_s and N_u, according to the stability of the corresponding fixed points of the fast subsystem; they meet at the saddle–node vertex, at $y = \gamma_{sn}$. The dashed horizontal line is the slow nullcline, and the dotted horizontal line represents the reset voltage level $x = -1$. M_{spikes} stands for the manifold of average values of spiking cycles of the fast subsystem at each fixed value of y; γ_h stands for the value of y for the homoclinic spiking orbit. In (c), $\sigma = -1.7$, and the fixed point of the system is stable (S); in (d), $\sigma = -1.3$, and it is unstable (U); the orbit from (a) is superimposed on the diagram.

following reason: in all models that follow Eqs. (7), changes in σ shift the slow nullcline vertically in the v–u plane, while changes in I shift the fast nullcline horizontally. In the Izhikevich model, due to the slope of the slow nullcline, both kinds of changes are interchangeable: a change in σ of value $\Delta\sigma$ is equivalent to a change in I of value $\Delta I = b\Delta\sigma$, and a change of variable $u' = u - b\Delta\sigma$. Since the numeric value of u has no physical meaning, using I as the unique external input has no consequences for the validity and flexibility of the model. In the Rulkov model, with its horizontal slow nullcline, there exists no such equivalence between horizontal and vertical shifts, and I and σ have different effects.

The role of α is analogous to that of c in the Izhikevich model, in the sense that it determines the position of the reset voltage relative to the stable and unstable branches of the fast nullcline. In the Izhikevich model, the nullcline is fixed in the v axis and the reset level is determined by parameter c; in the Rulkov model, the reset level is fixed at $x = -1$ while the fast subsystem nullcline shifts with α. This is important for dynamics: bursting can only happen, in the $\mu \to 0$ limit, if the reset level intersects the branch N_u of the fast nullcline. We discuss this issue in Section 3.1. Fig. 28(b) shows the steady-state regimes of the model as a function of α and σ; comparison with Fig. 28(a) underscores the analogy between c and α, and between I and σ, in the Izhikevich and Rulkov models.

The supercritical Rulkov model The supercritical Rulkov model [52] also obeys Eqs. (13), but has a different form for $F(x, y)$, namely

$$F(x,y) = \begin{cases} \dfrac{-\alpha^2}{4} - \alpha + y, & \text{if } x < -1 - \dfrac{\alpha}{2}, \\ \alpha x + (x+1)^2 + y, & \text{if } -1 - \dfrac{\alpha}{2} \le x \le 0, \\ 1 + y, & \text{if } 0 < x < 1 + y, \\ -1, & \text{if } x \ge 1 + y. \end{cases} \tag{17}$$

The return map, which we show in Fig. 12(a), is apparently indistinguishable from that of Fig. 11(b), and neither would the nullcline diagram give any hint of a difference with Figs. 11(c) or (d). As in the non-chaotic Rulkov model, the parameter

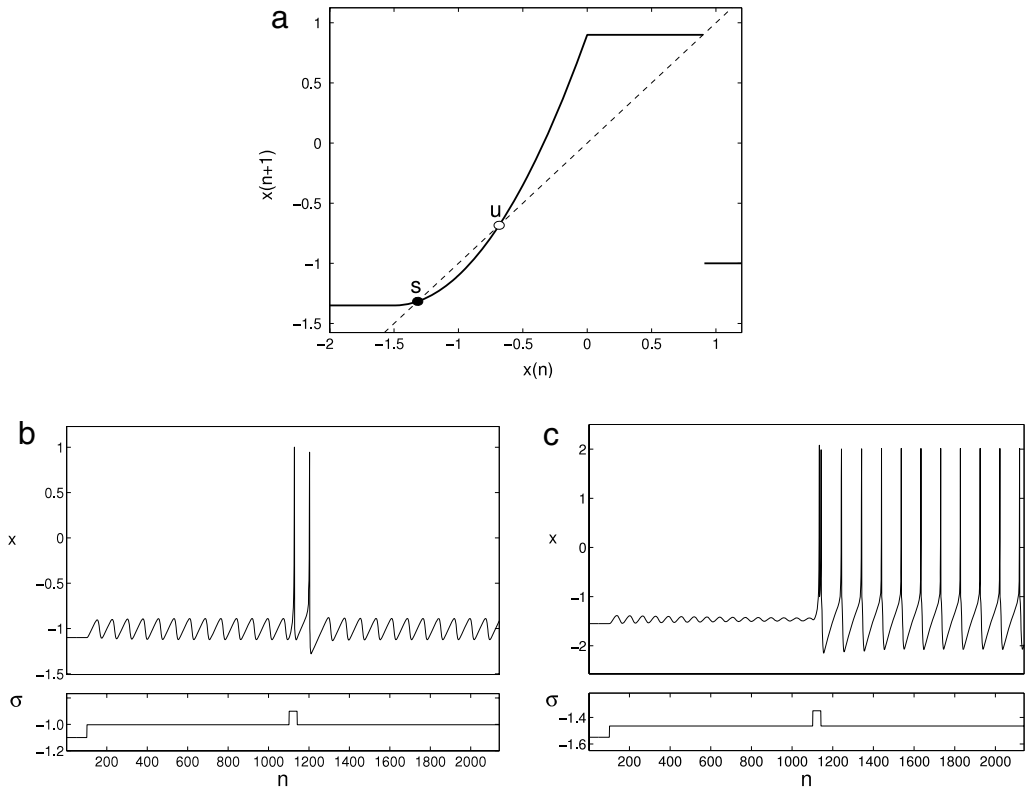

Fig. 12. (a) Return map of the fast subsystem of the supercritical Rulkov model [Eq. (17)], with $\alpha = 1$ and $y = -0.1$. (b) Illustration of subthreshold oscillations and lack of bistability in the supercritical model, with $\mu = 0.01$. (c) Same case as in (b) in the non-chaotic Rulkov model, with $\alpha = 6$ and $\mu = 0.01$, illustrating decaying subthreshold oscillations and bistability.

α decides whether the model is or not a burster (in this case, $\alpha > 1$ is necessary for bursting). But this form of the map produces a very interesting effect: self-sustained subthreshold oscillations [52]. We will have more to say about this in Section 3.2; here we point out that the difference stems from the change in character of the Neimark–Sacker bifurcation of the fixed point, from subcritical to supercritical, and hence the name we have chosen for the model. This further entails that the supercritical map is not bistable, while the non-chaotic model is. In Fig. 12(b), a supercritical Rulkov neuron receives an initial input step and initiates small, sustained oscillations. A short additional pulse gives rise to spiking, but this only lasts for the duration of the pulse: there is no bistability. On the other hand, when a non-chaotic model goes through the same procedure, as in Fig. 12(c), the spiking continues even after the short pulse is over, showing that the system is bistable at the excitation level of the initial step. Besides, the subthreshold oscillations slowly die out. Incidentally, the bistability *of the full system*, which, as we have just demonstrated, is lacking in the supercritical model, and is not to be confused with the bistability *of the fast subsystem*, present in all bursting models.

The chaotic Rulkov model Finally, the chaotic Rulkov model [49] also obeys Eq. (13), but has a peculiar form of $F(x, y)$:

$$F(x, y) = \frac{\alpha}{1 + x^2} + y. \tag{18}$$

Notice that the familiar threshold-and-reset, piecewise construction of $F(x, y)$ is absent. It has been replaced by a unimodal map, depicted in Fig. 13(a). There is still a stable-unstable fixed point pair, labeled s and u_1, that disappears through a saddle–node bifurcation when $y + I$ increases. Spiking orbits are no longer periodic, but chaotic. One such orbit has been superimposed over the return map of Fig. 13(a). The chaotic nature of bursts is evident in the phase plane diagram of Fig. 13(b), where a classic bifurcation diagram of the chaotic map has been superimposed. A saddle–node bifurcation at $y = \gamma_{sn}$ determines the beginning of bursts as in previous models, while the ending takes place through an *external crisis* at $y = \gamma_{cr}$, where the second iterate of the critical point of the fast map, $x = 0$, touches the middle unstable branch N_u of the fast nullcline. Therefore, instead of a horizontal line of reset voltages, we have a curve of second iterates of $x = 0$, which in Fig. 13(b) is labeled $\Xi_{\min}$. Notice that the period-doubling cascade leading to chaos is born at values of y well below the region of bistability; chaos is therefore fully developed in the bursting region.

Fig. 14 compares a bursting orbit of the chaotic Rulkov map with a bursting orbit of the non-chaotic Rulkov map. The non-chaotic map produces a periodic bursting trajectory that ends μ-close to the homoclinic point γ_h, while the bursts of the chaotic map are irregular and may end well past the external crisis value γ_{cr}. The irregularity of the chaotic bursts is similar

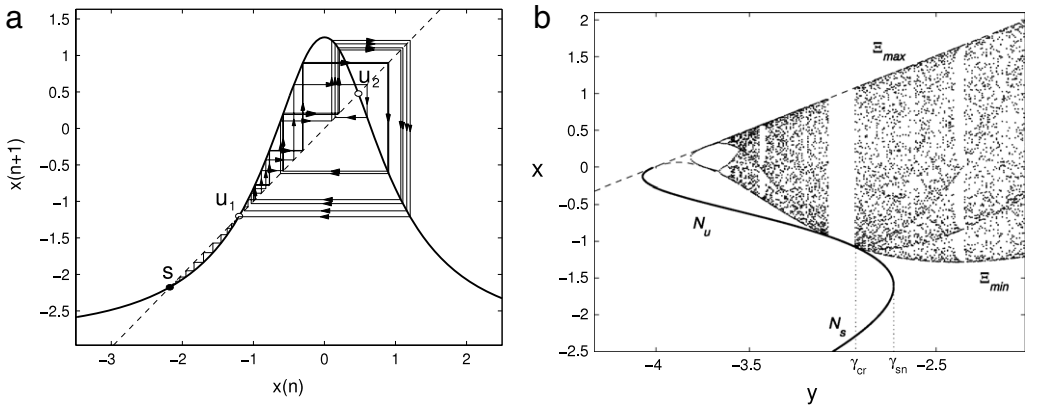

Fig. 13. (a) Return map of the fast subsystem of the chaotic Rulkov model of Eq. (18), with $\alpha = 4.15$ $y = -2.9$. An orbit has been superimposed over the return map. s marks the stable fixed point, u_1 and u_2 unstable fixed points. (b) A bifurcation diagram of the model. N_s and N_u are stable and unstable branches of the fast nullcline; a third branch has not been labeled. $\Xi_{\max}$ and $\Xi_{\min}$ are the curves of the first and second iterate of the critical point $x = 0$. γ_{sn} and γ_{cr} are the values of y that correspond to the saddle–node and external crisis bifurcation of the fast map.

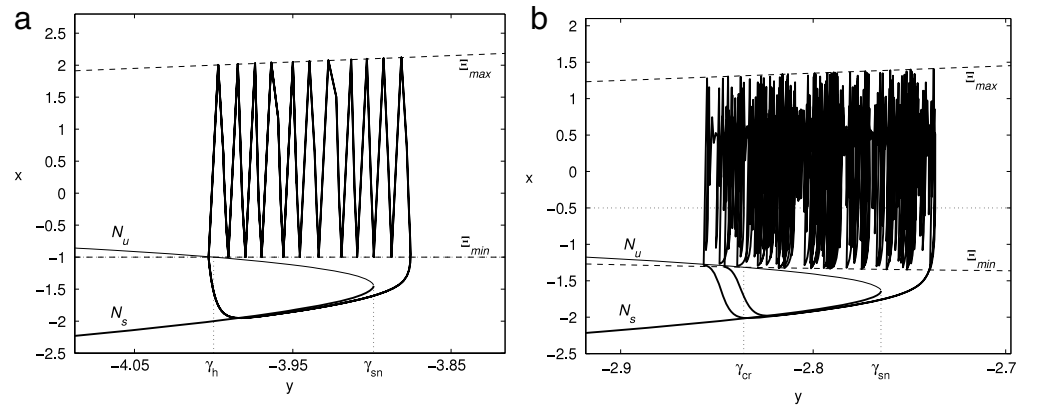

Fig. 14. (a) An orbit of the non-chaotic Rulkov map superimposed over its nullcline diagram. $\alpha = 6$, $\mu = 0.002$ and $\sigma = -1$. Labels have the same meaning as in Fig. 13. (b) Same as in (a) for the chaotic Rulkov map. $\alpha = 4.15$, $\mu = 0.001$ and $\sigma = -0.5$.

to that of more realistic bursters with stochastic channel dynamics, such as the Sherman model for pancreatic β-cells [56]. Bursting orbits are described in more detail in Section 3.1.

2.1.3. The Courbage–Nekorkin–Vdovin (CNV) model

A model recently proposed by Nekorkin and Vdovin [57], and slightly modified in [36], has important similarities to the chaotic Rulkov model. The dynamics of the slow variable are the same in both maps; the difference lies in the fast variable, which follows, instead of a unimodal map, a Lorenz-type map [58].

The equations of the CNV model are

$$\begin{aligned} x(n+1) &= x(n) + F[x(n)] - y(n) - \beta H[x(n) - d], \\ y(n+1) &= y(n) + \epsilon \cdot [x(n) - J], \end{aligned} \tag{19}$$

where $H(x)$ is the Heaviside step function and

$$F(x) = \begin{cases} -m_0 x, & \text{if } x \le J_{\min}, \\ m_1(x - a), & \text{if } J_{\min} < x < J_{\max}, \\ -m_0(x - 1), & \text{if } x \ge J_{\max}. \end{cases} \tag{20}$$

The equivalence in terms of the generic model of Eqs. (7) and (8) is $q = 0$, $\sigma = J$ and $f(x) = F(x) - \beta H(x - d)$, while ϵ can be identified in both models. The fast subsystem, depicted in Fig. 15(b), is a piecewise linear map; m_0 and m_1 are positive constants, while $J_{\min}$ and $J_{\max}$, the values of x where the fast subsystem first return map changes its slope, are given by

$$J_{\min} = \frac{a m_1}{m_0 + m_1}, \qquad J_{\max} = \frac{m_0 + a m_1}{m_0 + m_1}.$$

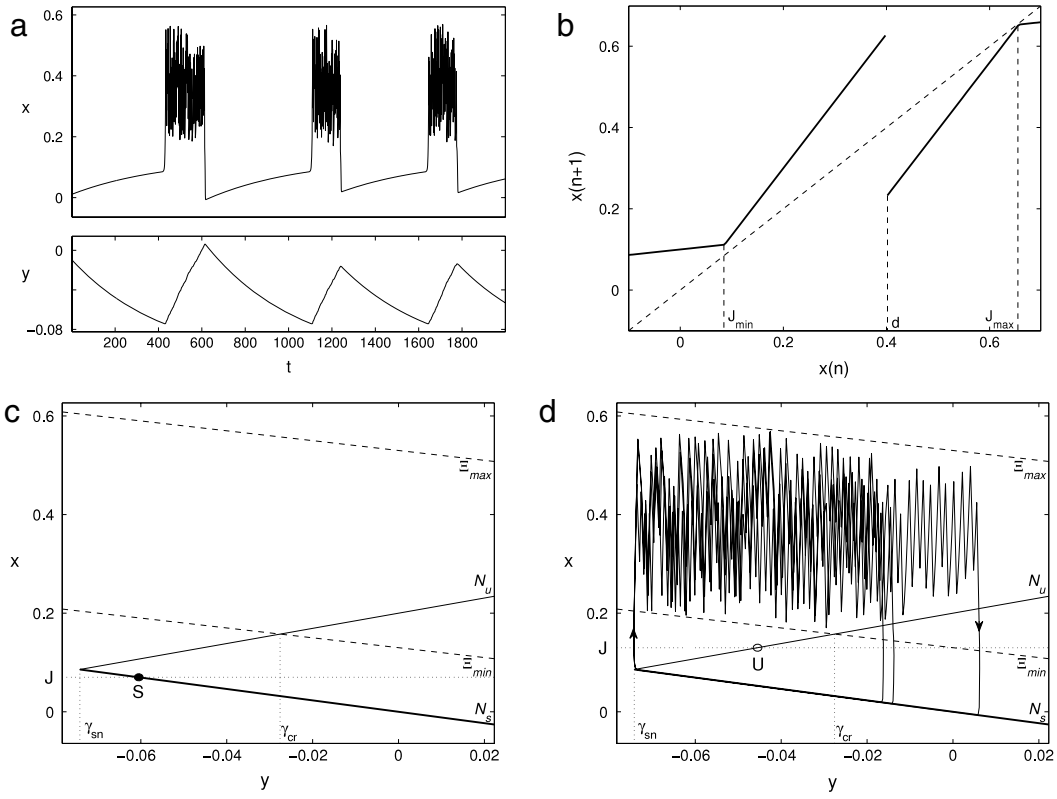

Fig. 15. (a) Time evolution of the Courbage–Nekorkin–Vdovin (CNV) model along a bursting orbit. Parameter values are $m_0 = 0.864$, $m_1 = 0.65$, $a = 0.2$, $d = 0.4$, $\beta = 0.4$, $\epsilon = 0.002$ and $J = 0.13$. (b) First return map of the fast subsystem, when $y = 0$. s and u refer to stable and unstable fixed points of the subsystem. (c) and (d) Nullcline diagrams. N_s and N_u are stable and unstable branches of the fast nullcline. $\Xi_{\max}$ and $\Xi_{\min}$ are the curves of first iterates of $x = d^-$ and $x = d^+$, respectively. γ_{sn} and γ_{cr} are the values of y of the saddle–node and external crisis bifurcation of the fast map. In (d), all parameters are the same as in (a), and the orbit is superimposed on the diagram; U marks the unstable fixed point of the full system. In (c), $J = 0.07$, S marks the stable fixed point, and no orbit is represented; the steady state of the system is quiescent.

Parameter d is chosen to lie between $J_{\min}$ and $J_{\max}$. All this ensures that the fast subsystem is everywhere hyperbolic, chaotic, Lorenz-type, with a step discontinuity at $x = d$ of size β. To help understand its dynamics, it has been depicted in Fig. 16 for different values of the slow variable y. Just as in the Izhikevich and Rulkov fast return maps, a saddle–node bifurcation takes place for a certain value of the slow variable [namely, $y = F(J_{\min})$]. For y above this value, there exists a stable fixed point in the fast subsystem that is globally attracting whenever the lowest point of the rightmost piece of the return map lies below the unstable fixed point. This is what happens in Figs. 16(a) and (b), and is equivalent to the situation in the chaotic Rulkov model when y is below the external crisis bifurcation [γ_{cr} in Fig. 13(b)].

Thus the CNV model is the Lorenz-type counterpart of the chaotic Rulkov model. The similarity between the two maps is apparent in the comparison of Fig. 15(d) with Fig. 14(b). The phase planes of both models are equivalent. The differences in their fast subsystems affect the distribution of the amplitudes of the spikes inside each burst, but not the burst mechanism: the system follows an invariant curve ϵ-close to the stable branch of the fast subsystem nullcline, N_s, and the saddle–node bifurcation, at $(x, y) = [J_{\min}, F(J_{\min})]$, is close to the initiation of the active phase of the burst. At the point where the line of minimum iterates $\Xi_{\min}$ intersects the unstable branch N_u, an external crisis bifurcation takes place, signaling the possibility of burst ending. However, the dynamics of the CNV Lorenz-type map are not the same as those of the Rulkov unimodal map, and burst length and spike distributions differ. This may be further developed by studying the invariant measure of each map [59].

Therefore, both the Rulkov and CNV models are of the fold/homoclinic kind [60], with different spike dynamics. Interestingly, the Neimark–Sacker bifurcation that takes place in the CNV model when J changes and the slow nullcline traverses ϵ-close to the saddle–node bifurcation of the fast subsystem is supercritical, and thus the CNV model can exhibit sustained subthreshold oscillations, just as the supercritical Rulkov model. Additionally, when parameters are chosen so that the piece of the fast return map at $x > J_{\max}$ comes into play, a peculiar bimodal regime sets in where bursts alternate chaotically with large spikes. Finally, if the size β of the discontinuity is small enough, the system will behave as a discrete relaxation oscillator in the vein of the FitzHugh–Nagumo model [61]. These three other regimes are depicted in Fig. 17.

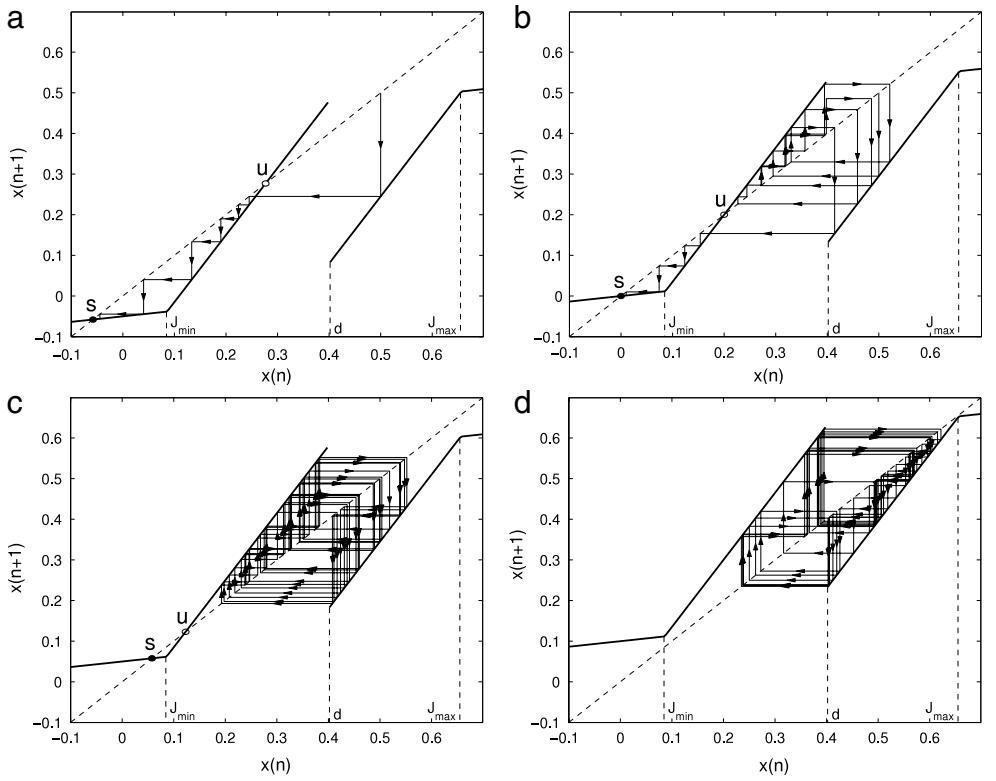

Fig. 16. First return maps of the fast subsystem of the Courbage–Nekorkin–Vdovin (CNV) neuron model given by Eqs. (19), with $m_0 = 0.864$, $m_1 = 0.65$, $a = 0.2$, $d = 0.4$, and $\beta = 0.4$. The values of the recovery variable are in each case: (a) $y = 0.05$, (b) $y = 0.0$, (c) $y = -0.05$, and (d) $y = -0.1$.

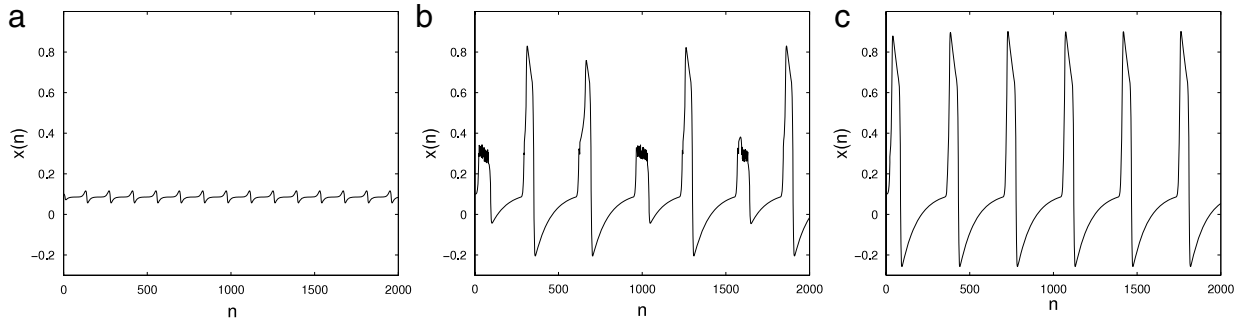

Fig. 17. Three different regimes of the Courbage–Nekorkin–Vdovin (CNV) neuron model. In all three cases, $m_0 = 0.4$, $m_1 = 0.3$, $a = 0.2$ and $d = 0.3$. (a) Subthreshold oscillations: $J = 0.08573$, $\epsilon = 0.025$ and $\beta = 0.3$. (b) Burst-spike alternation: $J = 0.1123$, $\epsilon = 0.004$, $\beta = 0.072$. (c) Relaxation oscillations, $J = 0.1123$, $\epsilon = 0.004$, $\beta = 0.05$. According to Courbage et al. [36].

2.1.4. The Chialvo model

A map introduced by [35] closely resembles the chaotic Rulkov map; it may be considered its predecessor, although there has been apparently no connection between them. The equations of the map are

$$\begin{aligned} x(n+1) &= x(n)^2 e^{y(n)-x(n)} + I, \\ y(n+1) &= ay(n) - bx(n) + c. \end{aligned} \tag{21}$$

The similarity with the generic model of Eq. (7) is evident. Fig. 18(c) and (d) show the nullcline diagram in the quiescent (excitable) and spiking regimes; again we find the stable and unstable branches of the fast nullcline, intersected by a slanted slow nullcline. In this case, changes in external input do not merely shift the fast nullcline, but alter its shape in a nonlinear way. In fact, the model does not exactly fit into the generic equations because the variable y does not enter additively, but multiplicatively, in the x equation. This, however, has weighty consequences on the dynamics of the system. As y grows the return map of x does not simply shift upwards, but rather explodes exponentially, as shown in Fig. 18(b); this discourages using y as a slow variable to produce bursting orbits, because the return map of x varies wildly with the different values

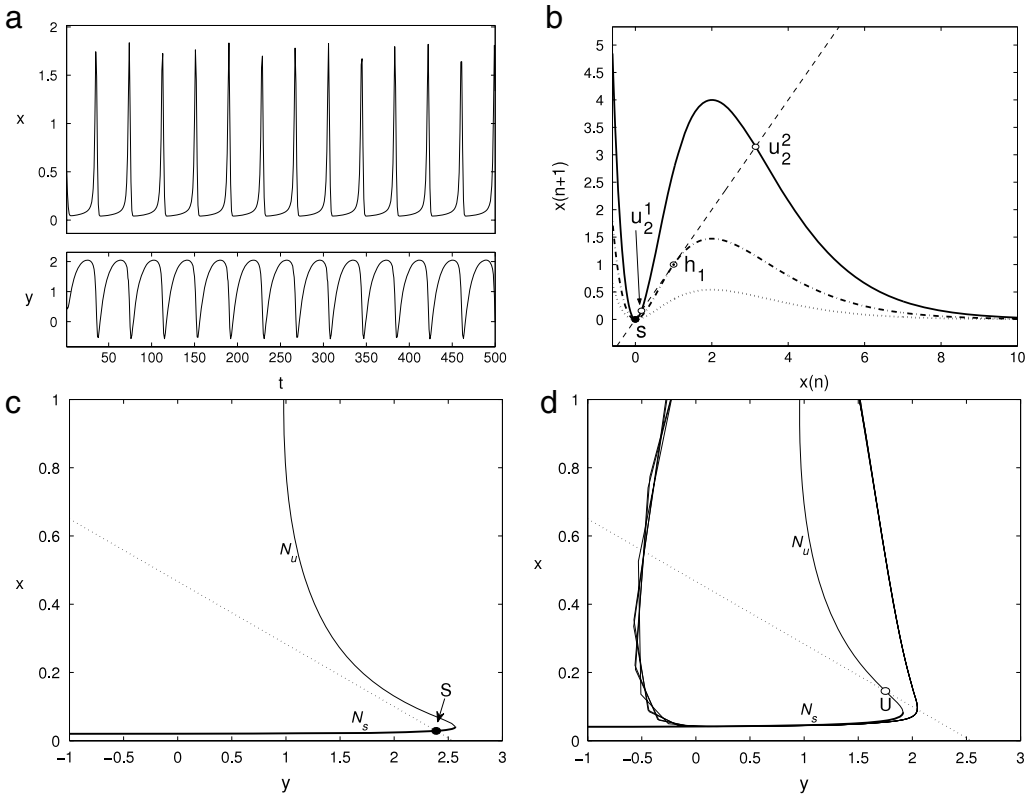

Fig. 18. (a) Time evolution of the Chialvo model along a spiking orbit. Parameter values are $a = 0.89$, $b = 0.6$, $c = 0.28$ and $I = 0.04$. (b) First return map of the fast subsystem, for $I = 0$, when $y = 0$ (dotted), $y = 1$ (dash-dotted) and $y = 2$ (solid line). s marks the stable fixed point. h_1 is a half-stable fixed point for $y = 1$ (precisely at a saddle–node bifurcation). u_2^1 and u_2^2 are unstable fixed points for $y = 2$. (c) and (d) Nullcline diagrams. N_s and N_u are stable and unstable branches of the fast nullcline. In (d) all parameters are the same as in (a), and the orbit is superimposed on the diagram; U marks the unstable fixed point of the full system. In (c), $I = 0.02$, S marks the stable fixed point, and no orbit is represented; the steady state of the system is quiescent.

of y and makes it hard to control burst parameters. The Chialvo neuron is intended as a model of excitable dynamics, with y representing fast, rather than slow, recovery mechanisms. Without the restriction of y being slow, the model displays a wide array of dynamical features, including subthreshold oscillations, bistability and chaotic orbits. Chialvo [35] provides a very clear phase plane description of these features.

2.2. One-dimensional bursters

As mentioned in Section 2.1, it is possible to design one-dimensional map-based models where the only variable represents membrane voltage and which are capable of bursting. The necessary separation of time scales must in that case be embedded in passages through regions where the return map is close to the diagonal, be it near a saddle–node, homoclinic, or flip bifurcation [44]. For example, the parameters of the chaotic Rulkov model and the value of its slow variable can be adjusted so that its fast subsystem is barely past the saddle–node bifurcation and the critical point falls near the bottleneck. One such configuration is shown in Fig. 19(a) and (b). Bursts are chaotic and spikes within them not well defined, as in the original two-dimensional system.

Another one-dimensional bursting map was proposed by [37]. It is depicted in Fig. 19(c). It consists of four linear pieces; the first piece runs close to the diagonal and provides the slow build-up towards spiking. The second and fourth pieces are designed so that the orbit jumps from one to the other, slowly closing upon the intermediate third piece, where the orbit is sent back to silence and build-up. Thus, spikes are always made up of two samples, spike frequency along the burst is invariant, and spike amplitude decreases along the burst. Burst length is chaotic.

A third example, also piecewise linear, is provided by Aguirre et al. [38,62]. In this case the model is not properly one-dimensional, since an additional binary variable s is used to switch between two map branches: one ascending, ($s = 1$), above the diagonal, and one descending ($s = 0$), below the diagonal, as depicted in Fig. 19(e). When the orbit grows above the upper spiking limit (marked D in the figure), the map switches to the descending branch; the opposite takes place when it falls below a lower limit (marked L). This ensures repetitive spiking. To obtain bursting, the map adds a threshold (marked C) around which switching also takes place: when the orbit, ascending from below L, falls in a small region below C, it switches to the descending branch, producing a subthreshold oscillation; similarly, when the orbit, descending from above

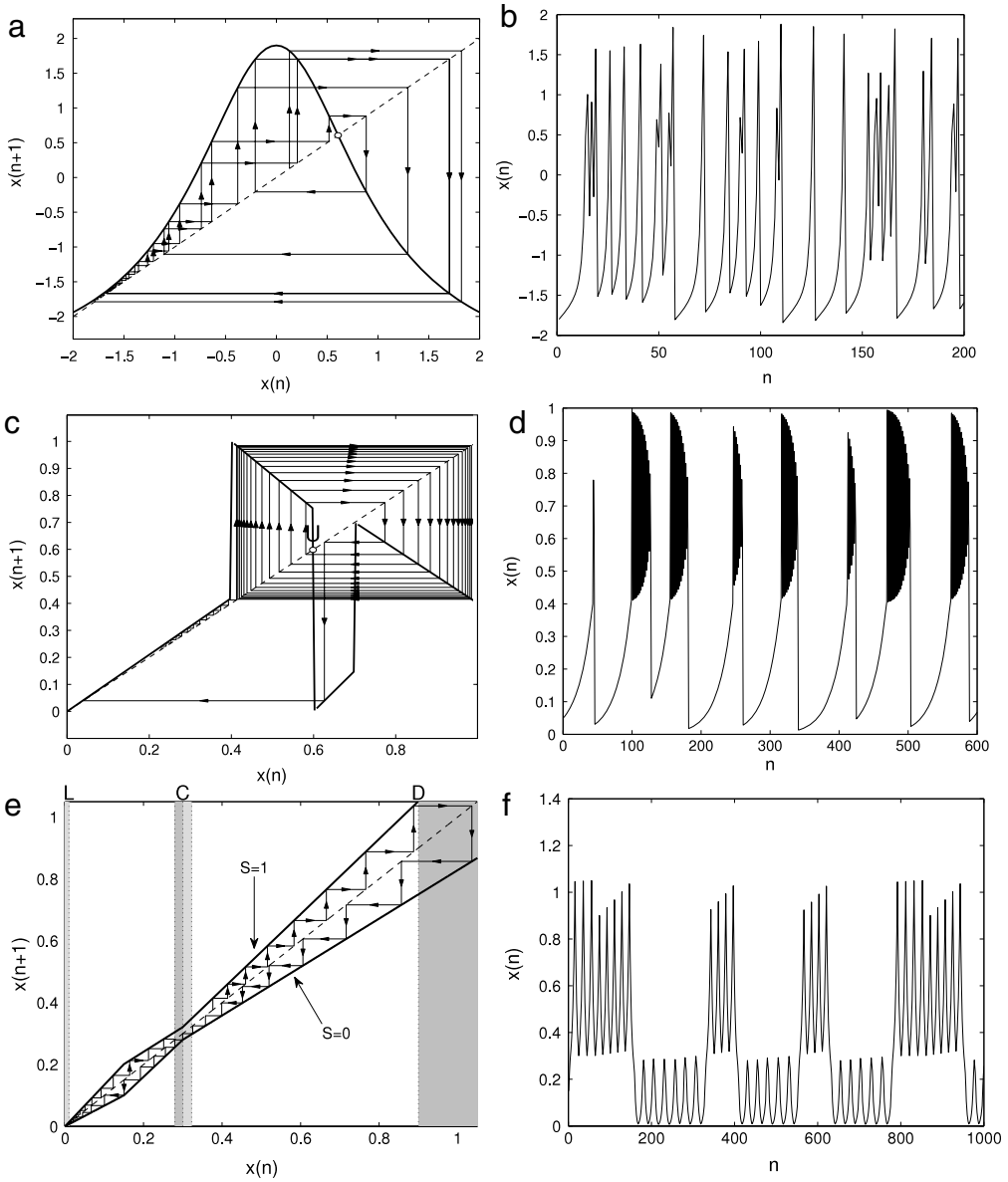

Fig. 19. (a) First return map of the fast subsystem of the chaotic Rulkov model, with $\alpha = 4.8$ and $y = -2.9$. The map is a one-dimensional chaotic burster in itself, with the slow time scale set by the passage through the phantom of a saddle–node bifurcation. (b) Example orbit of the map in (a). (c) First return map of the one-dimensional map-based burster model proposed by Cazelles et al. [37]. It is a discontinuous map made up of four linear pieces. (d) Example orbit of the map in (c). (e) Double return map proposed by Aguirre et al. [38]. The return map is either the lower or the upper one depending on the value of s. When x falls in one of the dark gray areas, s switches to $s = 0$; in the light gray areas, to $s = 1$. (f) Example orbit of the map in (e).

D, falls in a small region above C, it ascends again, producing additional spikes in a burst. The system can switch chaotically between subthreshold oscillations and bursting, as seen in Fig. 19(f).

Although they are the simplest and most computationally efficient of all bursting models, these one-dimensional bursters have not been extensively used for modeling. The reason is their lack of robustness, with the need to fine-tune parameters to get the desired bursting, and the difficulty in relating them to biophysical properties. The slow and fast time scales of bursting neurons stem from different processes; one-dimensional bursters mix both in only one variable, and make it impossible to control them separately.

2.3. The Nagumo–Sato and Aihara models

A different approach to modeling dynamics of neurons by means of maps originates from the McCulloch–Pitts [26] formalism for artificial neurons, rather than from the electrophysiologically inspired Hodgkin–Huxley tradition. This type

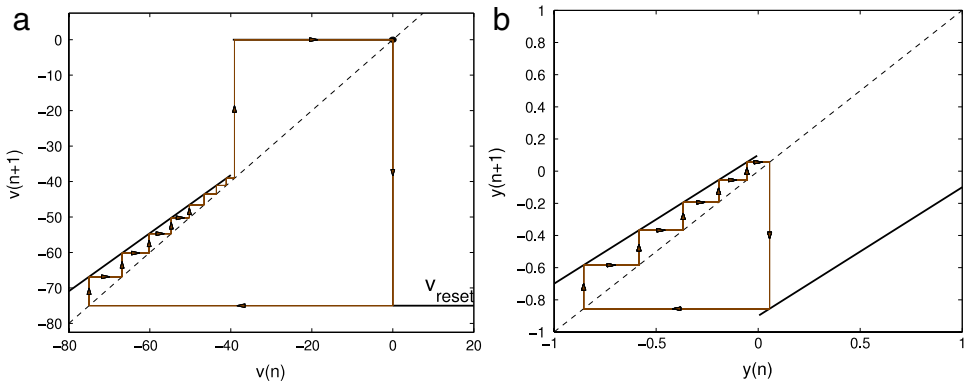

Fig. 20. (a) First return map of the map-based LIF model of Eqs. (5) with the same parameters as in Fig. 4, discretization step $\Delta t = 5$ and spike level $v_s = 0$. A cobweb of the unique periodic orbit of the system is superimposed on the diagram. (b) The same for the Nagumo–Sato model of Eqs. (23) with $k = 0.8$ and $a(n) = 0.1$.

of neuron model is best represented in the equations given by Caianiello [27], or, equivalently, by Nagumo and Sato [28]:

$$x(n+1) = H\left[S(n) - \alpha \sum_{r=0}^{n} b^{-r} x(n-r) - \theta\right]. \tag{22}$$

In Eq. (22), $H(x)$ is the Heaviside step function, $S(n)$ is the external stimulus at time n, θ is a threshold value for firing, and $x(n)$ represents the state of the neuron, which can only be, at each time step, 0 (not fired) or 1 (fired). Parameters $\alpha > 0$ and $b > 1$ regulate the refractoriness of the neuron. A neuron following Eq. (22) fires whenever external excitation is greater than θ, except when it has fired recently, in which case the refractory term makes the effective threshold higher.

The dynamics of the model can be best understood by means of a change of variables [27,28]. Indeed, if a new variable is introduced,

$$y(n) = \frac{S(n) - \theta}{\alpha} - \sum_{r=0}^{n} b^{-r} x(n-r),$$

Eq. (22) reduces to

$$y(n+1) = k y(n) + a(n) - H[y(n)], \tag{23}$$

where $k = 1/b$ and

$$a(n) = \frac{1}{\alpha}\left[\left(S(n+1) - \frac{S(n)}{b}\right) - \theta\left(1 - \frac{1}{b}\right)\right]$$

is the transformed stimulus. The firing state $x(n)$ can be immediately retrieved from $y(n)$, since $x(n) = H[\alpha y(n)] = H[y(n)]$. Whereas $x(n)$ represents the external, firing state of the neuron, $y(t)$ stands for an internal state that measures how close the neuron is to firing. Although originally from [27], the model of Eq. (23) is usually referred to as the Nagumo–Sato model [28].

Notice that Eq. (23) is almost identical to the discretization of the LIF model, Eq. (5). Parameter k may be identified in both models, while $a(n)$ in Eq. (23) is equivalent to the term $(1 - k)[RI(n) + E_L]$ in Eq. (5). The difference between them lies in the reset mechanism: the LIF model has a hard reset at a constant level, while in the Nagumo–Sato model the reset level depends on the state of the neuron before firing. Both maps are compared in Fig. 20, for constant inputs $I(n)$ and $a(n)$. Notice that the state variable y of the Nagumo–Sato model does not exhibit spikes; they show instead in the output variable $x(n) = H[y(n)]$. In the LIF model, the hard reset ensures that only one possible periodic orbit exists. But even without a hard reset, the Nagumo–Sato model exhibits the same property, because, with $k < 1$, the map is almost everywhere contracting, and all initial conditions converge to a unique stable periodic orbit. Nagumo and Sato [28] give a detailed description of the periodic orbits that correspond to different values of k and a.

A modification of the Nagumo–Sato model has been proposed by [29]. The Aihara model substitutes the Heaviside step function in Eq. (23) by a sigmoid:

$$\begin{aligned} y(n+1) &= k y(n) + a(n) - F[y(n)], \\ F(y) &= \frac{1}{1 + e^{-y/\sigma}}. \end{aligned} \tag{24}$$

The output of the model is $x(n) = F[y(n)]$. The sigmoid $F(y)$ has a sharp transition (σ is small), and the return map is very similar to that of the Nagumo–Sato model; compare Figs. 21(a) and (b). The idea behind this small change in the model is that spiking need not be an all-or-nothing event; for example, it is clearly graded under space clamp in the giant squid axon [63].

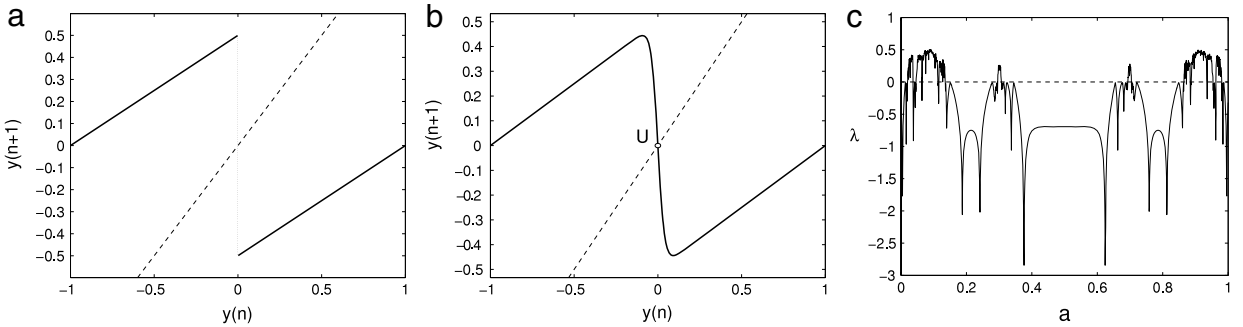

Fig. 21. (a) Return map of the Nagumo–Sato model of Eq. (23), with $k = 0.5$ and $a = 0.5$. The map has no fixed points, and all orbits are periodic. (b) Return map of the Aihara model of Eq. (24), with $k = 0.5$, $\sigma = 0.04$ and $a = 0.5$. U is an unstable fixed point. (c) Lyapunov exponent of the Aihara map with $k = 0.5$ and $\sigma = 0.04$ as a function of a. The Lyapunov exponent of the Nagumo–Sato map is everywhere $\lambda = \log k = -0.693$.

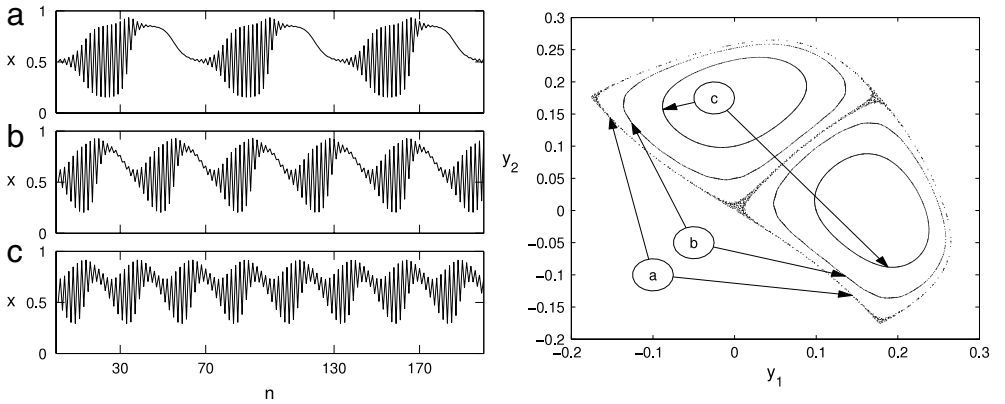

Fig. 22. Output variable $x(n)$ (left), and phase plane representation of orbits (right) of the modified Aihara model of Eq. (25) with $k_1 = 2$, $k_2 = 1$, $a = 0.5$ and $\sigma = 0.1$, for different initial conditions: (a) $y_1(0) = 0$, $y_2(0) = 0.01$; (b) $y_1(0) = 0$, $y_2(0) = 0.05$; (c) $y_1(0) = 0$, $y_2(0) = 0.1$. Notice that in the phase plane representation each orbit consists of two closed invariant curves; the orbit jumps between the two curves in consecutive time steps. According to [66].

A very narrow window of graded spiking responses, of the size of σ, is enough to turn the spiking sequence chaotic for certain ranges of external excitation a, because now the map is expanding in a finite interval of its domain; this can be seen in Fig. 21(c), where the Lyapunov exponent of the system [34] is depicted as a function of a. Positive values of the exponent imply chaos. Notice that the Lyapunov exponent of the Nagumo–Sato model is everywhere equal to $\log\, k < 0$, independent of the value of a; in the Aihara model, this value of the exponent is found in the plateau centered around $a = 0.5$ that can be seen in Fig. 21(c). The chaotic trains of spikes generated by the Aihara model for values of a that yield a positive Lyapunov exponent have indeed been observed in the giant axon of the squid [64]. The Aihara model is an interesting bridge between biological and formal neurons. A study of the dynamics of the Aihara model can be found in [65].

The Caianiello model could be reduced to a single variable because the refractory term in Eq. (22) was purely exponential. The term can be generalized to obtain models with additional dynamic properties, as proposed for example by Tanaka et al. [66]:

$$\begin{aligned} y_1(n+1) &= k_1 y_1(n) + k_2 y_2(n) + a - F[y_1(n)], \\ y_2(n+1) &= y_1(n). \end{aligned} \tag{25}$$

The additional variable y_2 acts as memory storage and allows the model to burst with appropriate parameter values. In particular, when $k_2 = 1$, a family of bursting orbits emerges along pairs of invariant curves that originate from a Neimark–Sacker bifurcation of a period-two stable orbit and are bounded by heteroclinic loops. Such orbits are depicted in Fig. 22. The period and duty cycle of the bursts can be controlled by choosing appropriate values of parameters [67], but, since they also depend very much on initial conditions, this model of bursting cannot be considered robust enough for biological modeling. Robust bursters based on the Aihara model add a third, slow variable to the system, and have been put forward by Kuva et al. [68] and Copelli et al. [69]. Bursting as a network effect with Aihara neurons is described in [70].

Interestingly, one-variable neuronal maps similar to the Aihara model are obtained by means of Poincaré sections of ODE-based systems. Medvedev [30] does so from the three-variable model excitable bursting cells proposed by Chay [71]. The Chay model has two fast variables, representing voltage and the proportion of open, voltage-dependent potassium channels, and one slow variable, representing intracellular calcium concentration. The model is a burster: with appropriate parameter

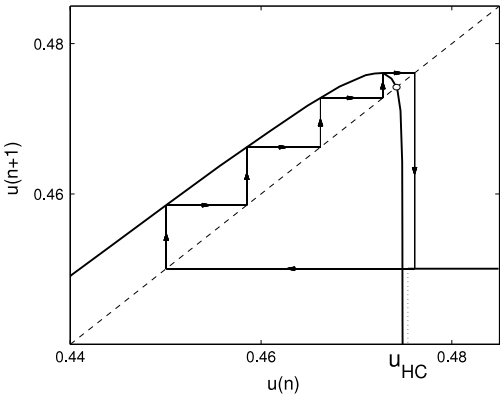

Fig. 23. Return map of the calcium concentration $u(t)$ obtained by Medvedev [30] from the ODE-based Chay neuron model. Each iteration $u(n)$ of the map represents the value of calcium concentration after one spike, or after the quiescent period following the end of a burst. The depicted superstable orbit corresponds to a periodic bursting regime of the ODE-based model with four spikes per burst.

values, the concentration of calcium builds up as the neuron spikes and, by activating calcium-dependent potassium channels, terminates the burst; while the neuron is silent, calcium concentration decreases, deactivating potassium channels and allowing spiking once again. By averaging the variation in calcium concentration due to each spike, Medvedev obtains a one-dimensional return map for this variable and is able to study its bifurcations as parameters of the neuron model undergo variation. The map is depicted in Fig. 23. The similarity with the Aihara map of Fig. 21(b) is apparent. An almost linear, build-up piece for low values of u, the calcium concentration, with slope lower then unity, is followed by a sharp downturn, sigmoid-like, and then by another linear, horizontal or almost horizontal piece. As parameters in the model change, these overall features of the map remain unchanged, but, as in the Aihara model, its position relative to the diagonal shifts, giving rise to bifurcations. Touboul and Brette [31] get a similar map from two-dimensional IF models (the ODE-based counterparts of models in Section 2.1) when the reset voltage is above the bounded basin of attraction of the stable fixed point of the system; in this case, the mapping is on the recovery variable.

2.4. The netlet model

The last model we are going to introduce goes a step further in abstraction, since it represents not a single neuron but a whole population. A clear formulation was given by Harth et al. [72] and Anninos et al. [73], following earlier work on neural nets [74,75]. The single variable in the model, $\alpha(n)$, represents the average activity of a pool of excitatory and inhibitory neurons forming an anatomical unit they call *netlet*, as suggested by the discoveries of [76] and [77]. The time step is made equivalent to the refractory period of neurons, so that each neuron can fire only once per timestep, and must be silent immediately afterwards. The average activity $\alpha(n)$ is then simply the fraction of neurons that have spiked during the n-th time step. The basic netlet equation is:

$$\alpha(n+1) = [1-\alpha(n)]P[\alpha(n)], \tag{26}$$

where the $(1-\alpha)$ factor represents refractoriness, while $P(\alpha)$ is the probability that a non-refractory neuron will receive inputs that make it spike at time step $n+1$. To derive it, neurons are assumed to be simple thresholding units that fire whenever the sum of excitatory inputs during a time step, minus the sum of inhibitory inputs, exceeds threshold. Another key assumption is that all neurons in the netlet share a random distribution of connections, so that the postsynaptic potentials generated by a spike are distributed in a probabilistic manner among them. Different distributions produce slightly different return maps [75,39,78–80]. For the sake of illustration, a Poisson distribution [73] results in

$$P(\alpha) = e^{-\alpha h\mu^-} \sum_{m=0}^{M} \frac{(\alpha h\mu^-)^m}{m!} \cdot \left[1 - e^{-\alpha(1-h)\mu^+} \sum_{l=0}^{\eta(m)} \frac{(\alpha(1-h)\mu^+)^l}{l!}\right], \tag{27}$$

where h is the fraction of inhibitory neurons in the netlet, μ^+ and μ^- the average number of outgoing connections from each excitatory and inhibitory neuron, respectively, and $\eta(m)$ the number of excitatory postsynaptic potentials that place a neuron above threshold, assuming it receives m inhibitory postsynaptic potentials in the same time step. M is a large integer to make sure neglected terms are insignificant. Additional terms, not shown, are necessary to include an external excitation parameter σ, measuring the number of external excitatory spikes each neuron receives on average during each time step.

The closed form of the map allows analytical investigation of the dynamical properties of the system [73]; a picture of the map is enough for our purposes, however. It is depicted in Fig. 24 for three different values of external excitation. At low excitation (dashed line), the return map lies completely below the diagonal, and activity in the netlet rapidly goes to 0 for any initial condition. At an intermediate value, the familiar saddle–node bifurcation has taken place, forming two stable

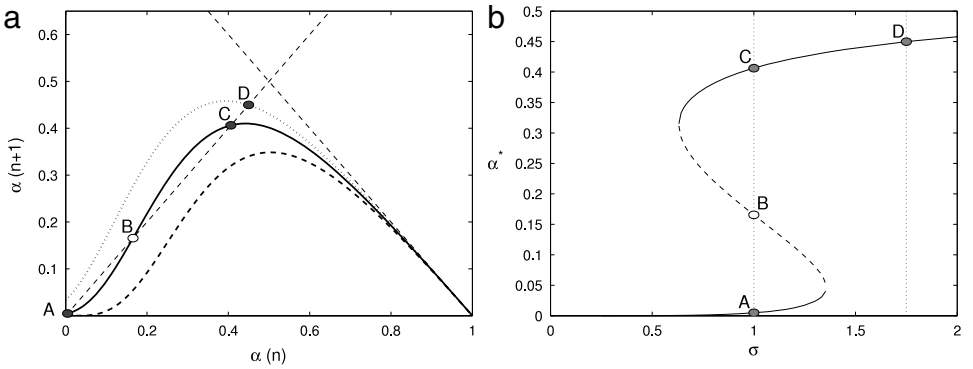

Fig. 24. (a) Return map of the netlet model for three values of external excitation σ: 0 (dashed line), 1 (solid) and 1.75 (dotted). (b) Bifurcation diagram of the netlet map against excitation, showing hysteresis. The curves of stable fixed points are solid, of unstable points dashed. Labeled points correspond to those in (a). Parameters of the netlet are 10% inhibitory neurons ($h = 0.1$), $\mu^+ = \mu^- = 15$ connections per neuron, and $\eta(0) = 5$, with excitatory, inhibitory and external postsynaptic potentials having equal amplitude.

fixed points: A, close to 0, and C, where significant activity is sustained. Whether one or the other final state is reached depends on whether the initial condition is below or above the unstable fixed point B. Finally, for high external excitation only the high-activity point D remains. Thus, the netlet can act as a switch with memory of past inputs. Multiple hysteresis loops may form in the netlet if it includes neurons with differing thresholds [81].

Notice in Fig. 24(a) that the return map never crosses the $1 - \alpha$ line (the dashed diagonal with negative slope). This is due to the absolute refractory term in Eq. (26). As a result, high-activity fixed points, such as C and D in the figure, never undergo a flip bifurcation that would turn them unstable and start a cascade of period-doublings. Activity always converges to those points by way of damped oscillations. The limitation imposed by absolute refractoriness proves therefore very restrictive, and modified models open up the possibility of richer dynamical regimes. Lee and Yi [82] derive an exponential netlet map from some reasonable assumptions. Others [83–85] take a purely phenomenological approach and turn to the well-known logistic map [86]. These maps, like the refractory netlet formulations, are unimodal and can be controlled by a parameter representing external input. Unlike the netlet map, they undergo the full cascade of period doublings towards chaos as excitation grows. Some support for chaotic netlet models can be found in Poincaré sections of some Hodgkin–Huxley formulations of network interactions [87].

3. Dynamic properties of isolated map-based neuron models

In the preceding section we have described the most salient properties of the models, and now we will examine more closely the dynamical properties of the two-dimensional, IF-inspired family introduced in Section 2.1 which, for their versatility and rich repertoire of behaviors, have been the object of abundant research. A systematic, very helpful examination of the continuous-time counterparts can be found in [45,31].

3.1. Bursting and adaptation

The fast–slow decomposition characteristic of two-dimensional map-based models of the integrate-and-fire family, described in Section 2.1, allows for an easy understanding of some important dynamical properties, such as bursting and adaptation. The fast subsystem is analyzed separately, assuming a constant value of the slow variable, which plays the role of a parameter.

To begin with bursting, let us consider, for the sake of definiteness, that the v equation (fast subsystem) of Eqs. (7) has the form of the Izhikevich model, given in Eq. (12), with $c = -55$:

$$v(t+1) = \begin{cases} \min(0.04v^2 + 6v + 140 + I - \gamma, 30), & v < 30, \\ -55, & v \geq 30. \end{cases} \tag{28}$$

Here γ stands for the slow variable u. Let us now suppose that $I - \gamma$ is such that this QIF map has no fixed points and therefore follows a periodic spiking orbit, as depicted in the return map of Fig. 25(a). Suppose in addition that the equation for u in the full system (7) is such that, following Eq. (10), γ increases whenever v is above the value $v = -60$ and decreases when it is below. Since $v_{\text{reset}} = -55$ is above that level, while v is spiking γ will increase and, according to Eq. (28), the return map will shift down and go through the saddle–node bifurcation that creates a stable–unstable pair of fixed points [Fig. 25(b)]. The neuron continues to spike, γ to increase and the return map to shift down until the unstable fixed point has moved to $v = -55$, where the periodic spiking orbit turns homoclinic [Fig. 25(c)]. Then, as γ grows further and the return map sinks lower, the orbit of v is attracted towards the stable fixed point s and the neuron becomes silent. But since s lies at a value of $v < -60$ (notice that the saddle–node bifurcation takes place at $v_{sn} = -62.5$), now γ begins to decrease and the return map to shift upwards, with the orbit v closely following the slow motion of s [Fig. 25(d)], until the saddle–node

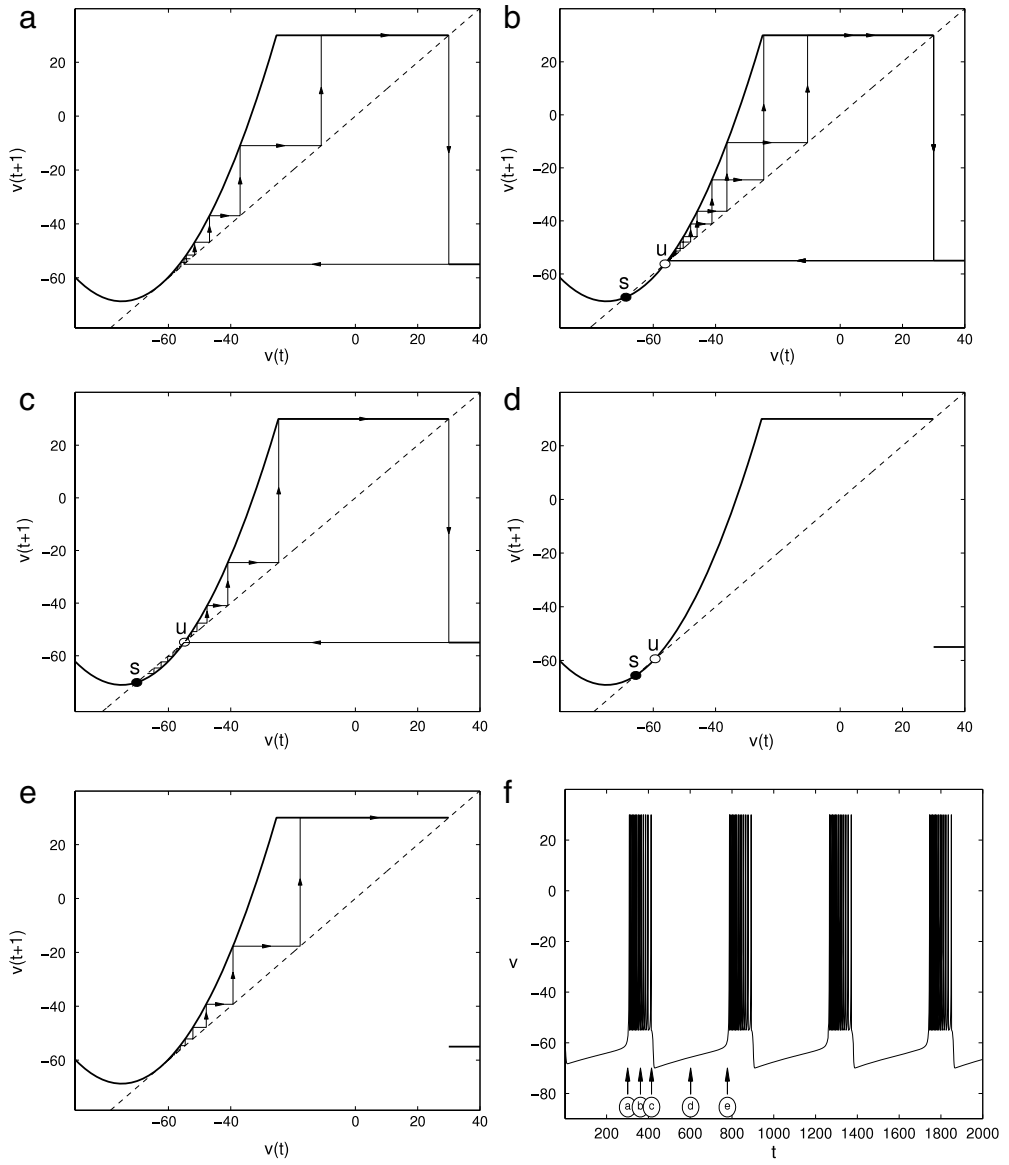

Fig. 25. (a) to (e) Return map of the fast subsystem of Eqs. (28) for values of γ corresponding to different phases of bursting, as explained in the text. (f) Time evolution of v along a bursting orbit. The instants corresponding to the different stages depicted in (a)–(e) are indicated.

bifurcation is crossed once again and the orbit escapes towards the spiking cycle [Fig. 25(e)]. All in all, the orbit consists of alternating silent and spiking phases, as shown in Fig. 25(f). That is bursting.

It is now easy to understand the complete two-dimensional dynamics of bursting. Fig. 26(a) and (c) show two bursting orbits superimposed on the two-dimensional nullcline diagram of the Izhikevich model. In Fig. 26(a) the value of injected current I is such that the two fixed points of the system have disappeared through a saddle–node bifurcation ($I = 2$; compare to Fig. 10). The M_{spikes} manifold lies completely above the slow nullcline, while the stable branch of the slow manifold N_s lies completely below. This justifies the slow variable dynamics explained in the preceding paragraph, and guarantees a bursting orbit. Since the bursts begin at a saddle–node (also called fold) bifurcation and end at a homoclinic bifurcation of the fast subsystem, the Izhikevich model belongs to the category of *fold/homoclinic* bursters [60]. Note, however, that bursts do not terminate precisely at $u = u_h$, due to the finiteness of a.

With a stronger external input, as in Fig. 26(c), M_{spikes} intersects the slow nullcline, creating a fixed point of the averaged slow subsystem of Eq. (10) and giving birth to a spiking orbit [Fig. 26(d)]. Indeed, observe that a necessary condition for bursting is that the saddle–node bifurcation takes place at a voltage below the minimum of the spiking cycle. That is, there must be a range of values of γ where the stable fixed point s and the stable spiking cycle coexist. Otherwise, in the $\epsilon \to 0$ limit, when the saddle–node pair disappears the return map will not shift upwards any further and the system will stick to either the spiking or the silent regime.

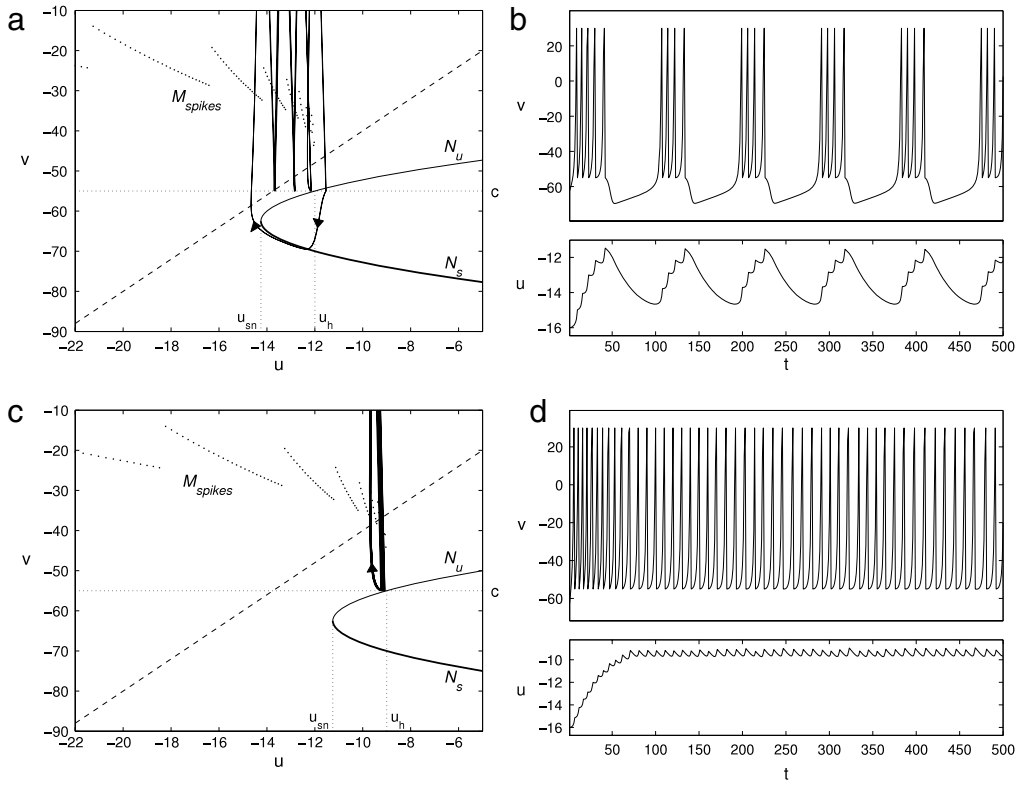

Fig. 26. (a) Nullcline diagram of the Izhikevich neuron model of Eqs. (11) in a bursting regime. Labels have the same meaning as in Fig. 10, and parameters are the same as there, except for $I = 2$. Part of an orbit is superimposed on the diagram. (b) Time evolution of v and u for the orbit in (a). (c) Same as in (a) for a spiking regime, $I = 5$. (d) Time evolution of v and u for the orbit in (c).

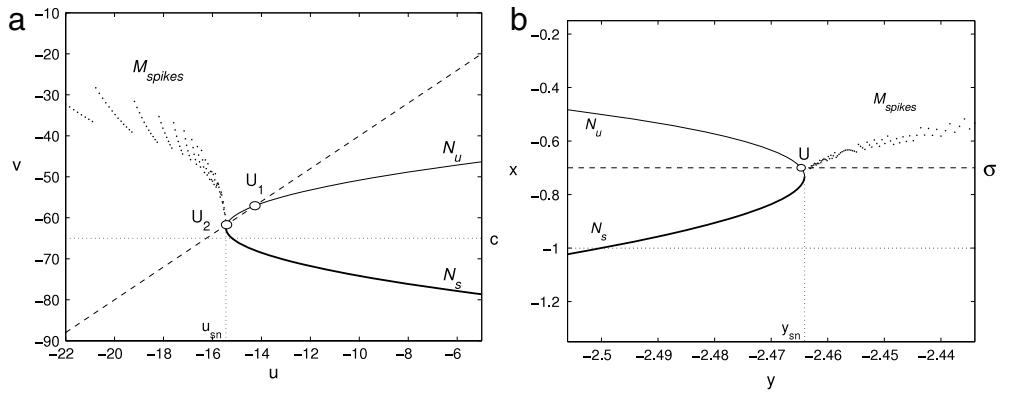

Fig. 27. (a) Nullcline diagrams of the Izhikevich neuron model with the same parameters as in Fig. 10(d), except $c = -65$. Since the intersection of the reset level (dotted horizontal line) with the fast nullcline lies at N_s, no homoclinic orbit exists in the fast subsystem. M_{spikes} now terminates at the N_s–N_u vertex, and bursting is impossible. (b) The same for the non-chaotic Rulkov model, in this case with $\alpha = 3$.

An important feature of the above examples from the point of view of modeling is that, as the injected current I increases, the neuron goes from silence to bursting to spiking. This is observed in some types of neurons, such as those of the pre-Bötzinger complex [88]. But many neuron types are incapable of bursting, and switch directly from silence into spiking. Since, as we know, the possibility of bursting depends on the existence of a region of bistability of the fast subsystem between u_h and u_{sn}, in order to eliminate bursting we must move u_h by changing the reset level c. In fact, when $c < v_{sn} = -62.5$, as in Fig. 27(a), M_{spikes} ends precisely at the vertex (u_{sn}, v_{sn}). Therefore, the slow nullcline intersects either N_s, and the neuron is silent, or M_{spikes}, and the neuron goes to a spiking regime. In the Rulkov family of models, the reset level is fixed, but its position relative to the saddle–node point can be adjusted by means of parameter α. A value $\alpha < 1$ in the supercritical model, and $\alpha < 4$ in the chaotic and the non-chaotic models [Fig. 27(b)], makes bursting impossible, forcing the direct transition from silence to spiking.

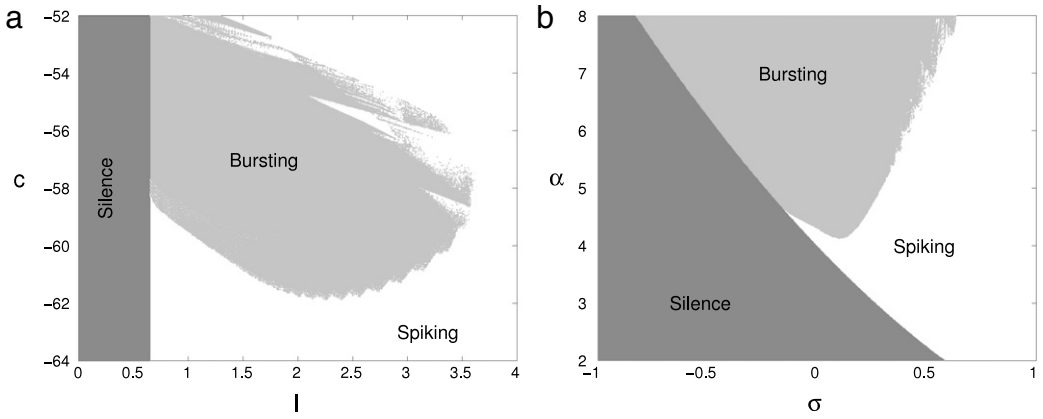

Fig. 28. (a) Types of steady-state activity in the Izhikevich model with $a = 0.02$, $b = 0.25$ and $d = 0$, as a function of external input I and reset level c. Depending on c, as I increases, the model can go from silence to bursting to spiking, or directly from silence to spiking. (b) The same in the Rulkov model, with $\mu = 0.001$, as a function of external input σ and parameter α.

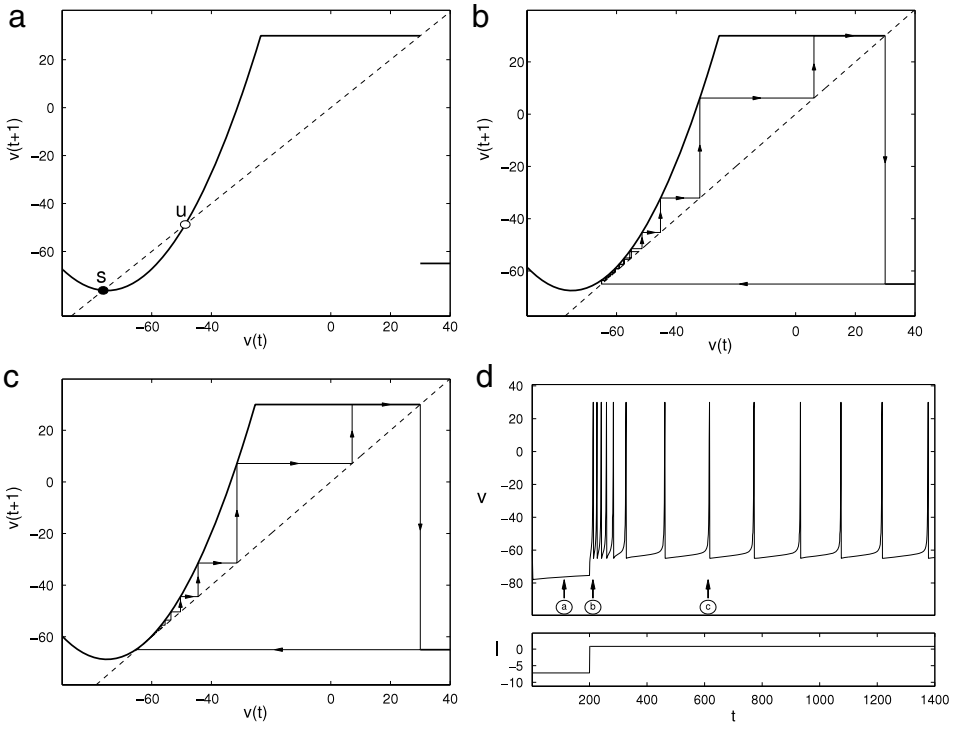

Fig. 29. (a) to (c) Return map of the fast subsystem of Eq. (28) for values of γ corresponding to different phases of spike frequency adaptation, as explained in text. (d) Time evolution of v and of external current I along a spike frequency adaptation routine. The instants corresponding to the different stages depicted in (a)–(c) are indicated.

The above explanations are valid in the $a \to 0$ limit. With finite a, the transition from silence to spiking or bursting is not so clear-cut, and the separation of bursters from non-bursters at $c = -62.5$ (in the case of the Izhikevich model) is merely an approximation; in fact, with a finite a, bursts of only one spike may appear at values of c well above that. Fig. 28(a) and (b) provide a rough summary of parameter regions of silence, spiking and bursting, for the Izhikevich and non-chaotic Rulkov models. Notice the similar roles of (I, c) in the Izhikevich model and (σ, α) in the Rulkov model. The boundary between silence and either spiking or bursting lies at the Neimark–Sacker bifurcation; the boundary between spiking and bursting is rather arbitrary (a criterion based on the spread of the interspike intervals has been used here), but clearly no bursting is to be found below $c = -62.5$ in the Izhikevich model, or $\alpha = 4$ in the Rulkov model.

As for spike frequency adaptation, let us take again the Izhikevich fast subsystem, Eq. (28), but suppose that the reset voltage is now $c = -65$. Let $I - \gamma$ be such that the system is resting at the stable fixed point s, as in Fig. 29(a), with γ neither

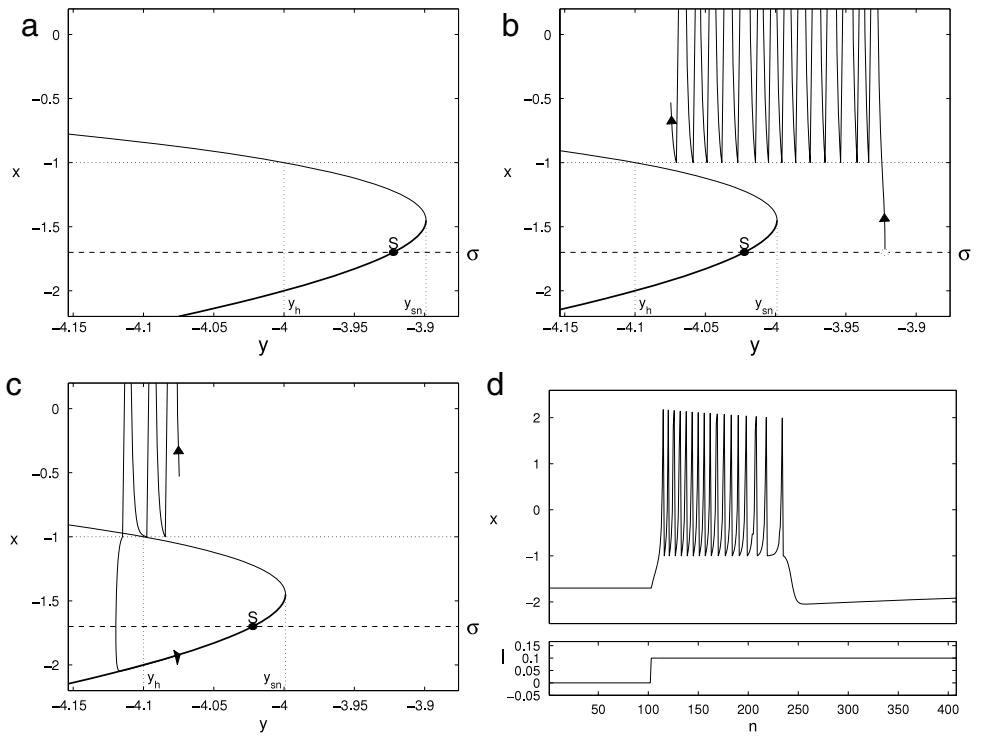

Fig. 30. Orbit of a Rulkov neuron subjected to a step in input current I. (a) Before the current step; neuron resting at S. (b) Immediately after current step; the neuron jumps into spiking. (c) End of spikes and return to stable fixed point S. (d) Full time evolution of x and external current. Parameters of the model in Eqs. (13) are $\alpha = 6$, $\mu = 0.001$, $\sigma = -1.7$.

increasing nor decreasing. If a sudden step in I comes, the return map will immediately shift up across the saddle–node bifurcation, the stable fixed point will disappear, and the neuron will begin to spike [Fig. 29(b)]. This will cause γ to increase and the map to slowly shift downwards. But if the slow subsystem is such that, with the new values of u, the slow variable itself increases only as long as v is above -60, for example, the return map will cease to shift at some point before the saddle–node bifurcation happens again. This is because, as the return map approaches the $v(t+1) = v(t)$ line, the orbit stays longer and longer close to the saddle–node value of $v_{sn} = -62.5$, and therefore at some point the average value that dictates the dynamics of the slow variable will fall below -60. A stable spiking orbit [Fig. 29(c)] for the full system of Eq. (7) sets in. Since the spiking frequency just after the external input step was higher than at the final steady state, the firing rate of the neuron has adapted.

The Rulkov model exhibits the same adaptation mechanism, but it is worth noting that the horizontality of its slow nullcline makes it an extreme case. In fact, changes in I can only have transient effects upon the Rulkov system: the horizontal shift of the fast nullcline does not alter its position relative to the slow nullcline. This is illustrated in Fig. 30, where the response of a quiescent Rulkov neuron to a step in input current I is depicted. Initially [Fig. 30(a)] the neuron is at rest at the stable fixed point S. When the current step comes [Fig. 30(b)], S and the whole fast nullcline shift leftwards, and the state jumps upwards to begin spiking. Since the stable point is globally attracting, the burst will die later [Fig. 30(c)] and the neuron slowly returns to the same point, only with a different value of y. All in all, injection of steady currents provokes a merely transient response [Fig. 30(d)]. Compare this total adaptation to the spike frequency adaptation of the Izhikevich model (Fig. 29). This insensitivity to DC currents in the Rulkov model can be made to emerge explicitly in its equations by means of a change of variables [89]. If in Eq. (13) the substitution $y(n) + I(n) \equiv z(n)$ is introduced, the system transforms into

$$x(n+1) = F[x(n), z(n)],$$
$$z(n+1) = z(n) - \mu[x(n) - \sigma] + I(n) - I(n+1),$$

whereby $I(n)$ disappears from the fast subsystem and *only its derivative* enters the slow subsystem as an additional excitation. The model is therefore unresponsive to low frequency input currents. This frequency selectivity is reconsidered in Section 3.2.

Similar explanations may be given for all the behaviors depicted in Fig. 9, taking as the point of departure a particular realization of the generic model of Eq. (7). For a thorough study, in continuous-time, refer to [31].

3.2. Resonance, oscillations, and the integrator versus resonator trade-off

We have already mentioned that the two-dimensional IF-based models introduced in Section 2.1 exhibit preferential amplification of inputs at particular frequencies, that is, resonant behavior. A basic understanding of the mechanism underlying this property can be gained by turning to the so-called linear resonate-and-fire [60], or generalized integrate-and-fire [90], model. It is built by adding a second linear equation to the LIF model. The equations of the map-based linear resonate-and-fire model are

$$\begin{bmatrix} v(t+1) \\ u(t+1) \end{bmatrix} = \begin{cases} \begin{bmatrix} v(t) + \mu_1(bv(t) - \omega u(t) + I) \\ u(t) + \mu_2(\omega v(t) + bu(t) - \sigma) \end{bmatrix} & \text{if } v(t) < \theta, \\ \begin{bmatrix} v_s \\ u(t) \end{bmatrix} & \text{if } \theta < v(t) < v_s, \\ \begin{bmatrix} v_{\text{reset}} \\ u_{\text{reset}} \end{bmatrix} & \text{if } v(t) \geq v_s. \end{cases} \tag{29}$$

It is a linear two-dimensional map with a threshold in the v variable, which again represents membrane potential. It is immediately apparent that this model fits the generic equations (7) for two-dimensional map-based models derived from the IF family. Here we just drop the condition of separation of time scales: parameters μ_1 and μ_2 may be of the same order. The rationale for the peculiar arrangement of the terms is that, when $\mu_1 = \mu_2$ and both are small, and if $b < 0$ and $\omega > 0$, it represents an Euler discretization of a linear two-dimensional system with a stable focus of angular frequency ω and decay rate b. The name of the model comes from its resonance properties, as depicted in Fig. 31. Using σ as external input, we may induce a spike if we inject a sufficiently strong pulse, as in Fig. 31(a). But we may also do it by means of two weaker pulses with the appropriate timing, as in Fig. 31(b). The interval between pulses is close to the intrinsic period of oscillation of the system, which, as straightforward linear analysis shows, is, when $\mu_1 \approx \mu_2$,

$$T_r \approx 2\pi \frac{1 + b\bar{\mu}}{\omega\bar{\mu}},$$

with $\bar{\mu} = (\mu_1 + \mu_2)/2$. Thus, although the first pulse is unable to elicit the spike, the second one adds to the first one period later and does the trick. If the second pulse comes too late or too soon, as in Fig. 31(c), the amplitude of oscillation will not be enough to cross the threshold and no spikes are generated.

Therefore, the response of resonate-and-fire neurons is selective to input frequency. This is the definition of a resonator. One-dimensional integrate-and-fire models, instead, are integrators: they add up their inputs and fire if the accumulated effect exceeds threshold. They do have a proper time scale, given by their decay rate toward stable equilibrium, and pulsed inputs with a frequency significantly lower than this rate will fail to accumulate; they are high pass filters. But in the case of the RF model, in addition to the decay rate we have an intrinsic oscillation frequency that makes it selective to a narrow range of frequencies: it is bandpass. Note that in Fig. 31(c) the neuron fails to spike even though pulses are less far apart than in Fig. 31(b). This can never happen in a one-dimensional IF model.

Now we may return to the fast–slow map-based models introduced in Section 2.1 and described by Eq. (7). We see there that ϵ and q are just convenient rearrangements of parameters b, ω and μ_2 in Eqs. (29), and that the fast–slow time scale translates into $\mu_2 \ll \mu_1$. The separation of time scales does not preclude resonance, but forces the subthreshold oscillations to follow the slow time scale. Indeed, if we linearize the fast subsystem around the fixed point(s), we obtain equations equivalent to Eqs. (29). It is straightforward to show [51] that the fixed points undergo a Neimark–Sacker bifurcation when external currents I or σ change, and that the angular frequency of oscillations that are born satisfies

$$\omega^2 \equiv \epsilon(1 - \epsilon q^2) > 0. \tag{30}$$

The condition $\omega^2 > 0$ will be satisfied as long as $\epsilon \ll 1$, as assumed in the generic model. Frequency is thus of the order of ϵ, and oscillations follow slow time.

Depending on whether the Neimark–Sacker bifurcation is super- or sub-critical, self-sustained subthreshold oscillations may or may not appear. For example, the Izhikevich model, as well as the chaotic and the non-chaotic Rulkov models, are subcritical and do not sustain subthreshold oscillations at typical parameter values. The supercritical Rulkov model, as implicit in its name, does. The difference in the bifurcations is depicted in Fig. 32 for the Izhikevich and supercritical Rulkov models.

Sustained subthreshold oscillations are an extreme form of resonance: the system oscillates at a preferred frequency in the absence of any external input. More generally, resonance is a graded property, and can be quantified by several measures, such as the quality factor, in the case of linear systems. Interestingly, in the family of two-dimensional map-based models encapsulated by Eqs. (7), the property of resonance is negatively correlated to another very important property, namely the sensitivity of the neuron to external currents. We have explained in Section 3.1 how the horizontal slope of the slow nullcline of the Rulkov model made it insensitive to steady changes of the external current I; more generally, the steeper the nullcline, the more sensitive the neuron is. At the same time, it can be shown that the linear quality factor, and the subcritical–supercritical character of the Neimark–Sacker bifurcation, depend on the slope of the slow nullcline in the

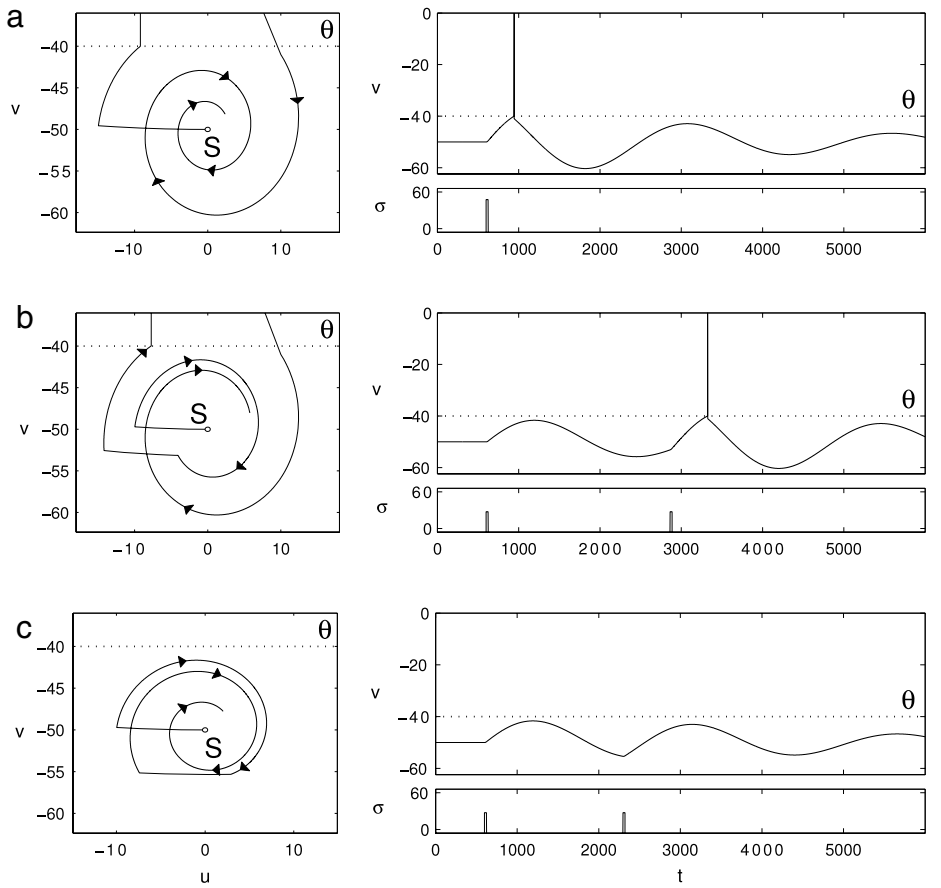

Fig. 31. Phase plane diagrams (left) and evolution in time of variable v (right) of the resonate-and-fire map-based model given by Eqs. (29), with $b = -0.03$, $\omega = 0.25$, $\mu_1 = \mu_2 = 0.01$, $\theta = -40$, $v_s = 0$, $v_{\text{reset}} = -41$, $u_{\text{reset}} = 10$, $I = 1.5$. Input σ, shown below the v trace, acts as an external pulsed input. S marks the stable fixed point of the system. Notice that input pulses produce strong horizontal deflections in the phase plane. (a) One strong input pulse. (b) Two weaker input pulses at a near-resonant frequency. (c) Two non-resonant pulses. According to Izhikevich [60].

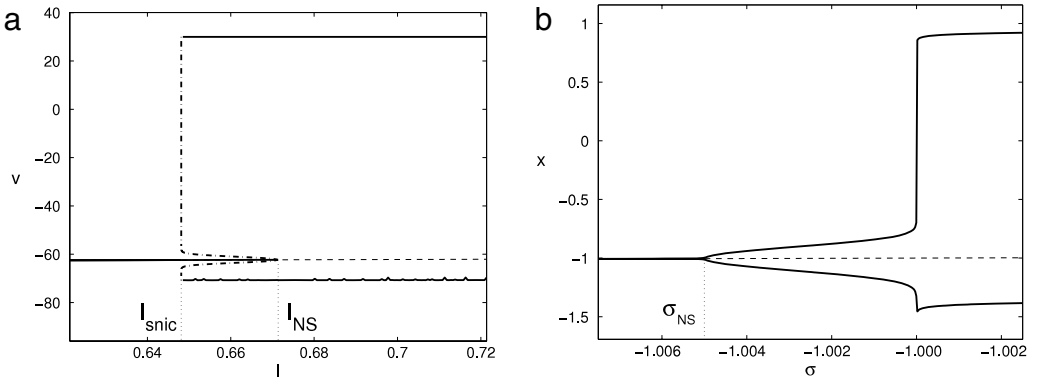

Fig. 32. Maximum–minimum bifurcation diagrams of the fast variable of (a) the Izhikevich neuron map, Eqs. (11), against excitation parameters I, and (b) the supercritical Rulkov map, Eqs. (17) and (13), against excitation parameter σ. Continuous lines represent stable fixed points or invariant curves, the dashed line represents unstable fixed points and dash-dotted lines correspond to unstable invariant curves. I_{NS} and σ_{NS}, Neimark–Sacker bifurcations. I_{snic}, saddle–node of invariant curves.

opposite way: the steeper slope corresponds to less selective resonance. Fig. 33 shows how, in the case of the Izhikevich model, sensitivity increases with nullcline slope (given by $1/b$) while the resonance quality factor decreases.

The trade-off between sensitivity and resonance is a general property of two-dimensional models based on slow–fast decomposition; it is a clear demonstration of the resonator/integrator opposition, and is explained in some detail in [51]. The Rulkov model, with its horizontal slow nullcline, displays sharp frequency selectivity, as shown by Bazhenov et al. [89],

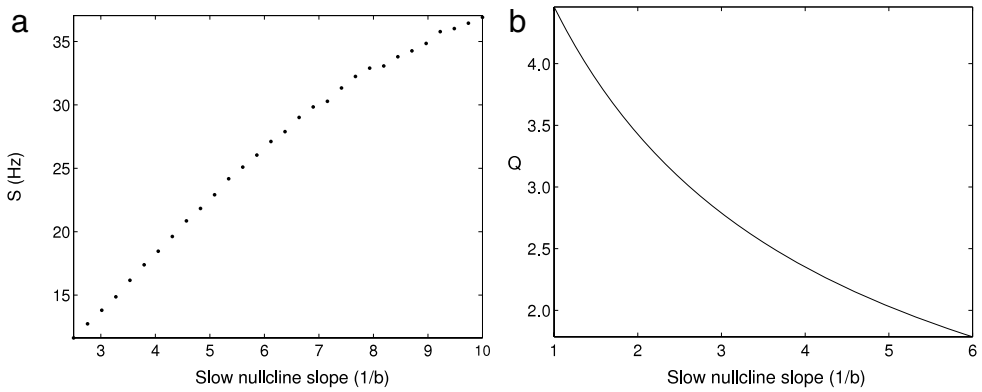

Fig. 33. (a) Sensitivity of the Izhikevich model, measured as the increase in firing rate per external current unit (regression average for I between $I_{NS}+0.5$ and $I_{NS}+1.5$), as a function of the slope of the slow nullcline ($1/b$). Frequencies are given in Hz, considering a time step of 1 ms. Current intensities have no units. Other parameters of the Izhikevich model of Eqs. (11) are $a=0.02$ and $c=-65$. (b) Q-value of the impedance curves as a function of $1/b$, with a constant resting potential $v^*=-62.7$ and $\omega^2=a(b-a)=0.005$.
Source: From Ibarz et al. [51].

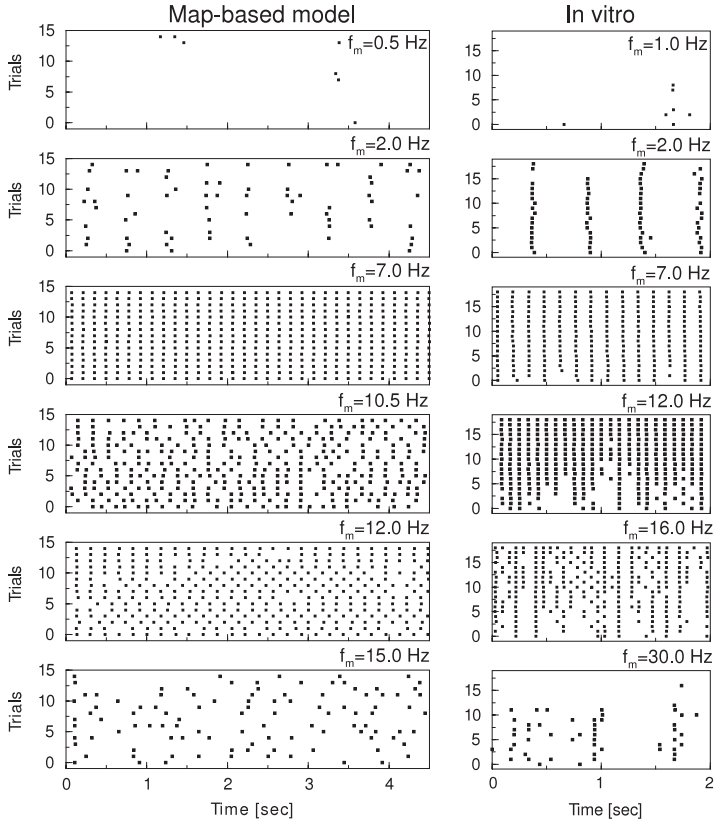

Fig. 34. Spiking of a non-chaotic Rulkov neuron (left panels) and of a RS cell of rat prefrontal cortex (right panels) in response to frequency modulated Poisson-type inputs, for 16 trials and six different modulation frequencies. The time equivalence for the Rulkov model is 0.5 ms per time step.
Source: From Bazhenov et al. [89].

where a non-chaotic Rulkov neuron is compared to a cortical neuron in its response to sinusoidally modulated stimuli. The comparison can be seen in Fig. 34. Both in regular-spiking rat cortical neurons *in vitro* and in the Rulkov model, the injection of Poissonian spike trains with a periodically modulated rate induced reliable, phase-locked responses at intermediate modulation speed (7–12 Hz), but only sparse and uncorrelated firing when the modulating sinusoid had either lower or higher frequencies.

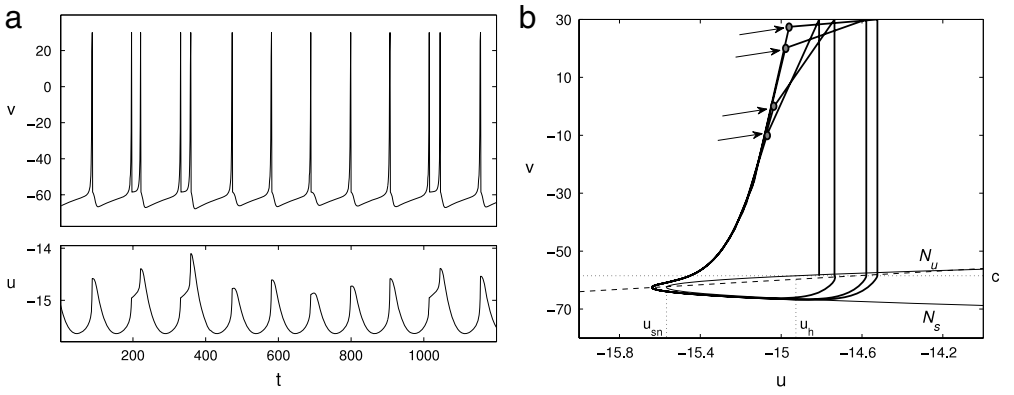

Fig. 35. (a) A chaotic orbit of the Izhikevich neuron model with $a = 0.02$, $b = 0.25$, $c = -58.5$, $d = 0$, and $I = 0.6828$. Slightly irregular spiking alternates unpredictably with bursts of two spikes; the irregularity is best noticed in the u variable. (b) The phase plane for the orbit in (a). A stretch of the orbit comprising four successive spikes is superimposed. The gray dots pointed to by the arrows are the last iterates before each spike; notice how the unpredictable spread of u values of each spike depends on how far this iterate is from threshold, which is a pure artifact of discretization.

3.3. Chaos

There exists experimental evidence of chaotic behavior in the spike trains of several types of neurons [91]. Whether the chaotic features of neuronal dynamics are functionally significant is still contested. At any rate, map-based neuron models are ideally suited to incorporate chaos at a minimal computational cost, and indeed a majority of map-based neuron models are designed specifically for this. Among the two-dimensional, slow–fast bursting models, the chaotic Rulkov model (Section 2.1.2), the Courbage–Nekorkin–Vdovin (CNV) model (Section 2.1.3) and the Chialvo model (Section 2.1.4) are fundamentally chaotic models. Their main chaotic features stem from their fast subsystems, with Rulkov and Chialvo using a smooth unimodal map and CNV a Lorenz-type map. These differences have an influence on the distribution of spike frequencies and amplitudes inside each burst, and on the distribution of burst lengths. Another chaotic model, the Aihara model (Section 2.3), tries to encapsulate in the simplest possible way the origin of chaotic trains of spikes in non-bursting neurons.

But even the map-based models that are not specifically conceived to display chaotic behavior can do so under certain circumstances. The source of chaotic behavior in these cases is the process of discretization. Indeed, all the two-dimensional map-based models derived from the IF family described in Section 2.1 exhibit chaotic orbits in some intervals of parameter values.

One form of chaos stems from the discontinuity of the threshold-and-reset mechanism. This feature is common to both map-based and continuous-time two-dimensional IF models [92,31]. According to the Poincaré–Bendixson theorem, chaos is not possible in continuous ODE-based two-dimensional systems. However, the discontinuous reset can work as a proxy for a third dimension, allowing the crossover of nearby trajectories to produce chaotic responses in a manner akin to smooth neuron models with three or more variables, such as the Hindmarsh–Rose model [93]. In the map-based case, this source of chaos is compounded, and usually overwhelmed, by the discretization of time steps. Fig. 35(a) represents a chaotic orbit of the Izhikevich model. The seemingly unpredictable sequence of spikes per burst and interspike intervals (best appreciated in the course of the slow variable) is suggestive of chaos. When we look at the phase plane [Fig. 35(b)] we see that the source of the irregularity lies in discretization: the recovery variable u receives, in the iterate immediately preceding a spike, a discrete "kick" of a size that depends on the particular value of v in that step. In continuous time systems there would be no such differences, and spiking would be strictly periodic.

Therefore, when confronted with an irregular orbit of a simple map-based model, the question arises not only as to whether the orbit is actually chaotic (as opposed to transient, or very long periodic), but also whether the chaos is meaningful or a mere artifact of discrete integration. A simple way to address both questions is to reduce the dimensionality of the system by constructing an *adaptation map* [31]. A *spiking* adaptation map $u(T_{i+1}) = \Phi_S[u(T_i)]$ is the value of the recovery variable u at the moment of the first spike after iterating the system from $(v, u) = (v_{\text{reset}}, u(T_i))$; in other words, it represents the change in the slow variable from one spike to the next. Fig. 23 was an example of such a map. If we are interested in the dynamics of bursts, we can build instead a *bursting* adaptation map $u(T_{i+1}) = \Phi_B[u(T_i)]$, by iterating again from $(v, u) = (v_{\text{reset}}, u(T_i))$ but waiting for the first spike *after* v *falls below the fast nullcline vertex* (signifying that a new burst has started). If either map is well defined in an interval of u values that covers the range of the system orbit, it will completely determine the dynamics of the neuron: a fixed point of the adaptation map corresponds to a periodic orbit of the full system; chaos in the adaptation map implies chaos in the full system. Fig. 36 illustrates by this method how the chaotic orbit in Fig. 35 is born: the bursting adaptation map, at a slightly lower value of excitation [Fig. 36(b)], has a stable fixed point, and the neuron spikes periodically. However, as excitation increases, the adaptation map undergoes the canonical period-doubling cascade of bifurcations and chaos ensues [Fig. 36(d)].

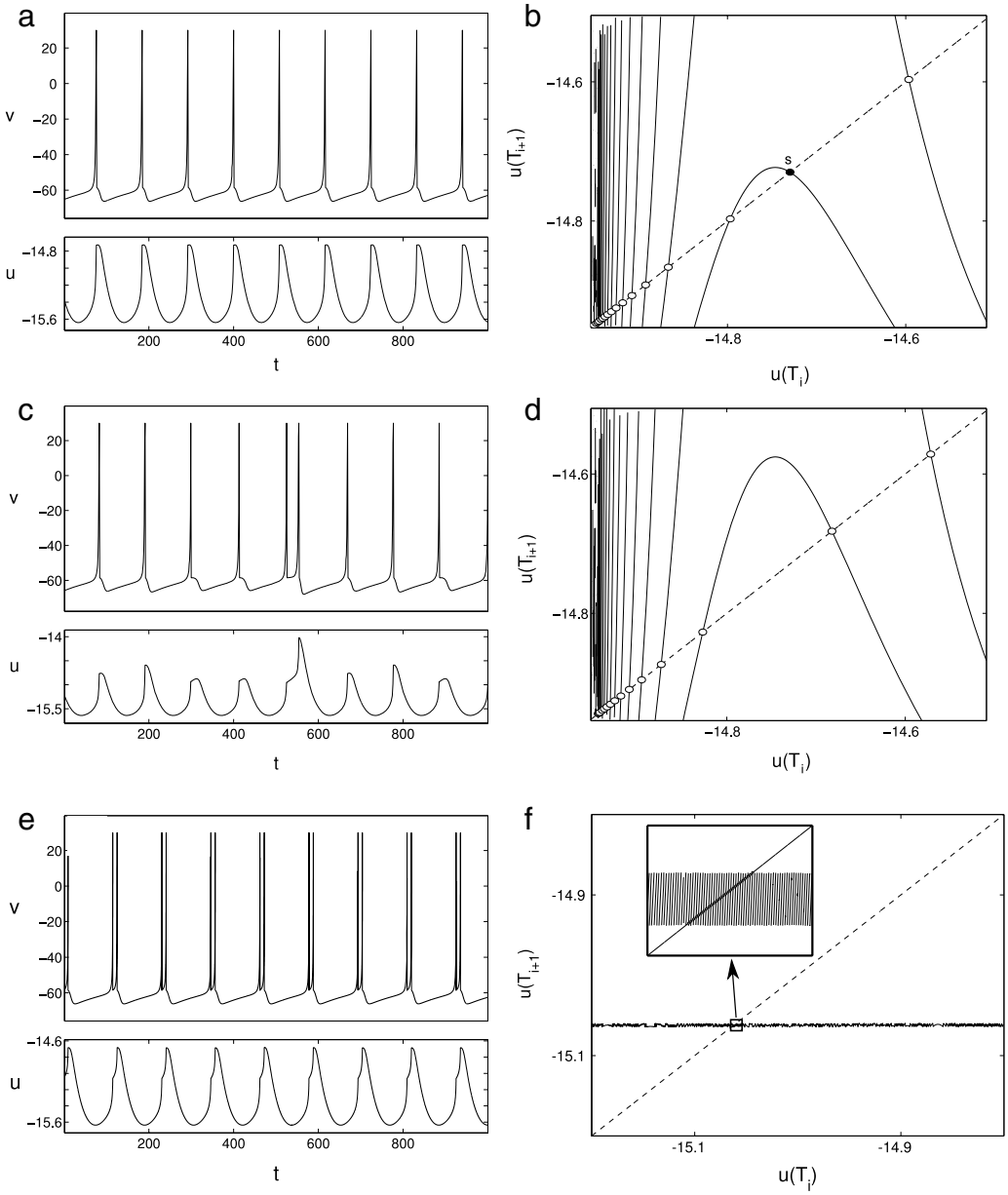

Fig. 36. On the left, orbits of the Izhikevich model, and on the right, the corresponding bursting adaptation maps. (a) and (b), $I = 0.6820$. (c) and (d), $I = 0.6828$. All other parameters are the same as in Fig. 35. In case (a) the orbit is periodic, as corresponds to the stable fixed point s in the adaptation map. The adaptation map in (b) is easily proven chaotic, and so is the corresponding orbit. (e) and (f) are the same as (c) and (d), except the time step has been reduced 100-fold. Each time unit represents 100 iterations. The adaptation map has collapsed into a straight line that proves the system is periodic in a coarse scale; however, the inset in (f) shows that what looks like a line is actually a complicated map, just as in (d).

To determine whether chaos is due to the threshold-and-reset or to the finite integration interval, we can modify the time step and compare. To do this, we first rearrange the v equation in Eq. (7) into the form $v(t+1) = v(t) + \hat{F}[v(t), I \pm u(t)]$, and then change the time scale:

$$v(t + 1/S) = v(t) + \frac{1}{S}\hat{F}[v(t), I \pm u(t)],$$
$$u(t + 1/S) = u(t) \mp \frac{1}{S}\epsilon \cdot [v(t) - qu(t) - \sigma],$$

where $S > 1$ is the scale reduction. Of course, this only makes sense if the map-based model can be meaningfully traced back to a Euler-discretized continuous-time counterpart. Thus, if we use a time step of 0.01 ms, instead of 1 ms ($S = 100$), to discretize the Izhikevich model, the adaptation map in Fig. 35(d) collapses into what looks like a horizontal line [Fig. 35(f)],

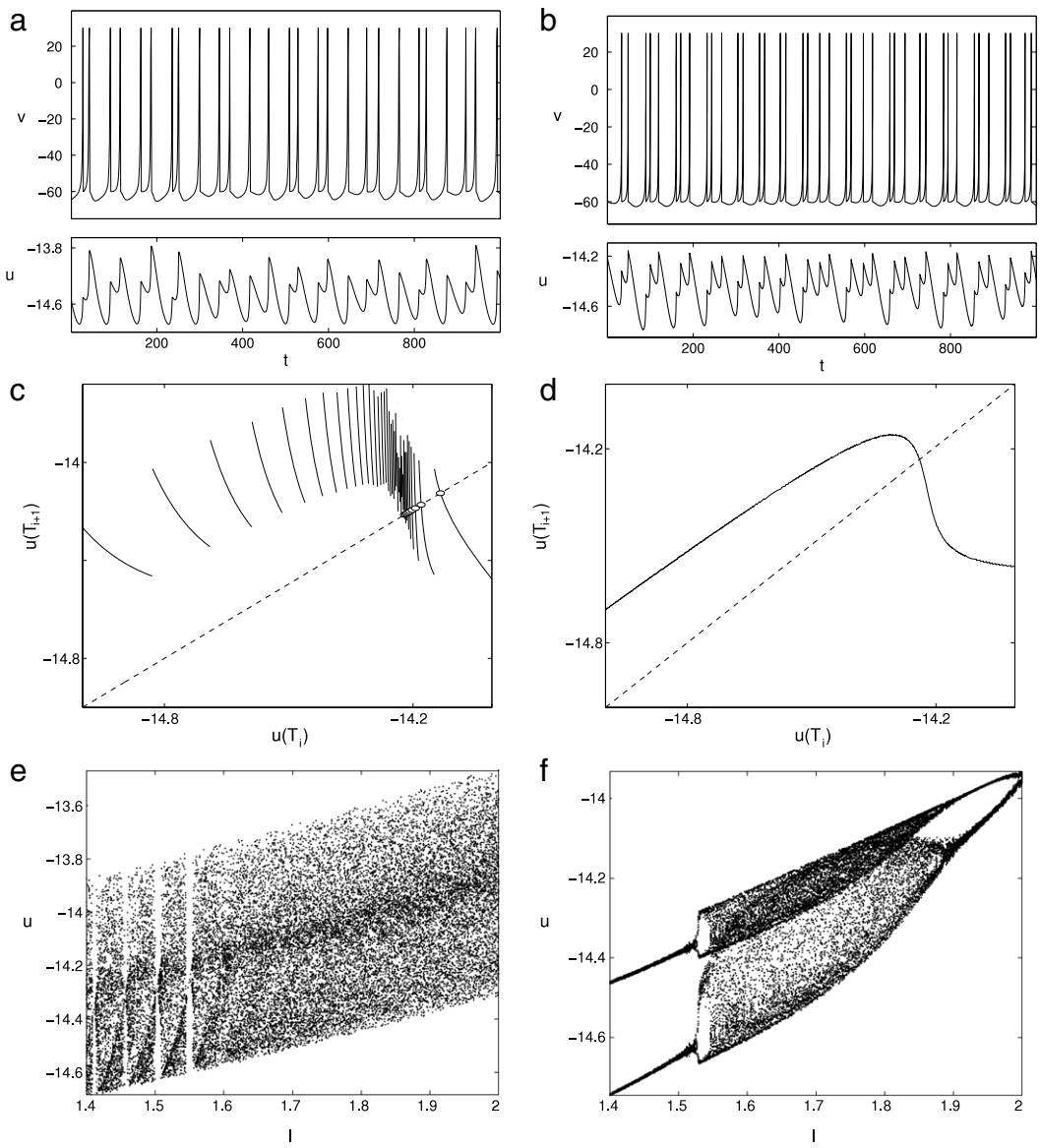

Fig. 37. Figures on the left column come from the usual map-based Izhikevich system of Eqs. (11), with $a = 0.02$, $b = 0.25$, $c = -60$. Figures on the right are from the same model, but integrated with a time step 1/100 smaller. (a) and (b) Chaotic orbits at $I = 1.7$. In (a), t represents time steps, as usual. In (b), each unit of t corresponds to 100 iterations. (c) and (d) Spiking adaptation maps. Notice that the map in (c) looks like a "sliced" version of the map in (d). (e) and (f) Bifurcation diagrams of the adaptation map, as a function of excitation I.

and the orbit regularizes. At a finer scale we see that the map is still chaotic (with the features of a baker's map [34], see the inset of Fig. 35(f)), but clearly the chaoticity is completely an artifact of discretization. A more interesting case is depicted in Fig. 37. Here we see a chaotic spiking orbit that remains chaotic when the time step is reduced 100 times. The adaptation map with the normal time step [Fig. 37(c)] looks like a chopped version of the fine-timescale adaptation map [Fig. 37(d)], each piece stretched due to the pre-spike expansion of the fast subsystem. But as the pieces collapse into the apparently smooth map of Fig. 37(d), the chaotic nature of the map remains. The bifurcation diagram of the adaptation maps [Figs. 37(e) and (f)] as a function of excitation I shows that, while chaos is pervasive in the original map-based model [Fig. 37(e)], the finely discretized version displays a typical cascade of bifurcations [Fig. 37(f)], with wide chaotic parameter regions. We can therefore say that the chaotic orbit in Fig. 37(a) is not a mere artifact of the finite time step: the discretization adds an additional layer of chaos over the already chaotic behavior of the continuous-time model, which is due to the threshold-and-reset jumps.

A different technique to understand the origin of chaotic orbits in map-based neuron models is described by Shilnikov and Rulkov [94], for the particular case of the non-chaotic Rulkov model. It can be summarized as follows: the fast subsystem nullcline, also known as the *critical manifold* [95], is normally hyperbolic at every point except the saddle–node bifurcation.

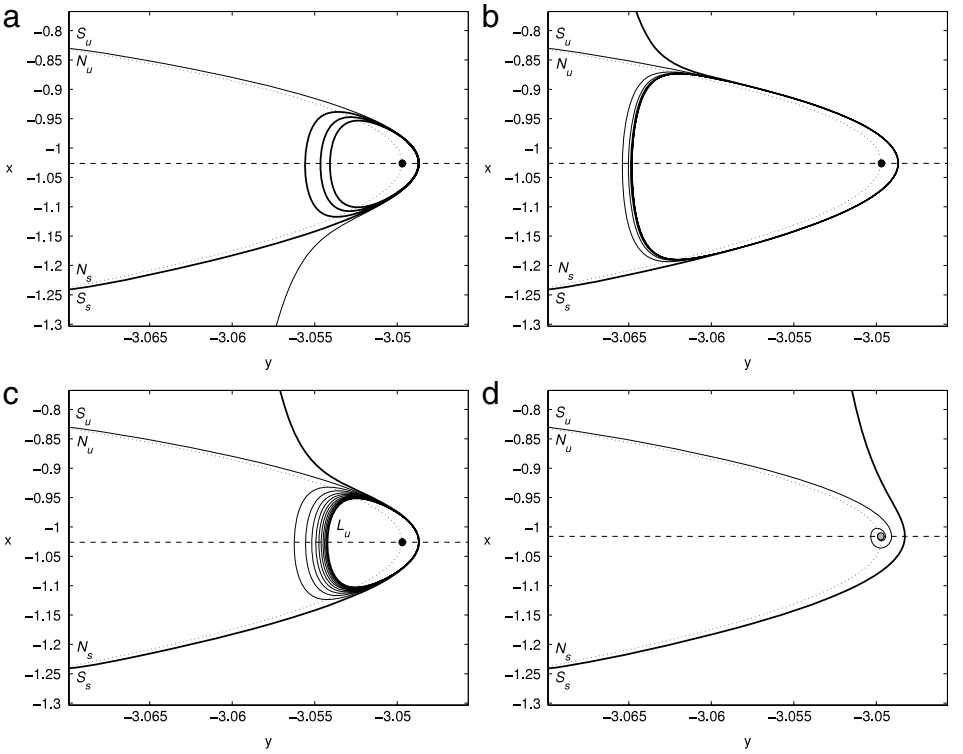

Fig. 38. Evolution of the stable, S_s (thick continuous line), and unstable, S_u (thin continuous line), invariant manifolds μ-close to the stable, N_s, and unstable, N_u, branches of the fast subsystem nullcline (dotted line), of the Rulkov model of Eqs. (13). Parameter values are $\mu = 0.001$ and $\alpha = 4.15$. The dashed horizontal line is the slow subsystem nullcline at $x = \sigma$. A circle marks the fixed point of the system, solid black if stable, light gray if unstable. (a) $\sigma = -1.0262$. The fixed point is stable and globally attracting; the stable invariant manifold S_s slowly spirals into it. (b) $\sigma = -1.02611317$. The fixed point is still stable, but the stable and unstable invariant manifolds have collided (not appreciated in the figure). (c) $\sigma = -1.02605$. The stable and unstable invariant manifolds no longer cross each other (not appreciated in the figure). The unstable manifold S_u approaches a limiting repelling invariant curve, labeled L_u, that separates the basin of attraction of the fixed point from the rest of state space. (d) $\sigma = -1.016$. The fixed point has turned unstable at the Neimark–Sacker bifurcation. The unstable invariant manifold S_u spirals away from it.

This ensures that, when we consider the full two-dimensional system of Eqs. (13), this manifold will persist in the form of two invariant manifolds that are ϵ-close to the stable and unstable branches of the nullcline [96]. The evolution of the stable manifold as parameters change can be traced by iterating the map forwards from initial conditions on the stable branch of the nullcline, far from the saddle–node. Iterates quickly converge on the stable invariant manifold. The same can be done for the unstable invariant manifold by locally inverting the two-dimensional map of Eqs. (13); inversion yields

$$\begin{aligned} x(t) &= Z, \\ y(t) &= y(t+1) + \mu(Z - \sigma), \end{aligned} \tag{31}$$

where

$$\begin{aligned} Z &= k - \sqrt{k^2 - 2k + 1 + \alpha/\mu}, \\ k &= \frac{x(t+1) - y(t+1) + \mu(\sigma + 1)}{2\mu}. \end{aligned} \tag{32}$$

The unstable invariant manifold of the original map is stable and attracting in the inverted map, and can be traced similarly.

Fig. 38 depicts the changes in the stable and unstable invariant manifolds in the Rulkov model as the excitation parameter σ changes through the subcritical Neimark–Sacker bifurcation. The reader may also find Fig. 32(a), where the diagram of the same bifurcation in the Izhikevich model is depicted, helpful for the present discussion. In Fig. 38(a) the fixed point of the map is stable and globally attracting. The system is not far from the Neimark–Sacker bifurcation, and, for this reason, the stable invariant manifold S_s climbs up close to the unstable branch of the fast nullcline, spiraling into the fixed point very slowly. Although the unstable invariant manifold S_s acts as a boundary separating the immediate basin of attraction of the fixed point from the rest of the state plane, orbits starting outside the immediate basin will end up in it by way of the spike reset mechanism. In Fig. 38(b), the excitation parameter σ has increased slightly and the stable and unstable invariant manifolds have collided; a magnification of the region close to the vertex of the fast subsystem nullcline would show the intertwining of both manifolds. Such crossings could never happen in the corresponding continuous-time two-dimensional system. In continuous time, as the system gets close to the situation depicted in Fig. 38(b), trajectories follow

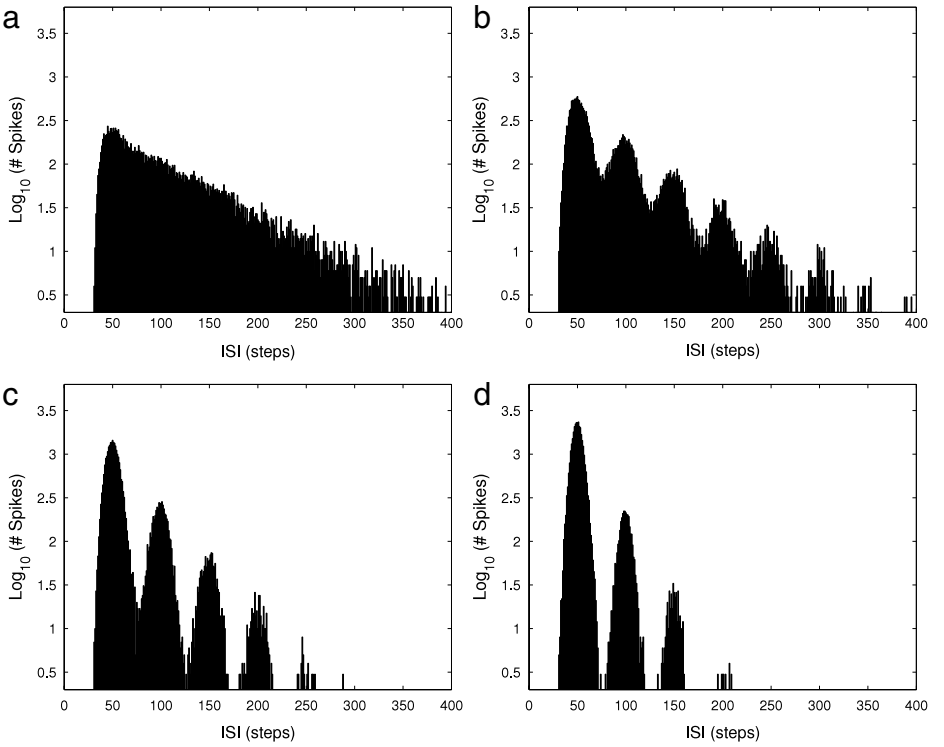

Fig. 39. Interspike interval histogram for the Chialvo model driven by white noise and a sinusoidal subthreshold input. Parameter values for Eqs. (21) are $a = 0.89$, $b = 0.6$, $c = 0.28$, $I = 0.01$. White noise is added to the x equation; it is uniformly distributed between -0.06 and 0.06 (standard deviation is therefore $\sigma = 0.035$). The sinusoidal modulatory signal also enters additively in the x equation, and its amplitude is (a) $A = 0$, (b) $A = 0.01$, (c) $A = 0.02$, and (d) $A = 0.03$. Spikes are counted whenever x crosses the value $x_{thr} = 2.5$. According to Chialvo and Apkarian [102].

the unstable branch of the fast nullcline for ever longer stretches before falling onto the equilibrium point, until, at the saddle–node of limit cycles bifurcation [the continuous-time equivalent of the saddle–node of invariant curves bifurcation depicted in Fig. 32(a) at I_{snic}], an unstable limit cycle appears and trajectories shoot up instead of falling down. The limit cycles that closely follow the unstable branch of the fast nullcline are called *canards* [97]. Canards are hard to obtain by numerical integration due to the explosive behavior of the system in the vicinity of the unstable branch of the nullcline [95]. This is precisely the situation depicted in Fig. 38(b), where close initial conditions near the stable manifold are blown up and separated by the unstable manifold, get mixed again by the reset mechanism, and result in chaotic orbits.

A further increase in σ leads to the phase portrait of Fig. 38(c), where the stable and unstable invariant manifolds are no longer intermingled. The invariant manifold closes in on a closed unstable invariant curve L_u separating the basin of attraction of the stable fixed point from that of periodic spiking orbits. Finally, at a slightly higher value of excitation, the Neimark–Sacker bifurcation takes place as L_u shrinks onto the fixed point. Its basin of attraction vanishes, and only spiking orbits are possible.

The above discussion outlines the origin of chaos at the transition from the quiescent to the spiking regime, near the Neimark–Sacker bifurcation. A discussion of chaotic orbits at the transition between spiking and bursting can also be found in [94]; for a similar discussion around the supercritical Rulkov model, see [52].

3.4. Stochastic coherence and stochastic resonance

A considerable amount of background noise is present in the signals that neurons in the central nervous system need to process [98]. Sources of noise include ion channels and pumps [99] and neurotransmitter release [100], but also synaptic bombardment by thousands of presynaptic neurons, some of which convey useful information, while others only contribute accidentally to the fluctuations in the membrane voltage of postsynaptic neighbors. Separating the purposeful sources of variability from the noisy ones is a very difficult problem [101]. One necessary step to disentangle it is to understand the response of neuron models to noisy inputs.

An early work of Chialvo [102] illustrates the basic response of two-dimensional map-based neurons to noisy inputs. When white noise is injected into a quiescent neuron, it fires at random intervals. The intervals depend on how far the quiescent level is below the firing threshold and the amplitude of the noise. The resulting interspike interval (ISI) distribution is similar to that of a Poisson process with a refractory period: ISI frequencies decay exponentially as the interval increases [Fig. 39(a)]. If a subthreshold periodic current is injected, firing becomes more likely at the times when the injected current

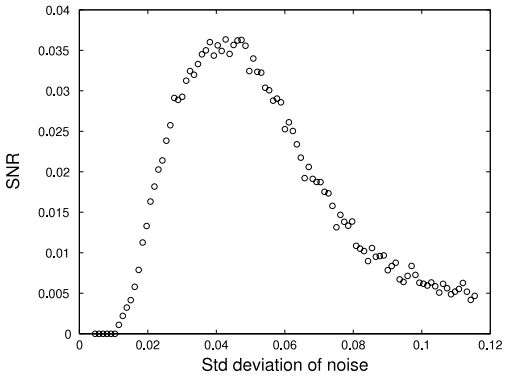

Fig. 40. Signal-to-noise ratio (SNR) of the output of the Chialvo model with a sinusoidal subthreshold input signal, for different levels of white noise. All parameters are the same as in Fig. 39, with sinusoidal input amplitude fixed at $A = 0.015$. SNR is measured as the quotient between the number of pairs of consecutive spikes with interspike interval equal to the period of the sinusoidal input ($T = 50$) and the total number of spikes.

most depolarizes the membrane voltage. Therefore, interspike intervals tend to cluster around integer multiples of the period of the driving signal. This effect is shown in Fig. 39(b)–(d). As the amplitude of the periodic current increases, keeping noise amplitude constant, a multi-peak ISI histogram emerges with an exponentially decaying envelope. This behavior is found in experimental histograms recorded from real, periodically forced sensory neurons, and proves the importance of noise for the transmission of sensory information [103].

Indeed, noise can be helpful in preserving features of the input signal at the output of the neuron. If, instead of keeping noise amplitude constant and intensifying the periodic signal, we keep the latter constant and vary the former, and measure the signal-to-noise ratio (SNR) of the output, it turns out that SNR is maximized at a finite noise level. This is shown in Fig. 40, where SNR is measured as the ratio of interspike intervals that exactly coincide with the driving signal period. This enhancement of information transmission by means of an optimal noise level is known as *stochastic resonance* (SR) [104], and is also a universal feature of excitable systems. Stochastic resonance is a rather counterintuitive phenomenon in which the response of a nonlinear dynamical system to an external force is enhanced by a finite level of noise. Thus, SR is revealed by the non-monotonic behavior of some quantifiers – mostly the signal-to-noise ratio – with the noise strength. Longtin et al. [103] suggested that SR could be of importance in neurobiology as it provides a constructive role to noise in the process of transduction/coding of information by sensory neurons. They argued that, in a well-defined sense, the response of a stimulated neuron could be described by the dynamics of a particle in a bistable potential subjected to both forcing and noise, reproducing the experimental behavior of certain neurons of the sensory system. Here we see how the SR phenomenology arises as well in map-based models of excitable systems.

White noise and sinusoidal inputs are basic building blocks in signal processing theory. However, in the context of spiking neurons, pulsed inputs may be deemed more meaningful, and Poissonian trains of pulses may play a role equivalent to that of white noise in assessing their characteristic response. A very simple measure to quantify this response is the *coefficient of variation*, C_V [3]. The C_V is a measure of the irregularity of a train of spikes. It is defined as the ratio between the standard deviation of interspike intervals and their average value:

$$C_V = \frac{\sqrt{var(T)}}{\langle T \rangle}.$$

For a Poissonian spike train, where spikes are independent of each other, $C_V = 1$, whereas for a periodic spike train, $C_V = 0$.

Interesting information about a neuron can be gained by feeding it with a Poissonian train of pulses and measuring the C_V of its output train of spikes. When this is done with the map-based Izhikevich model of Eqs. (11) for different values of the slope of its slow nullcline, for example, the results depicted in Fig. 41 are obtained. It can be observed that the coefficient of variation is less than unity, which is the C_V of the stimulation. Therefore, the neuron regularizes the input stimulus. This is to be expected simply as a result of refractoriness [2]. The interesting point is that the degree of regularization decreases (C_V increases) with increasing $1/b$. This is due to the loss of resonance described in Section 3.2. Further details are provided by Ibarz et al. [51].

A complete understanding of the response of map-based neuron models to stochastic inputs requires quantitative predictions of the relationship between neuron parameters and noise features. This quantitative treatment can be carried out by standard methods of stochastic analysis. Since the dynamics of spike generation is threshold-like, it can be treated as a first-exit-time problem amenable to Fokker–Planck formulation [105]. This has been done, for example, for the chaotic Rulkov model in its spiking regime [106–108]. Noise is injected either in the fast or the slow variable, or both:

$$\begin{aligned} x(n+1) &= \frac{\alpha}{1+x^{(n)}} + y(n) + \sqrt{D_x}\xi_x(n), \\ y(n+1) &= y(n) - \mu[x(n) - \sigma] + \sqrt{D_y}\xi_y(n). \end{aligned} \tag{33}$$

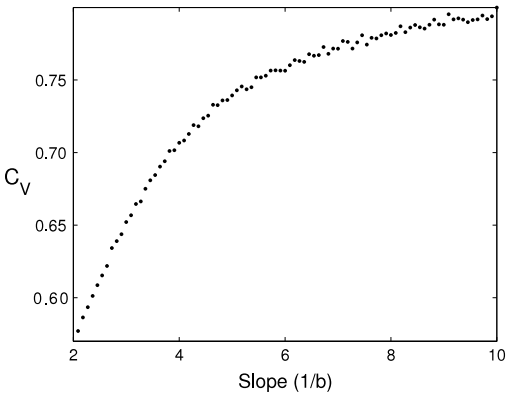

Fig. 41. Coefficient of variation C_V for different values of the slope $1/b$ of the slow subsystem nullcline of the Izhikevich model of Eqs. (11), stimulated by a Poissonian train of pulses and Gaussian white noise. Each point corresponds to the average of 100 realizations of noise. The neuron is kept excitable for all values of b by injection of a stationary current $I(b)$ such that the resting voltage of the system is stable at $v^* = -62.7$. Other parameters are $a = 0.02$ and $c = -62.5$.
Source: From Ibarz et al. [51].

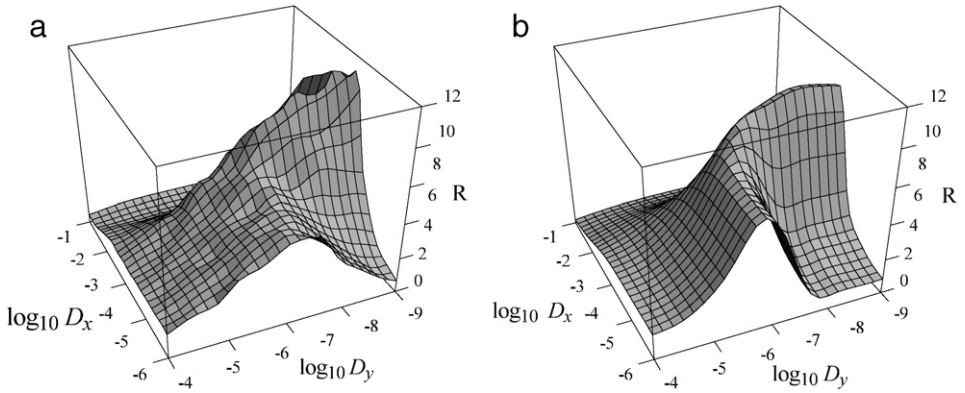

Fig. 42. Regularity R as a function of noise variances D_x and D_y in the Rulkov model of Eqs. (33), with $\alpha = 1.99$, $\mu = 0.001$ and $\sigma = -1$. With these parameter values the neuron is excitable and produces random spikes (not bursts). (a) Simulation results. Each point of the surface represents an average over ten independent noise realizations of $5 \cdot 10^5$ iterations of the model. (b) Values predicted by a Fokker–Planck approximation.
Source: From Hilborn and Erwin [108].

In the above equations, ξ_x and ξ_y are Gaussian white noise independent processes of unit standard deviation, D_x and D_y representing their variance. As with the Chialvo model, if a periodic input signal is added to the noise, the system exhibits stochastic resonance. Hilborn and Erwin [108] quantitatively studied a closely related phenomenon, *stochastic coherence*. In this case, no periodic input signal is present; only noise. The output train of spikes is then irregular, and its degree of randomness is lowest at finite values of noise amplitude. As before, the randomness of this output can be quantified by means of the coefficient of variation, or, alternatively, by means of its reciprocal, called *regularity*, R, defined as

$$R = \frac{1}{C_V} = \frac{\langle T \rangle}{\sqrt{var(T)}}. \tag{34}$$

The higher R, the closer to periodic is the output train of spikes. Fig. 42(a) represents R as a function of both D_x and D_y in the chaotic Rulkov model; these values have been obtained from simulations. It is apparent that for fixed values of D_y, regularity is maximal at nonzero values of D_x, and the same is true for fixed D_x when varying D_y, at least for low D_x.

These simulation results can be predicted by a Fokker–Planck analysis. The way to do this is to divide the behavior of the excitable Rulkov neuron into three phases: an activation phase, where the neuron lies close to the stable fixed point; a pulse phase, when noise pushes the state beyond threshold and a spike is generated; and a recovery phase, where the state slowly relaxes back to the activation region. Corresponding to each phase, a first-exit time problem for the mean and variance of the time spent in it is solved. Regularity can then be estimated as

$$R = \frac{\langle T_a \rangle + \langle T_p \rangle + \langle T_r \rangle}{\sqrt{var(T_a) + var(T_p) + var(T_r)}},$$

where T_a, T_p and T_r are first-exit times for the activation, pulse and recovery phase. The details of the calculation can be found in [108]. In Fig. 42(b) calculated values of R as a function of D_x and D_y are depicted for comparison with the simulation

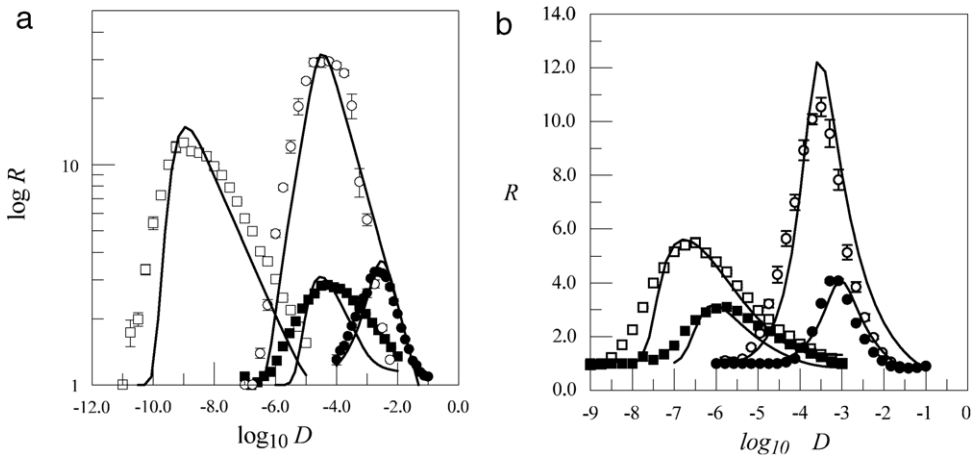

Fig. 43. (a) Analytically predicted (continuous lines) and simulated (dotted lines) regularity R of spike trains of the Rulkov model of Eqs. (33) as a function of noise variance D. Squares correspond to $D = D_y$, with $D_x = 0$, while circles correspond to $D = D_x$, with $D_y = 0$. Open symbols are for $\mu = 10^{-4}$ while solid symbols are for $\mu = 10^{-2}$. In all cases $\alpha = 1.99$. (b) The same with $\mu = 10^{-3}$ and $\alpha = 1.99$ (open symbols) or $\alpha = 1.91$ (solid symbols).
Source: From Hilborn and Erwin [108].

values of Fig. 42(a). The Fokker–Planck approximation yields a good fit to the simulations at a fraction of the computational cost. Another comparison of analytical and simulation results is shown in Fig. 43. Predictions are not perfectly accurate, especially for the lowest levels of noise, but they do pin down the important relationships between parameters and behavior. For example, for smaller values of μ the time scales of the model are more separated and whether noise is added to the fast or the slow variable makes a more important difference [Fig. 43(a)]. On the other hand, decreasing α from 1.99 to 1.91 moves the stable fixed point further from the saddle–node bifurcation of the fast subsystem, thereby increasing the barrier the system must overcome in order to spike. Hence, the noise variance must be larger to achieve a given level of activation, and the maximum of regularity is achieved at higher noise levels [Fig. 43(a)].

4. Network behavior of map-based neuron models

As individual neurons connect to form networks, collective dynamic phenomena emerge whose mechanisms and functional significance are usually very hard to elucidate. The properties of each neuron, the scheme of connection between them, and the topology of the network, interact in complex ways to shape the dynamics of the full, high-dimensional system, and disentangling the influence of the different factors is a major challenge for computational neuroscience. In this section we review studies on collective modes of behavior, such as synchronization or propagation of activity, found in networks of map-based neurons.

4.1. Synchronization of spiking map-based neurons

Synchronous behavior of neural assemblies is a central topic in neuroscience. It is known to be correlated with cognitive activities [109] during the normal functioning of the brain, while abnormal synchronization is linked to important brain disorders, such as epilepsy, Parkinson's disease, Alzheimer's disease, schizophrenia and autism [110]. Hence the interest in the topic of neural synchronization, which has been extensively explored theoretically [111]. A sizable amount of work has been devoted to the case of map-based models.

Synchronization of map-based neuron models is sometimes studied in the context of coupled map lattices (CML) [10,11]. The theory of coupled map lattices deals with the dynamics of extended systems made up of chaotic maps, referred to as nodes, linked to each other to form a regular structure, such as a ring or a mesh. Typically, coupling takes on the following form:

$$\mathbf{x}_i(n+1) = (1-\epsilon) f\left[\mathbf{x}_i(n)\right] + \frac{\epsilon}{|\mathcal{N}_i|} \sum_{j \in \mathcal{N}_i} f\left[\mathbf{x}_j(n)\right], \tag{35}$$

where $\mathbf{x}_i(n)$ is the state vector of the i-th node at time step n, with i running from 1 to N, the total number of nodes. $\mathcal{N}_i$ is the set of neighbors of node i, and ϵ represents the strength of coupling ($0 \leq \epsilon \leq 1$). In the typical regular lattices, all neighborhoods have the same cardinality, sometimes called coordination number. With the coupling in Eq. (35), the nodes lose their individuality, since their next iterate is calculated as a mixture of iterates of several nodes. This is convenient for analytical purposes, and ensures that, when the system achieves complete synchronization, each node will behave as isolated, and the dynamics will be independent of the coupling strength. However, in a biological context, when nodes represent neurons, this form of coupling is seldom used.

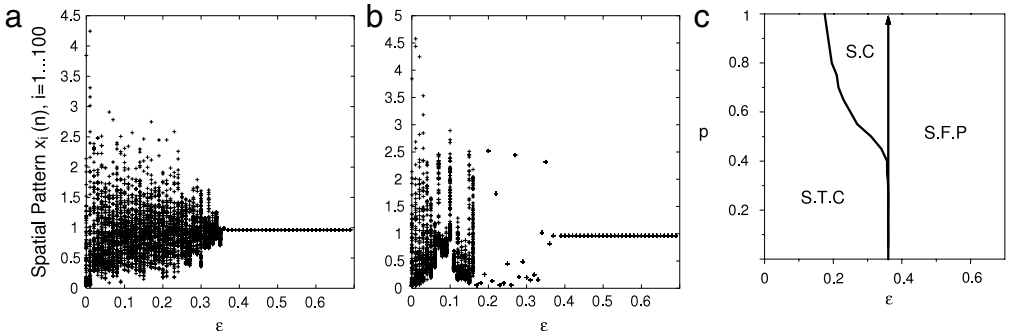

Fig. 44. (a) and (b) Snapshots of the network defined by Eqs. (36) as a function of coupling strength ϵ. In (a), the network is a regular ring ($p = 0$), while in (b), it is completely random ($p = 1$). In the latter case there is an interval of ϵ (approximately, $0.16 < \epsilon < 0.36$) where the network is synchronized, not at a fixed point, but in a chaotic orbit. (c) Regimes of synchronization in the network, in the ϵ–p space. The abbreviations SC, STC and SFP denote synchronized chaos, spatio-temporal chaos and synchronization at fixed point.
Source: From Jampa et al. [112].

Jampa et al. [112] used a modification of the CML coupling scheme. In this study, the nodes are Chialvo neurons. Eqs. (21) are coupled to yield the system

$$\begin{aligned} x_i(n+1) &= (1-\epsilon)\left[x_i(n)^2 e^{y_i(n)-x_i(n)} + I\right] + \frac{\epsilon}{2}\left[x_{\xi_i(n)}(n) + x_{\eta_i(n)}(n)\right], \\ y_i(n+1) &= a y_i(n) - b x_i(n) + c. \end{aligned} \tag{36}$$

In contrast with Eq. (35), the neurons are coupled only through their first variable (voltage), in a manner that closely resembles resistive connections. Each neuron i has two neighbors, indicated by subscripts $\xi_i(n)$ and $\eta_i(n)$. At each time step, with probability $1-p$, $\xi_i(n) = i-1$ and $\eta_i(n) = i+1$ (modulo N), while with probability p those indices are selected at random in the range $1 \ldots N$. In other words, the network is a ring whose links are randomly rewired with probability p *at each time step*. This dynamic rewiring assimilates the coupling to an all-to-all mean-field scenario (see Section 4.2). The neuronal parameters used are $a = 0.89$, $b = 0.18$, $c = 0.28$ and $I = 0.03$; with these, isolated neuron dynamics are chaotic.

Synchronization is affected both by the coupling strength ϵ and the probability of rewiring p. The dependence is summarized in Fig. 44(c), while the snapshots represented in Fig. 44(a) and (b) help visualize the difference between the case $p = 0$ and the case $p = 1$. When coupling is strong ($\epsilon > \epsilon_c \approx 0.361$) the unique fixed point of the system becomes a stable global attractor, and all neurons remain quiescent at that point; this is independent of the rewiring probability. But at lower levels of coupling the global activity depends on p: for low p (mostly fixed links), the network is not synchronized, each neuron chaotically firing independently of the others (a state that the authors label as spatio-temporal chaos); but at higher values of p there is an interval of coupling strengths below ϵ_c that result in complete synchronization, not at a fixed point but in a chaotic spiking regime.

The fact that the synchronization interval grows monotonically with p might seem to suggest that a completely random topology is better from the point of view of synchronization than a regular structure or an intermediate, small-world scenario [113]. However, such a conclusion is unwarranted because of the dynamic nature of the links in the model of Eqs. (36). In fact, averaged over a large number of iterations, random links act as a form of diluted global, or all-to-all, coupling, and linear analysis based on this identification yields good agreement with numerical simulations. The globally coupled system equivalent to (36) is

$$\begin{aligned} x_i(n+1) &= (1-\epsilon)\left[x_i(n)^2 e^{y_i(n)-x_i(n)} + I\right] + (1-p)\frac{\epsilon}{2}\left[x_{i+1}(n) + x_{i-1}(n)\right] + \frac{\epsilon p}{N}\sum_{j=1}^{N} x_j(n), \\ y_i(n+1) &= a y_i(n) - b x_i(n) + c. \end{aligned} \tag{37}$$

Notice that, in Eqs. (37), links are no longer dynamic. The Jacobian of the system around a synchronized state is a block circulant matrix,

$$J = \begin{pmatrix} A+C & B+C & C & C & \ldots & C & B+C \\ B+C & A+C & B+C & C & \ldots & C & C \\ \vdots & \vdots & \vdots & \vdots & \ddots & \vdots & \vdots \\ B+C & C & C & C & \ldots & B+C & A+C \end{pmatrix},$$

where block A is due to intrinsic dynamics and depends on the state, B is due to nearest neighbor coupling and is proportional to $1-p$, and C is due to global coupling and proportional to p. Increasing p strengthens the C blocks and weakens the B blocks, and this shifts the matrix eigenvalues towards the stable half-plane. Therefore, what this study seems to imply is that global, and not random, coupling is better for synchronization than local coupling. Another study whose implications for the

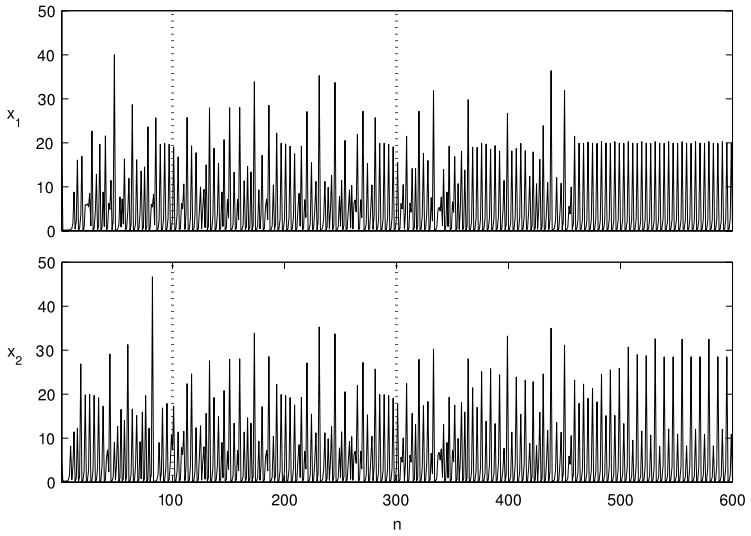

Fig. 45. Synchronization of two Chialvo neurons coupled according to Eqs. (38), with chaos suppression by means of periodic pulses, Eqs. (39). Before the first dashed vertical line, the neurons run independently from different initial conditions. The coupling is active after the first dashed vertical line, and the periodic pulses after the second one. The parameters of both neurons are $a = 1.04$, $b = 0.1$, $c = 0.45$ and $I = 0.147$. The periodic pulses have $\lambda_x = \lambda_y = -0.035$ and $p = 12$. According to Güémez and Matías [120].

topic of the dependence of synchronization among map-based neurons on the degree of randomness of their connections are dubious is [114], where connections between Rulkov neurons are not rewired, but rather added at random, and therefore it is unclear whether the reported increase in synchrony is due to randomness or merely to the number of links. Simulations in [115] show that synchronization of chaotic Rulkov neurons is rather insensitive to rewiring; in this work, the emphasis is on connection delays (see also [116]). A numerical study of the effects of probability of rewiring in community-structured networks [117] of Izhikevich neurons can be found in [118]. Here again synchronization is shown to grow monotonically with rewiring probability, although the stress is on another property, *causal density* [119], which peaks at low p values.

A different coupling scheme that is advantageous from the point of view of analysis but has no physiological counterpart is used by Güémez and Matías [120], who also study synchronization among two or more coupled chaotic Chialvo neurons, although in the context of chaos suppression. Coupling is implemented by shared variables, as in the following example:

$$\begin{aligned} x_1(n+1) &= x_1(n)^2 e^{y_1(n)-x_1(n)} + I, \\ y_1(n+1) &= a y_1(n) - b x_1(n) + c, \\ x_2(n+1) &= x_1(n)^2 e^{y_2(n)-x_1(n)} + I, \\ y_2(n+1) &= a y_2(n) - b x_2(n) + c. \end{aligned} \tag{38}$$

Notice that in Eqs. (38), the x variable of the *first* neuron is used to define the dynamics of the x variable of the *second* neuron; it can be said that the first neuron drives the second one. This form of coupling has received much attention in studies of synchronization of chaotic systems [121]. It does result in synchronized chaotic orbits when applied to Chialvo neurons, as shown in Fig. 45. Additionally, a mechanism of chaos suppression is implemented by means of multiplicative periodic pulses applied to the driving neuron, as follows:

$$\begin{aligned} x_1(n+1) &= \left[x_1(n)^2 e^{y_1(n)-x_1(n)} + I\right](1 + \lambda_x \delta_{m,p}), \\ y_1(n+1) &= \left[a y_1(n) - b x_1(n) + c\right](1 + \lambda_y \delta_{m,p}), \end{aligned} \tag{39}$$

where $\delta_{m,p}$ is Kronecker's delta and $m \equiv n \pmod p$, p being the period of the pulses. Constants λ_x and λ_y scale the pulses for each variable. The pulses achieve the stabilization of a periodic orbit. Interesting as these facts may be from the point of view of nonlinear dynamics, and although chaotic synchronization and chaos control may be of some relevance to the issue of information processing in the brain, the scheme of coupling and forcing seems too far from physiological plausibility, and it has not been pursued further with map-based neuron models.

A more interesting form of coupling, from a biological point of view, is *pulse* coupling. Synchronization in all-to-all pulse-coupled networks of identical excitatory LIF neurons is known to be a globally attracting state [122]. Likewise, Nagumo–Sato neurons tend to completely synchronize when they are globally pulse-coupled [123]. The equations of a network of Nagumo–Sato pulse-coupled neurons with identical parameters are

$$y_i(n+1) = k y_i(n) + a - H[y_i(n)] + \epsilon \sum_{j \neq i} \sum_k \delta(n - n_{j,k}), \tag{40}$$

where $n_{j,k}$ is the time step where neuron j produces its k-th spike, that is, for all k, $y_j(n_{j,k}) \geq 0$. In other words, every time a neuron fires it advances the voltage of all other neurons by ϵ. In the case of the LIF model, the arrival of a pulse at two

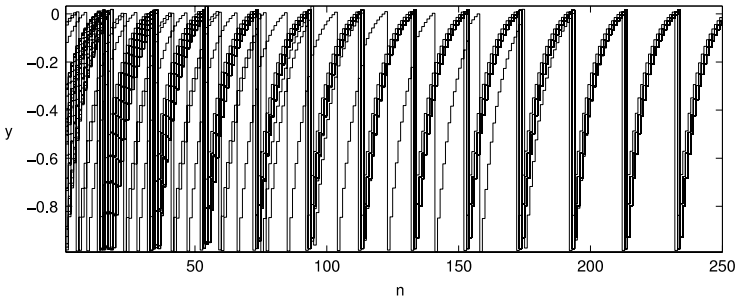

Fig. 46. Behavior of 30 Nagumo–Sato neurons in the all-to-all pulse-coupled network defined by Eq. (40). The orbits of the 30 neurons are simultaneously depicted. Neurons are gradually absorbed in a small number (three, in the present example) of completely synchronized clusters. Parameters are $k = 0.87$, $a = 0.01$ and $\epsilon = 0.002$.

neurons close to threshold makes them fire together and be reset at exactly the same level; from then on, they will always be perfectly synchronized. This is called synchronization by absorption. In the Nagumo–Sato model there is no absorption, because there is no fixed reset level. Nevertheless, as exemplified in Fig. 46, the neurons do tend to group together under global pulse coupling in a small number of completely synchronized clusters. Different clusters maintain a constant phase lag between them. Masuda and Aihara [123] explained this phenomenon by means of a phase description, following the example of [122]. The phase variable ϕ is defined as

$$\phi(y) = \frac{\ln \frac{a}{a-(1-k)y}}{\ln \frac{k(a-1)+1}{a}} + 1,$$

so that $\phi(a-1) = 0$, $\phi(0) = 1$, and increments of ϕ are uniform along the subthreshold evolution of the isolated Nagumo–Sato neuron. By studying the expansion and contraction of the phase at the moment of firing and at the reception of incoming spikes, heuristic arguments are furnished to explain the formation of synchronized clusters. Phase descriptions are as fruitful for map-based models as they have proven to be for ODE-based oscillators.

When a small amount of noise is added to Eq. (40), synchronization can be enhanced by disrupting the basins of attraction of solutions whose clusters are highly out of phase. To quantify this effect, the following measure of synchronization error is defined:

$$\chi(n) = \frac{2}{N(N-1)} \sum_{i=1}^{N} \sum_{j=i+1}^{N} d[y_i(n), y_j(n)], \tag{41}$$

where $d(y, y') = \min(|y - y'|, |y - y' + 1|, |y - y' - 1|)$. Without noise the network sets in a clustered solution, and out-of-phase clusters produce a high synchronization error, as seen in Fig. 47(a). But a small amount of noise makes out-of-phase clusters highly unstable, and the network settles around a completely synchronized solution, with small synchronization error, as in Fig. 47(b). Obviously, excessive noise does not help synchronization further [Fig. 47(c)]. These effects are another form of the stochastic coherence phenomenon described in Section 3.4. A brief numerical investigation of stochastic coherence and stochastic resonance in a lattice of chaotic Rulkov neurons is described by Wang et al. [124].

Typically, studies on synchronization employ identical neurons as network nodes, because diversity is hard to deal with analytically. Simulations usually demonstrate that any spread in neuron parameters is damaging for synchronization. However, there are cases where limited diversity may enhance it. One such example is provided by Chen et al. [125]. Non-chaotic spiking Rulkov neurons [Eqs. (13) and (14)] are connected through ohmic links by making the current parameter I vary with time:

$$I_i(n) = \frac{g_e}{|\mathcal{N}_i|} \sum_{j \in \mathcal{N}_i} \left[x_i(n) - x_j(n) \right], \tag{42}$$

where, as in Eq. (35), $\mathcal{N}_i$ is the set of neurons connected to neuron i, and g_e is the conductance of the connections. Both global coupling (where $\mathcal{N}_i$ includes all neurons) and a ring network ($\mathcal{N}_i = i - 1, i + 1$) are tested, with similar results. Neuron parameters are chosen in the spiking regime ($\alpha = 3.0$, $\mu = 0.001$), and diversity is introduced through the excitation parameter σ, which is random and independently picked out for each neuron from a Gaussian distribution with standard deviation D. The degree of synchronization in the network is measured by means of the regularity R defined in Eq. (34). Fig. 48(a) illustrates the phenomenon of diversity-induced resonance. The average value of excitation, σ_0, has been chosen below the spiking threshold defined by the Neimark–Sacker bifurcation [Eq. (15)]; therefore, when diversity is zero, all neurons are quiescent, no spikes are produced, and regularity has no meaning (it is set to zero for continuity). At low values of diversity a few neurons are stimulated above threshold and begin to fire; regularity is low, but as diversity is increased

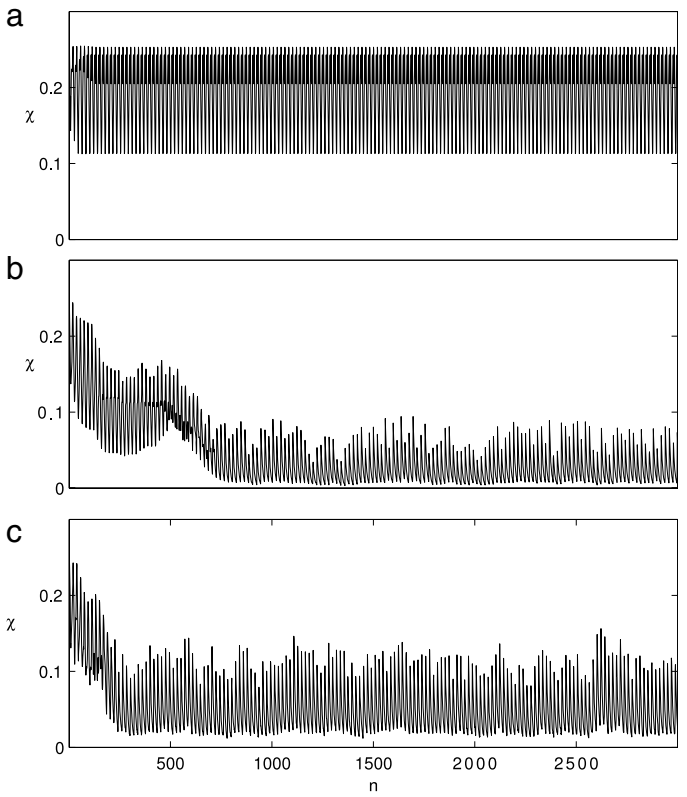

Fig. 47. Synchronization error χ along time in the same network of Fig. 46 with additional white uniform noise of amplitude σ. In (a), $\sigma = 0$: without noise, the network sticks at a clustered solution and the network is far from complete synchronization. In (b), $\sigma = 0.005$: the noise kicks the system away from out-of-phase clustered orbits and into the basin of the completely synchronized solution. In (c), $\sigma = 0.02$: excessive noise damages synchronization.

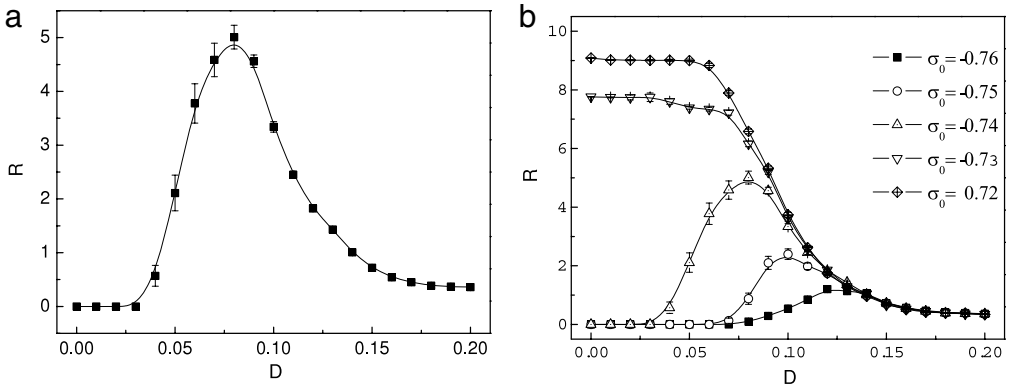

Fig. 48. (a) Regularity R as a function of diversity D in an all-to-all network of 500 electrically coupled non-chaotic Rulkov neurons, Eqs. (13), (14) and (42). Parameters are $\alpha = 3$, $\mu = 0.001$, $g_e = 1$ and σ following a Gaussian distribution with mean $\sigma_0 = -0.74$ and standard deviation D. Regularity is maximized at a finite diversity value. (b) Same as in (a) for varying average excitation σ_0. Only when σ_0 is below the threshold of spiking ($\sigma_{th} \approx -0.733$) can diversity-induced resonance be observed.
Source: From Chen et al. [125].

and more neurons are available for spiking they induce quiescent neurons to fire together with them, and regularity grows. The trend is offset, at high values of diversity, by the spread in the natural spiking frequency of the different neurons.

Therefore, diversity-induced resonance is not a universal phenomenon; it relies on the particular configuration in which most neurons are below threshold and the few that are able to spike dominate the whole network dynamics. This is demonstrated in Fig. 48(b), where resonance curves for different values of average excitation σ_0 are given. When σ_0 is above the spiking threshold, so that all neurons are active at $D = 0$, regularity monotonically decreases with diversity, as intuitively expected. On the other hand, when the average excitation is significantly below threshold, the resonance effect is present, but damped.

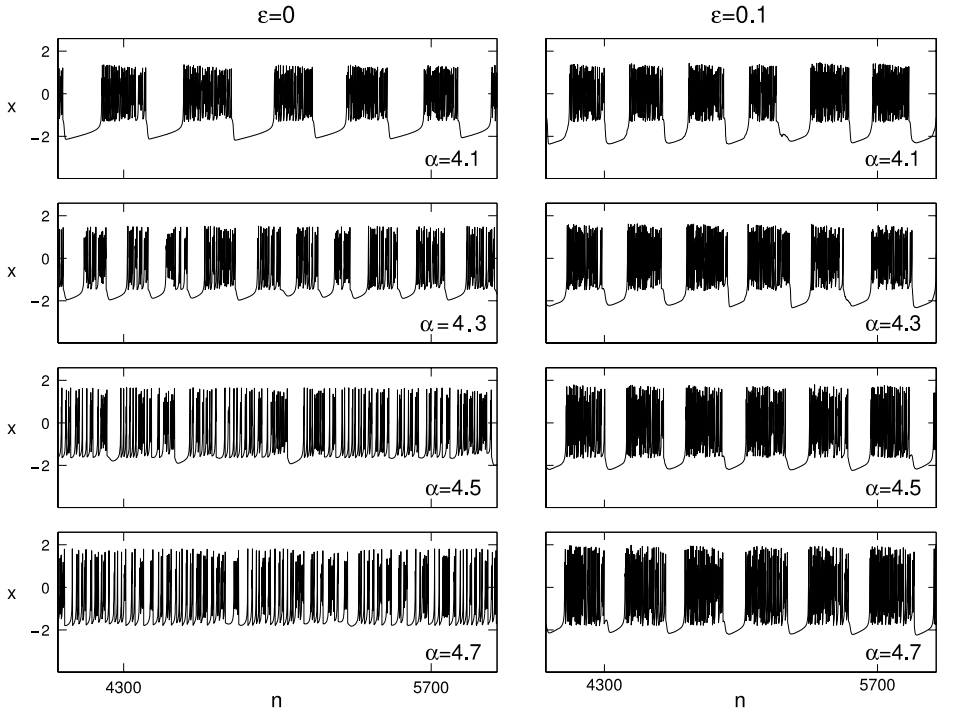

Fig. 49. Bursting of 4 out of 100 chaotic Rulkov neurons in a network with all-to-all mean field coupling [Eqs. (43)]. Each neuron has a different value of α, chosen from a uniform distribution between 4.1 and 5. On the left, coupling strength ϵ is zero: neurons are disconnected and burst in different regimes. On the right, coupling is $\epsilon = 0.1$: bursts become synchronized and regularized. Other parameters are $\mu = 0.001$ and $\sigma = -1$. According to Rulkov [49].

4.2. Synchronization of bursts

Bursting neurons make up a variety of important neural and excitable cell systems, including pancreatic β-cells in charge of the secretion of insulin [56], the thalamic reticular nucleus responsible for rhythms during sleep [126], areas in the basal ganglia related to motor control [127], and central pattern generators that drive coordinated rhythmic tasks [128]. Two-dimensional map-based bursters, such as those of the Rulkov family, are, because of their simplicity, very well suited for the study of synchronous bursting.

Where burst synchronization is concerned, it is the relationships between the times of beginning and end of the bursts, and not the evolution of the state inside or between the bursts, that is important. For this reason studies of burst synchronization among map-based neurons do not look for the stricter forms of synchronization, and tend to be closer to physiologically relevant phenomena than to abstract coupled-map lattice problems. The coupling schemes employed are easier to relate to biological processes than in the cases presented in the previous section, and it may be helpful to classify burst synchronization studies according to the scheme of coupling employed:

Mean field coupling

Mean field coupling consists in the addition of a term proportional to the average membrane voltage of all interconnected neurons. This term is usually added to the voltage variable. Thus, in the case of chaotic Rulkov neurons, the equations of a mean-field coupled assembly of neurons are

$$\begin{aligned} x_i(n+1) &= \frac{\alpha_i}{1+x_i^2(n)} + y_i(n) + \mathcal{C}_i(n), \\ y_i(n+1) &= y_i(n) - \mu[x_i(n) - \sigma_i], \\ \mathcal{C}_i(n) &= \frac{\epsilon}{|\mathcal{N}_i|} \sum_{j \in \mathcal{N}_i} x_j(n), \end{aligned} \tag{43}$$

where ϵ represents the strength of coupling and, as in previous examples [Eqs. (35) and (42)], $\mathcal{N}_i$ is the set of neighbors of the i-th neuron.

Rulkov [49] studied mean-field coupling of chaotic Rulkov bursters with a random distribution of their parameters and found that it resulted not only in synchronized bursting but also in a regularization of the duration of the bursts, which in isolated neurons are of variable duration due to the heterogeneity in the parameters and the dependence of the end of the burst on the chaotic orbit. This effect can be seen in Fig. 49. With different values of α for each neuron, bursts of very different durations and duty cycles are present when neurons are uncoupled ($\epsilon = 0$), and for each neuron they are irregular along time; but the presence of coupling ($\epsilon = 0.1$) synchronizes all neurons in phase, and makes them burst at

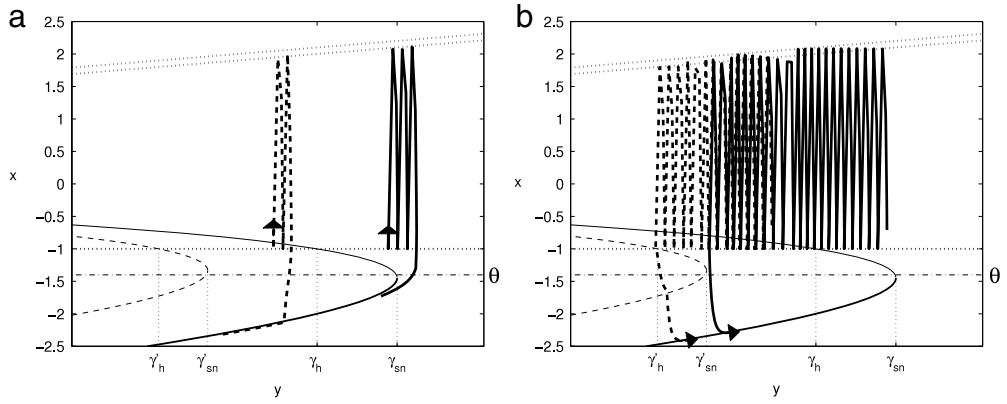

Fig. 50. Schematic effect of burst synchronization through either mean-field or FTM excitatory coupling. (a) When a neuron or group of neurons (represented by the solid traces and nullclines) reaches γ_{sn}, it begins to spike, and the coupling term shifts the fast nullcline of the other neurons (dashed traces) towards the left, drawing them into or closer to spiking. Thus burst initiation is synchronized. (b) When a neuron or group of neurons reaches $y = \gamma_h'$ (dashed traces) it jumps down into silence, shifting the fast nullclines of the other neurons (solid traces) towards the right, and thus bringing them into or closer to silence. Thus burst ending is synchronized.

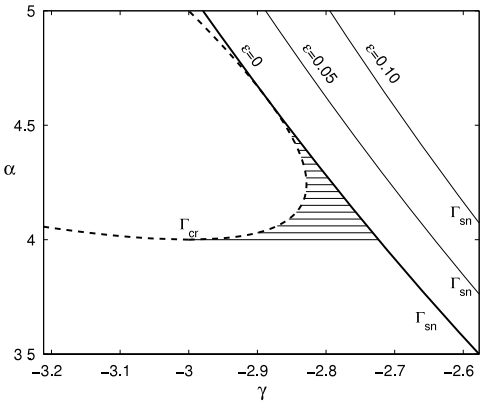

Fig. 51. Bifurcation diagram of the fast subsystem of the chaotic Rulkov neuron model [Eqs. (44)] in the α–γ plane. The dashed curve Γ_{cr} marks the external crisis bifurcation of the isolated neuron; curves Γ_{sn} of saddle–node bifurcations for different values of coupling ϵ [Eq. (45)] are represented. The dashed area signifies the bistability intervals for different values of α in isolated neurons that make burst durations widely differing; when coupling is present, differences are much less significant. According to Rulkov [49].

regular periods. The mechanism that synchronizes the bursts can be understood with the help of a nullcline diagram, as in Fig. 50. During the silent phase of the burst, the state of each neuron closely follows the stable branch N_s of the slow nullcline towards its vertex at $y = \gamma_{sn}$, where bursting begins [solid trace and nullclines in Fig. 50(a)]. When a neuron starts bursting, the coupling term of its neighbors (the whole network in all-to-all coupling) increases; this is equivalent to an increase in the recovery variable y (or parameter γ in the slow–fast decomposition), and is equivalent to a shift in the fast nullcline that places the neuron closer to its bifurcation [dashed nullcline in Fig. 50(a)], and hence bursting. As more neurons burst this effect amplifies in an avalanche, and in a short time the whole network is bursting. Similarly, during the active phase of a burst the state of the neurons slowly approaches the external crisis point $y = \gamma_{cr}$ where bursts end; when one neuron ceases bursting [dashed trace and nullcline in Fig. 50(b)], the coupling term decreases, effectively decreasing the value of y in all coupled neurons and driving them closer to the end of bursting [solid trace and nullcline in Fig. 50(b)].

The synchronization mechanism, as well as the high sensitivity of the durations of the bursts to the parameter α that can be appreciated in the left-hand side of Fig. 49, and the regularization that ensues from the coupling, as seen on the right-hand side of the same figure, are better understood with the help of a bifurcation diagram of the fast subsystem in the α–γ plane, depicted in Fig. 51. As already mentioned, in isolated neurons bursts begin at the saddle–node point γ_{sn} and end at the external crisis γ_{cr}; curves of such points as a function of α are labeled Γ_{sn} and Γ_{cr} in the figure. Burst duration is roughly proportional to the γ interval length between both curves, which is indeed very sensitive to α in the isolated case ($\epsilon = 0$). But, with mean-field coupling, the orbit of the neurons along the silent phase of the bursts changes. Since the neurons are synchronized, they share roughly the same value of x, and the coupling term $\mathcal{C}_i(n)$ in Eqs. (43) can to a very

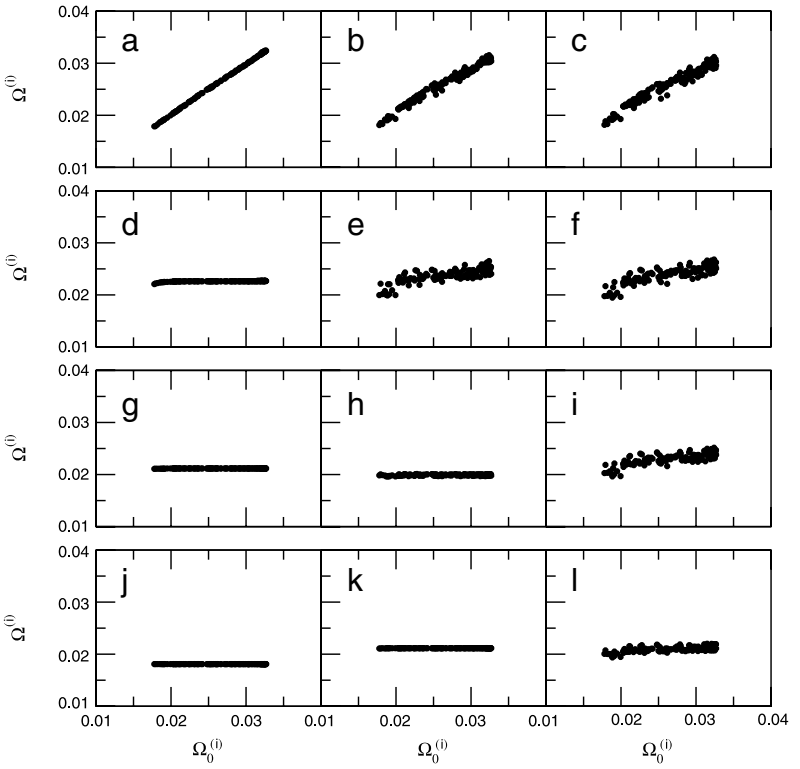

Fig. 52. Coupled bursting frequency $\Omega^{(i)}$ versus isolated bursting frequency $\Omega_0^{(i)}$ for a power-law mean-field coupled network [Eq. (46)] of chaotic Rulkov neurons, for different values of θ and ϵ. First column, $\theta = 0.5$; second column, $\theta = 2.0$; third column, $\theta = 4.0$. First row, $\epsilon = 0.015$; second row, $\epsilon = 0.035$; third row, $\epsilon = 0.045$; fourth row, $\epsilon = 0.07$. The networks have $N = 51$ neurons with parameter α randomly chosen between 4.1 and 4.4, $\mu = 0.001$ and $\sigma = -1$.
Source: From de Pontes et al. [131].

good approximation be replaced by $\epsilon x_i(n)$. Therefore, all neurons share the modified fast subsystem equation

$$x_i(n+1) = \frac{\alpha_i}{1+x_i^2(n)} + \gamma_i + \epsilon x_i(n). \tag{44}$$

The additional term makes the γ_{sn} point dependent on ϵ; the equation for the Γ_{sn} curve turns out to be

$$\alpha = \frac{2}{27\eta^2}\left[(\gamma^2 - 3\eta^2)^{3/2} - \gamma(\gamma^2 + 9\eta^2)\right], \tag{45}$$

where $\eta = 1 - \epsilon$. The result is a shift of the Γ_{sn} curve away from the Γ_{cr} curve, as seen in Fig. 51, and this, together with the avalanche mechanism explained above, lengthens and regularizes the bursting interval of all neurons. On the other hand, the Γ_{cr} curve is much less affected by the coupling, because the chaotic orbits of the neurons are mostly uncorrelated during the spiking phase and their average is close to zero. Indeed, Eq. (44) is a good approximation of the behavior of synchronized chaotic Rulkov neurons only during the silent phase of bursting. Duarte et al. [129] study the equation with the help of symbolic dynamics [130] to try to understand the effect of coupling on the chaoticity of the spikes along a burst, but, although the results are relevant to the dynamics of the map of Eq. (44), the same cannot be said with regard to the dynamics of the bursting ensemble.

The minimum mean-field coupling strength necessary for burst synchronization is highly dependent on network topology. As in the case of spike synchronization of Chialvo neurons described in the previous section [112], global coupling is better at synchronizing networks than nearest neighbor coupling. A quantitative study of the dependence is provided by Pontes et al. [131]. A coupling parameter is continuously varied that interpolates between a ring and an all-to-all structure; the coupling term $\mathcal{C}_i(n)$ in Eqs. (43) becomes

$$\mathcal{C}_i(n) = \frac{\epsilon}{\eta(\theta)} \sum_{j>0} \frac{1}{j^\theta}\left[x_{i+j}(n) + x_{i-j}(n)\right], \tag{46}$$

where $\theta \geq 0$ is a range parameter and $\eta(\theta)$ is a normalization factor that ensures that the total coupling strength is independent of the chosen topology. All-to-all coupling corresponds to $\theta = 0$, while $\theta = \infty$ yields a regular ring; intermediate values represent networks with connection strengths decreasing as a power-law of distance. A summary of numerical results of synchronization for different values of ϵ and θ is shown in Fig. 52. Networks of chaotic Rulkov

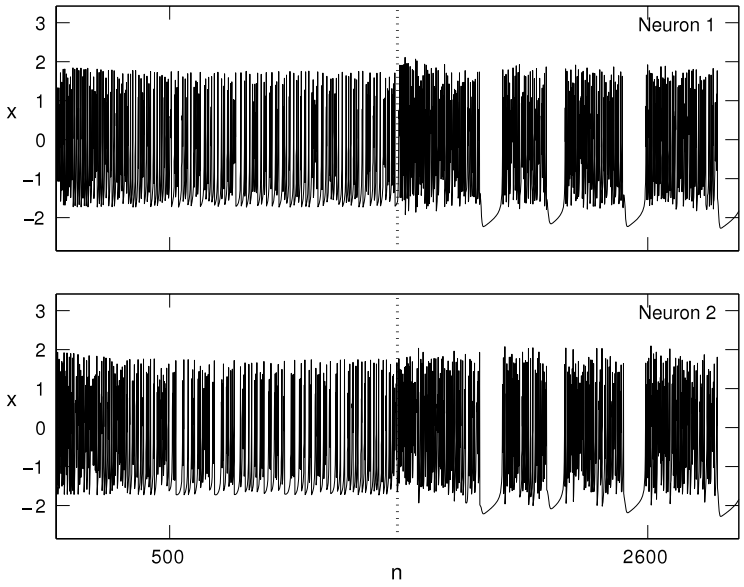

Fig. 53. Emergent bursting in two reciprocally mean-field coupled chaotic Rulkov neurons [Eqs. (43)] with $\alpha = 8\sqrt{3}/3$, $\mu = 0.001$ and $\sigma = -0.85$. Coupling is $\epsilon = 0$ before the vertical dotted line and $\epsilon = 0.2$ afterwards. Coupling turns non-bursting neurons into a synchronized bursting pair.

neurons with different intrinsic bursting frequencies (different values of α) synchronize with weaker coupling when the range parameter θ is smaller, that is, when the coupling range is wider.

Another study of the same system by Vries [132] showed that mean-field coupling could elicit bursting in non-bursting (tonically spiking) neurons. This phenomenon, called emergent bursting, is important in understanding the dynamics of pancreatic β-cells, which are known to produce the regular bursting necessary for proper insulin secretion only when enough of them are working in a connected assembly [133]. The explanation of the phenomenon of emergence is the same given above for synchronization of bursts. In the example of Fig. 53, both neurons have $\alpha = 8\sqrt{3}/3$, which is the value where the Γ_{sn} and the Γ_{cr} curves in the bifurcation diagram of Fig. 51 touch, no region of bistability exists and bursting is impossible. The neurons can only continuously spike or be quiescent when isolated. However, when they are coupled, the Γ_{sn} curve shifts to the right and an interval of bistability is created. Thus it is possible that neurons that are intrinsically non-bursting produce rhythmic bursts as a consequence of coupling. The phenomenon of emergent bursting is analyzed in the same system with negative mean-field coupling mimicking inhibitory interactions, via master stability functions [134], by Tanaka et al. [135]. Emergent bursting in networks of neurons of the Rulkov family has also been studied in the case of electrical and excitatory synaptic coupling [136], suggesting that it may be a pervasive phenomenon in large-scale networks of neurons.

An ensemble of map-based neurons that is coupled to burst in synchrony can be entrained by an external periodic signal injected in one or several of them [137,138,131,139]. The driving frequency should be close to the synchronized ensemble frequency, as shown in Fig. 54(a). The plateau of synchronization grows with driving signal amplitude up to a saturation level; notice that the plateau width is almost the same at $d = 0.09$ and $d = 0.15$. This is understandable, because the driving signal is injected into a single neuron: once this one is entrained, there is little room for improvement. More interesting is the fact that the plateau is asymmetric with respect to the free ensemble frequency: it enlarges with d almost exclusively in the direction of higher frequencies. Again, this can be explained by the avalanche mechanism: when the driving frequency is higher than the ensemble's, the driven neuron begins and ends bursting slightly ahead of the others and entrains them; however, when driving is slower, the ensemble takes the lead and entrains the driven neuron, making driving less efficient.

Another interesting result, which can be appreciated in Fig. 54(b), is that when the external drive is very strong and its frequency is higher than the plateau limit, synchrony breaks down. Suppressing synchronization by means of external control signals is a promising approach to the treatment of tremor [140] and possibly the prevention of epileptic seizures [141]. One particularly robust and practical desynchronization strategy is feeding back into the system a delayed copy of the mean field [142,143]. A numerical study of the system of Eqs. (43) with delayed feedback and scale-free topology can be found in Batista et al. [144].

Electrical coupling Electrical coupling is aimed at modeling gap-junctional synapses. It corresponds to a passive, resistive connection between the neuron bodies, and consists of a term proportional to the voltage difference between neighboring neurons. Thus the coupling term $\mathcal{C}_i(n)$ of an electrically coupled assembly of neurons is

$$\mathcal{C}_i(n) = \frac{g_e}{|\mathcal{N}_i|} \sum_{j \in \mathcal{N}_i} [x_j(n) - x_i(n)], \tag{47}$$

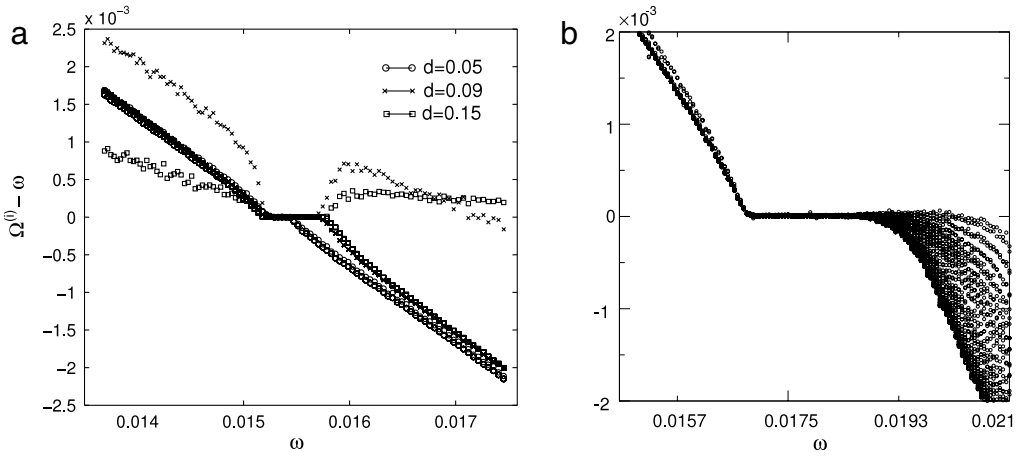

Fig. 54. (a) Mismatch between bursting frequency $\Omega^{(i)}$ and sinusoidal driving signal frequency ω in an all-to-all mean-field coupled network of 50 chaotic Rulkov neurons, for different values of driving amplitude d; each mark represents one neuron. Coupling strength is $\epsilon = 0.1$, neurons have $\mu = 0.001$, $\sigma = -1$ and $\alpha \in [4.1, 4.4]$. Only one neuron is driven. Outside the entrainment plateau, the driven neuron bursts at a frequency that is different from both that of the synchronized ensemble and of the driving signal (out-of-line marks). From Ivanchenko et al. [137]. (b) The same with power-law mean-field coupling, $\theta = 0.15$, and $d = 2$. Strong driving at high frequencies desynchronizes the whole network.
Source: From de Pontes et al. [131].

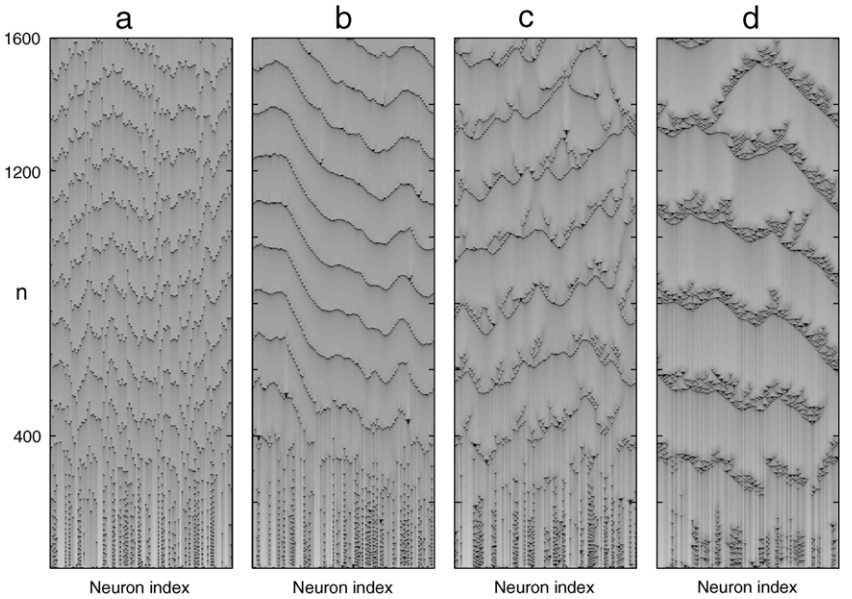

Fig. 55. Raster plots of the $x_i(n)$ variables of a ring of 100 non-chaotic Rulkov neurons coupled via gap-junctions. The value of the x variable of each Rulkov neuron is color-coded, darker for higher values. The neurons have parameters $\alpha = 3.5$, $\mu = 0.001$, and σ randomly distributed, $\sigma_i \in [-0.85, -0.84]$. Coupling conductances are (a) $g_e = 0.005$, (b) $g_e = 0.05$, (c) $g_e = 0.09$, (d) $g_e = 0.2$. Following Osipov et al. [145].

where g_e is the coupling conductance. By comparing Eqs. (47) and (43) it is obvious that mean-field and electrical coupling are very similar: electrical coupling just adds a negative $x_i(n)$ term that can be assimilated into the intrinsic dynamics of the neurons. Therefore, the synchronizing effects of mean-field coupling can also be seen with electrical coupling. However, electrical coupling having an immediate biological counterpart in gap junctions between neighboring neurons, studies of synchronization via electrical coupling rarely use all-to-all configurations and usually turn around specific network structures.

For example, Osipov et al. [145] explore the dynamics of a ring of electrically coupled non-chaotic Rulkov neurons. As already stated in the previous sections, locally coupled topologies such as rings are harder to synchronize than all-to-all networks. In Fig. 55(b), we see that neurons with slightly different rhythms (excitation σ is randomly distributed) synchronize when coupling g_e has moderate values; a front of activity forms, led by the most active neurons in the ensemble. Counter to intuition, increasing g_e in an attempt to improve synchronization produces a regime of chaotic intermittency [146], as seen in Fig. 55(c). Chaotic intermittency consists in the unpredictable alternation between phases

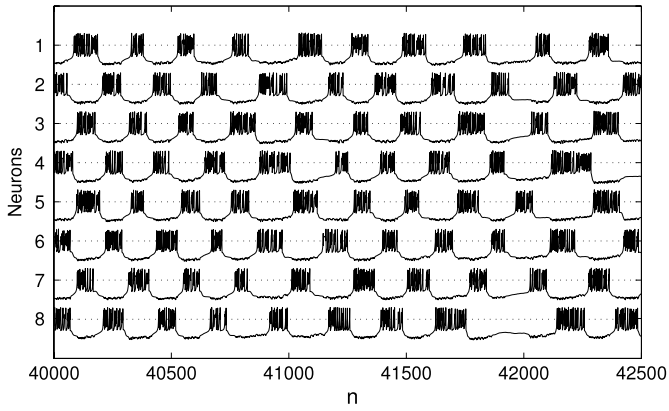

Fig. 56. Raster plots of the $x_i(n)$ variables of a ring of 32 identical chaotic Rulkov neurons coupled via negative linear junctions. The neurons have parameters $\alpha = 4.3$, $\mu = 0.001$, and $\sigma = -1.69$. Coupling conductance is $g_e = -0.02$.
Source: From Tanaka et al. [135].

of synchronized behavior and others of chaotic bursting. As with the emergent bursting cases previously described, spiking neurons are made to burst by the coupling, this time in a highly irregular fashion. The mechanism that generates the bursting phases, described in some detail by Ivanchenko et al. [136], can be summarized as follows: at strong values of electrical coupling, a spike elicited in a neuron by a neighbor's action potential can in turn produce a strong afterdepolarization in the first neuron, and in this fashion sequences of reciprocal spikes can be sustained until the slow recovery variable gets sufficiently far from excitable values. These chains of spikes propagate through the network and give rise to periods of chaotic bursting, separated by periods of synchronized spiking. The statistics of duration of the synchronized periods seem to conform to a power law. Chaotic intermittency is not limited to map-based models, being also observed in chains of ODE-based Hodgkin–Huxley neurons.

Some studies use negative conductance coefficients of electrical coupling [50,135,147]. This is questionable from the point of view of gap-junction modeling, but can be an expedient way to emulate inhibitory connections between neurons. The effect of negative electrical or linear coupling in a ring of neurons is to promote an *antiphase* state of synchrony, where neighboring neurons alternate their bursts, the one firing while the others are silent. This mode of activity can be seen in Fig. 56. In contrast with positive coupling, which promotes in-phase synchrony in any network topology, the effects of negative coupling create very different patterns of activity depending on the structure of the connections involved. This will be explored further in Section 4.3.

The appearance of irregular patterns of activity in electrically coupled networks is not necessarily linked to diversity in neuron parameters. In Tanaka et al. [135], a network of identical chaotic Rulkov neurons with negative electrical coupling is shown to produce, in a tight range of coupling conductance values, a highly complex mode of network activity, different from the chaotic intermittency described above, where successive ordered regimes of synchronization and wave propagation alternate in an unpredictable manner along time, as shown in Fig. 57. The source of the irregularity is the chaotic nature of the neurons, and the phenomenon can be framed in the wider concept of *chaotic itinerancy* [148].

Chemical synaptic coupling By chemical synaptic coupling we refer to coupling schemes that take into account relevant physiological parameters in order to model chemical synaptic connections between neurons. Synapses being in themselves complex systems, there exists some tension between the conflicting goals of fidelity to biology and the simplicity that lies at the heart of the map-based approach. A well-established departing point for simple yet biologically meaningful synapses, which is used extensively in dynamic clamp [149,150] experiments, is to model each synapse by the following equations [5]:

$$\begin{aligned} I_{\text{syn}}(t) &= -g(t)S(t)[V_{\text{post}}(t) - V_r], \\ \dot{S}(t) &= \frac{1}{\tau_{\text{syn}}} \frac{S_\infty[V_{\text{pre}}(t)] - S(t)}{S_1 - S_\infty\left[V_{\text{pre}}(t)\right]}. \end{aligned} \tag{48}$$

Here I_{syn} is the synaptic current entering the postsynaptic neuron, V_{post} is its membrane voltage, and V_{pre} is the presynaptic neuron membrane voltage. V_r is the reversal potential of the postsynaptic channels (depolarizing for excitatory synapses, hyperpolarizing for inhibitory synapses). The activation $S(t)$ is an internal variable of each synapse, and represents the amount of neurotransmitter docked on the postsynaptic cell relative to maximum; its dynamics are driven by presynaptic voltage through the sigmoidal activation function $S_\infty(V_{\text{pre}})$, between 0 and 1. Variable $g(t)$ is the maximal conductance, and may fluctuate along time following plasticity rules. There are two characteristic time scales for synaptic dynamics, the faster $\tau_{\text{syn}}(S_1 - 1)$ for *docking* of neurotransmitter to synaptic channel receptors, and the slower $\tau_{\text{syn}}S_1$ for *undocking*; therefore chemical synapses with different time courses can be modeled.

Some studies based on discrete-time neuron models make use of more or less straightforward discretizations of Eqs. (48) [55]. However, it is far more common to find them further simplified, tailored for specific purposes. A popular simplification is the so-called fast threshold modulation (FTM) model [151,152], which assumes that synapses are so fast that the activation

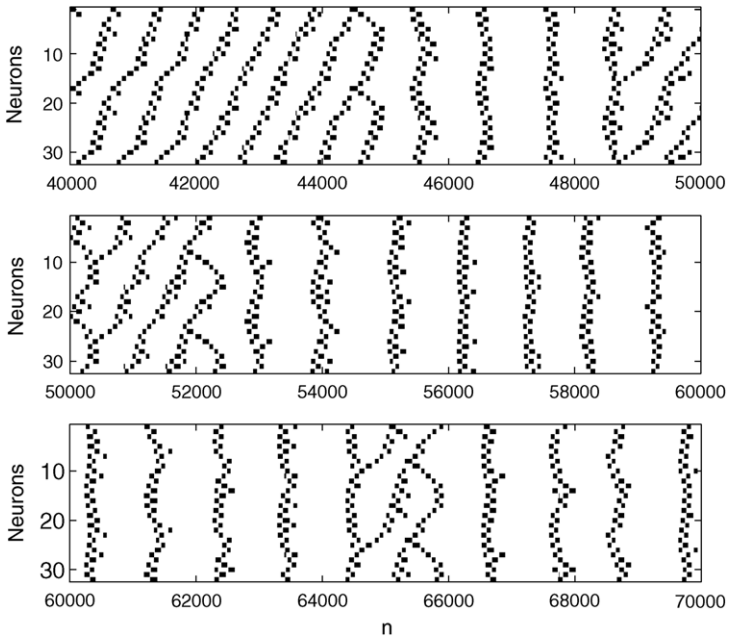

Fig. 57. Raster plots of the $x_i(n)$ variables of a ring of 32 identical chaotic Rulkov neurons coupled via negative linear junctions. The neurons have parameters $\alpha = 4.3$, $\mu = 0.001$, and $\sigma = -1.69$. Coupling conductance is $g_e = -0.02$.
Source: From Tanaka et al. [135].

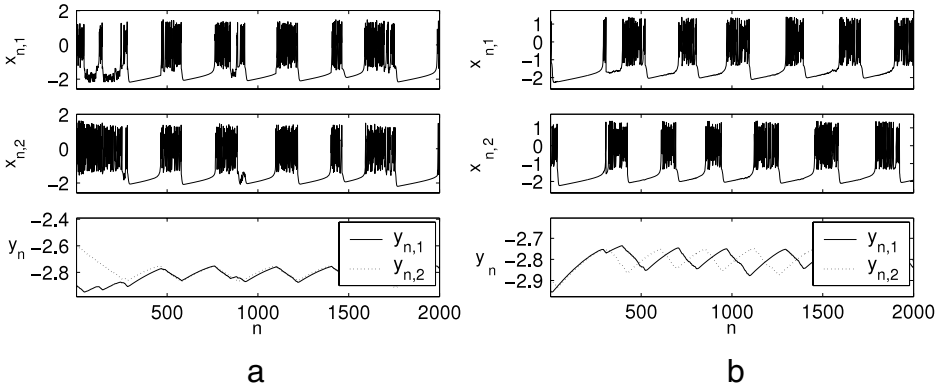

Fig. 58. Time evolution of two FTM-coupled [Eqs. (49)] chaotic Rulkov neurons, with $g_c = 0.1$ and $\theta_c = 0$. In (a), $x_r = 1$ (excitatory synapses). In (b), $x_r = -2$ (inhibitory synapses). Neuron parameters are $\alpha = 4.15$, $\mu = 0.001$ and $\sigma = -1.25$. Both the x and y variables are depicted.
Source: From Ibarz et al. [153].

variable instantaneously follows $S_\infty[V_{\text{pre}}(t)]$, and that the activation threshold is infinitely sharp. With FTM, the coupling term $\mathcal{C}_i(n)$ in Eq. (43) becomes

$$\begin{aligned} \mathcal{C}_i(n) &= \sum_k \mathcal{C}_{i,k}(n), \\ \mathcal{C}_{i,k}(n) &= \frac{g_{c,k}}{|\mathcal{N}_{i,k}|}\left[x_i(n) - x_{r,k}\right] \sum_{j \in \mathcal{N}_{i,k}} H[x_j(n) - \theta_{c,k}], \end{aligned} \tag{49}$$

where $H(x)$ is the Heaviside step function. Index k runs through the different types of chemical synapses. The parameters that define each one are $x_{r,k}$, the synaptic reversal potential (scaled to the values of variable x), and $\theta_{c,k}$, the presynaptic threshold of activation. With the FTM model there is no need to store dynamic variables of each synapse, synaptic currents being calculated instantaneously at each time step.

Ivanchenko et al. [136] reproduce the chaotic intermittency phenomena obtained with electrical synapses, as explained in the previous section, with excitatory FTM coupling. Indeed, in many respects, excitatory synaptic coupling produces synchronization effects similar to those of electrical coupling, and inhibitory synaptic coupling to negative electrical coupling. Ibarz et al. [153] investigate the dynamics of FTM-coupled Rulkov neurons. When two neurons are reciprocally coupled via excitatory synapses ($x_r = 1$), as in Fig. 58(a), they will synchronize in-phase; when through inhibitory synapses

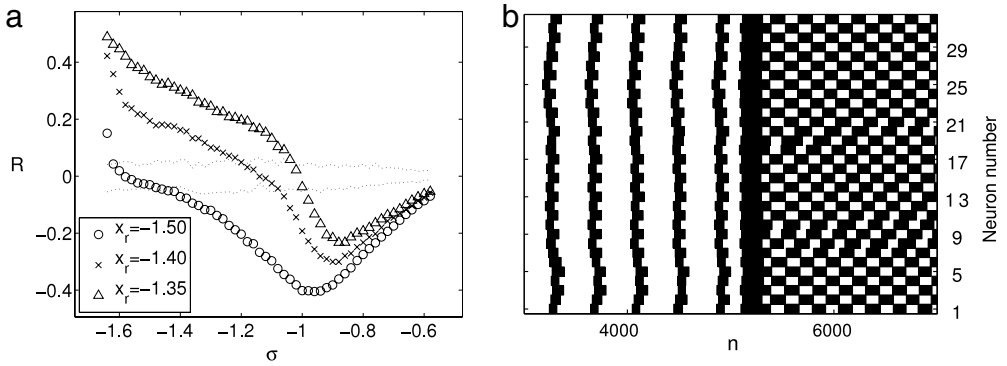

Fig. 59. (a) Cross-correlation of $x_{n,1}$ and $x_{n,2}$ as a function of external stimulation σ for two reciprocally FTM-coupled chaotic Rulkov neurons with $\alpha = 4.15$, $\mu = 0.001$, $g_c = 0.1$ and $\theta_c = -1.4$, for three different values of reversal potential x_r. (b) Raster plot of bursting in a ring of $N = 32$ non-chaotic Rulkov bursters with $x_r = -1.2$. At $n = 5000$, external stimulation σ switches from -1.2 to -0.8.

($x_r = -2$), as in Fig. 58(b), in anti-phase. This can be readily explained with the help of phase-plane diagrams, and is basically the same avalanche mechanism that tends to synchronize mean-field or electrically coupled neurons, displayed in Fig. 50. Further numerical explorations of these two cases are described in Shi and Lu [154].

For intermediate reversal potential values, the effects of synapses cannot be sharply categorized as excitatory or inhibitory. This is the case when modeling $GABA_A$ receptor channels, which, being selective for chloride ions, have a reversal voltage that lies close to the resting potential of the neuron. When intermediate reversal potential values between the excitatory and inhibitory extremes are employed in the FTM coupling model, synchronization can be controlled by means of external inputs. In Fig. 59(a) the cross-correlation between the x variables of two reciprocally FTM-coupled chaotic Rulkov neurons is plotted as a function of external stimulation σ, for three values of the reversal potential x_r. Positive cross-correlation is indicative of in-phase synchronization and vice versa. We see that, for $x_r = -1.4$, correlation reverses as σ changes. The effect is best appreciated in Fig. 59(b), where a ring of non-chaotic neurons coupled by FTM with intermediate reversal potential is made to switch from in-phase to anti-phase bursting by a change in applied stimulation. Numerical results about the effect of delays in this setting can be found in [155,156]. Cao and Ibarz [157] is a study of electrical coupling in the same context.

A major limitation of FTM coupling is that it leaves out the time scale of synaptic interaction, assuming it is instantaneous. A different elaboration of Eqs. (48) is used by Rulkov et al. [53] and Bazhenov et al. [89] that includes a time constant:

$$I_{syn}(n+1) = \gamma I_{\text{syn}}(n) - g_s \left[x_{\text{post}}(n) - x_r\right] \delta(n - n_{\text{pre},k}).$$

The set $\{n_{\text{pre},k}, k \in \mathbb{N}\}$ includes the time steps at which the presynaptic neuron has fired. The decay constant $\gamma < 1$ determines the undocking time scale; docking is instantaneous. The result is a form of pulse coupling, where each presynaptic spike contributes an exponentially decaying current waveform to the postsynaptic neuron. This model requires a new variable for each neuron and type of synapse; the effect of different synapses of the same type on one postsynaptic neuron can be accumulated in the same variable. The model is slightly awkward in that the postsynaptic voltage *at the instant of the presynaptic spike* determines the shape of the current pulse. A better approach is to use pulses of conductance, instead of current, and multiply them at each time step by the voltage term $[x_{\text{post}}(n) - x_r]$, as in [54]. In both studies short-term synaptic depression [158] is also included, so that synaptic conductance decreases every time a spike is fired and gradually recovers during silent periods.

4.3. Interplay between network topology and dynamics

Since excitatory interactions tend to promote in-phase synchronization, compact networks of excitatory bursters with sufficiently strong coupling tend towards an easily predictable state where all neurons fire together. However, when coupling is *inhibitory*, the synchronized state that results from the interactions has a rich dynamical structure that is dependent on network topology. Reciprocal inhibition is present in a variety of systems, including thalamic neurons during periods of sleep and drowsiness [126], dopaminergic neurons in midbrain, pancreatic β cells and central pattern generator (CPG) neurons responsible for rhythmic tasks such as swimming, walking, heartbeat and respiration.

In these systems, collective synchronous activity seems to be critical to the efficient processing of information. An example of pattern generator is shown in Fig. 60. It represents the stomatogastric ganglion of the shrimp, whose function is to generate the bursting patterns that operate pyloric muscles. The sequence of bursts that makes up the pattern is derived from the topology of the network, which, as we can see, is dominated by inhibitory interactions. It is of great interest to understand how the structure of these inhibitory networks determines the observed patterns. The topic has been investigated in the context of the winnerless competition principle and sensory encoding [160,161]. In both papers a network of inhibitory map neurons of the Rulkov type was used to reveal patterns of activation and deactivation of groups of synchronized neurons.

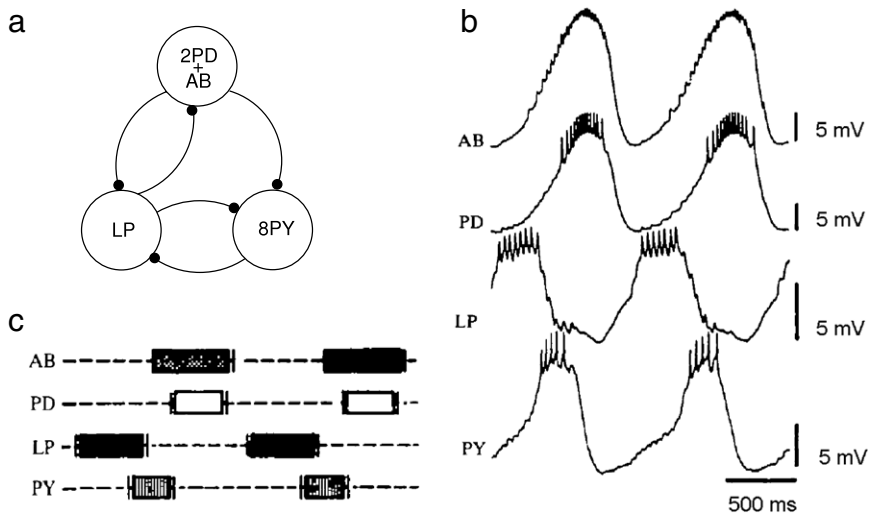

Fig. 60. (a) Structure of the stomatogastric ganglion of the crustacean *Homarus*. Black circles represent inhibitory synaptic connections. PD—Pyloric dilator neurons. LP—Lateral pyloric neuron. PY—Motoneurons. AB—Interneuron. The number of each type of neuron is indicated when more than one. (b) Voltage traces of each of the four types of neurons. (c) Raster of the burst pattern of this CPG. According to Meyrand and Moulins [159].

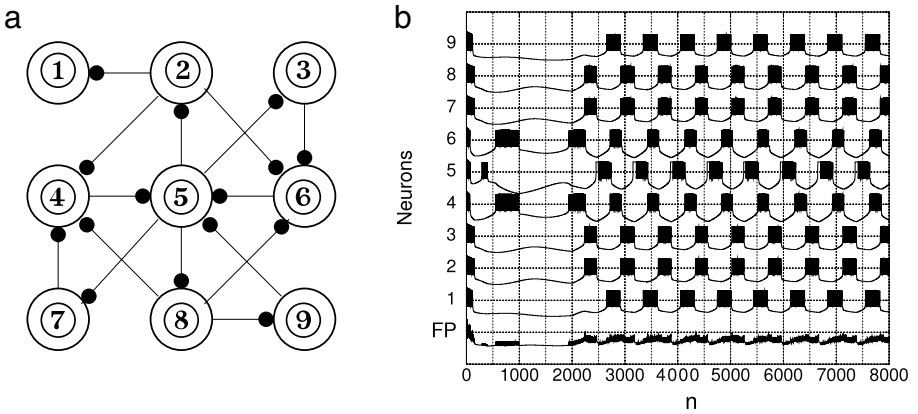

Fig. 61. (a) Neural network with nine neurons connected through directional inhibitory synapses. (b) Voltage traces generated by the network under the action of a suprathreshold stimulus of constant intensity. The stimulus is delivered to all neurons at $n = 2000$, and it consists in a sudden elevation of σ from -2.0 to 0.0, all neurons being stimulated in the same way. The plot labeled FP has been obtained by averaging the instantaneous values of all the spike trains.
Source: From Casado [160].

For example, Casado [160] used a small network of 9 non-chaotic Rulkov neurons to study the winnerless competition principle at the level of spiking neurons. In this case, the equations of the network are

$$\begin{aligned} x_i(n+1) &= F[x_i(n), y_i(n)], \\ y_i(n+1) &= y_i(n) - \mu \left[x_i(n+1) - \sigma - \sum_{j \in \mathcal{N}_i} g_c^{i,j} (x_j(n) - \theta_c) H(x_j(n) - \theta_c) \right], \end{aligned} \tag{50}$$

where $F(x, y)$ is the fast return map of the non-chaotic Rulkov model [Eqs. (14)]. Although at first sight the coupling looks similar to the fast threshold modulation scheme of Eqs. (49), notice that the coupling terms are simply proportional to presynaptic, and not postsynaptic, voltage. Thus the scheme is rather a form of thresholded mean-field coupling, with coefficients $g_c^{i,j} < 0$ to mimic inhibitory synapses. The choice of the neighborhoods $\mathcal{N}_i$ builds the network topology shown in Fig. 61(a). As shown in Fig. 61(b), the network develops a spatio-temporal pattern of firing that amounts to the transient activation and inactivation of four different assemblies of neurons. In fact, neurons labeled 1 and 9 fire in synchrony and the same occurs with neurons 2, 3, 7 and 8. Neurons 4 and 6 form another assembly, and neuron 5 alone constitutes the fourth group. Notice that, in spite of the links connecting only neighboring neurons, the different assemblies can include also non-neighboring units. Thus, inhibitory coupling induces a global structure on the whole network.

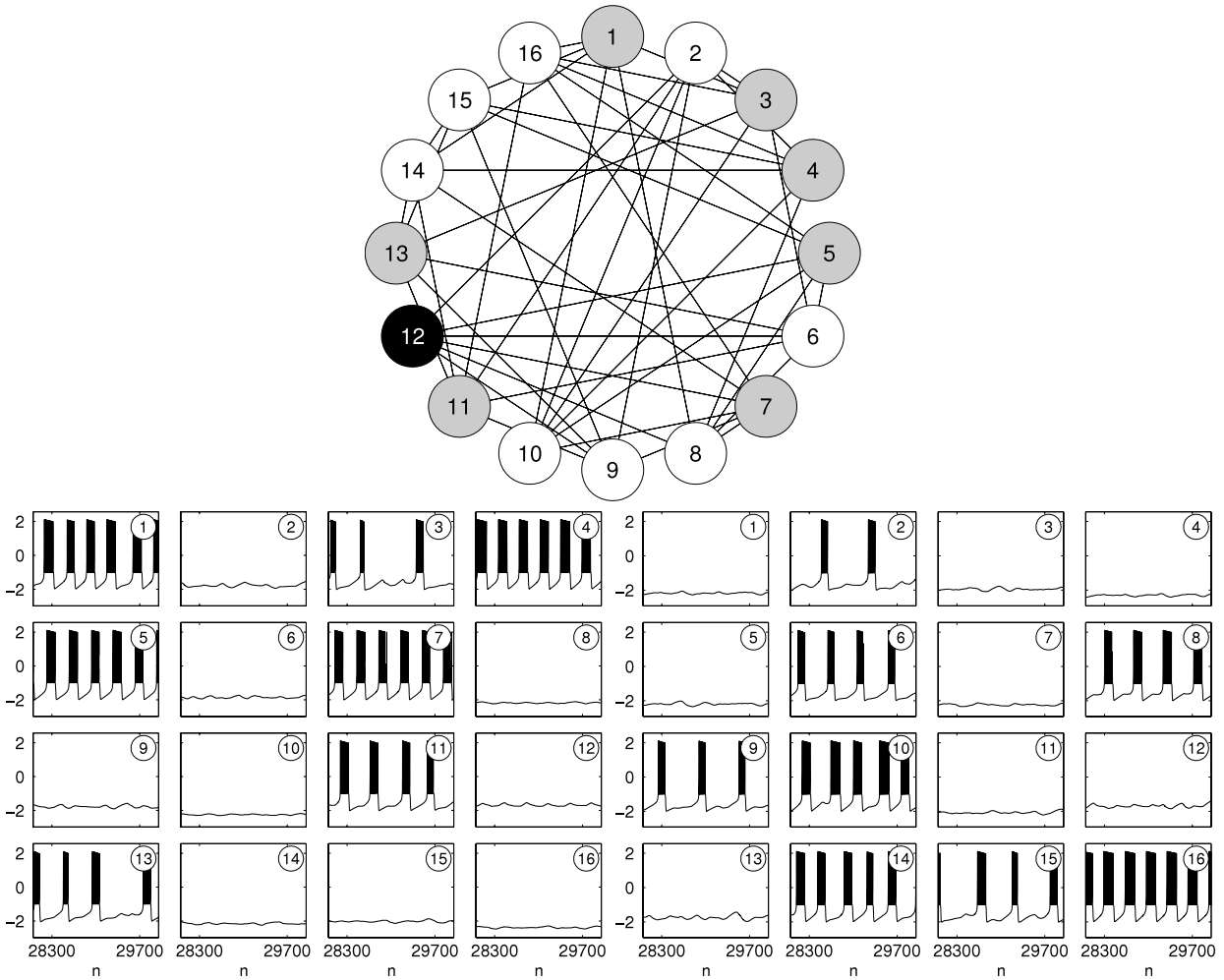

Fig. 62. Patterns of activity in a randomly generated balanced network of $N = 16$ neurons with $d = 6$ bidirectional connections per neuron. Top, the structure of the network. White and gray circles represent the two possible groups of active neurons when inhibition is strong ($g_c < -0.25$). Neuron 12 is inactive in all cases. Bottom, network activity when $g_c = -0.30$ for two different sets of initial conditions. On the left, only the gray neurons fire; on the right, white neurons fire. Other parameters are $\alpha = 6$, $\mu = 0.001, \sigma = -1$ and $\theta_c = -2$.
Source: From Ibarz et al. [162].

In some cases the network bursting pattern that arises from a particular topology can be predicted by the spectral properties of the network graph. Ibarz et al. [162] show, by means of linear stability analysis, that such is the case for networks of identical Rulkov neurons with direct inhibitory coupling and balanced inhibition. The latter property means that the weighted sum of synapses arriving at each neuron is the same, or, in terms of Eqs. (50), and considering that the coefficients $g_c^{i,j}$ constitute a matrix of connection weights, that the row sum $\sum_{j\in\mathcal{N}_i} g_c^{i,j}$ is a constant independent of i. This is a generalization of the concept of a balanced network [163] where the row sums are 0; in the present case, the constant row sum is negative.

The balance property together with homogeneity in neuron parameters ensures that the synchronized state where $(x_n^i, y_n^i) = (x_n^j, y_n^j)$ for any i and j is an invariant manifold of the system. Linearization of Eqs. (50) around this unique fixed point predicts the patterns of activity that result from the inhibitory interactions. An example of patterns in a 16-neuron, randomly generated, balanced network with reciprocal connections is shown in Fig. 62. Depending on initial conditions, one of two groups of neurons fires bursts while the rest of the network remains silent. The members of each of the two groups can be derived from spectral properties of the network graph, by calculating a so-called master stability function [134] of the system. The technique consists in decomposing the Jacobian of the system around the fixed points into as many modes as neurons make up the network. Each mode is associated to an eigenvalue and eigenvector of the network graph. A function can be built that provides the Lyapunov exponents of each mode for a given graph eigenvalue and given neuron parameters. The most unstable mode, as measured by the Lyapunov exponents it generates, will hopefully dominate the dynamics of the whole system, and the pattern of activity will be correctly predicted by the components of the corresponding graph eigenvector. With this, the influence of network topology in shaping the activity patterns is cleanly separated from that of individual neuron parameters, and a single function can predict the pattern generated by any network.

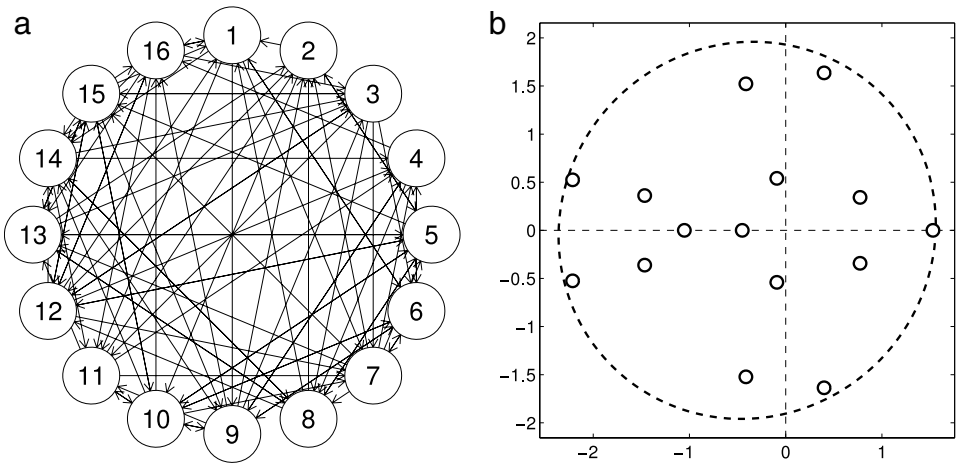

Fig. 63. (a) A balanced network of $N = 16$ neurons with $\nu = 6$ unidirectional input connections in each neuron. (b) Eigenvalues of the connectivity matrix of the network in the complex plane. The dashed circumference in the expected area of distribution of eigenvectors according to the circle law [164]. The eigenvalue $s_0 = 6$ is not shown.
Source: From Ibarz et al. [162].

In the case of the model of Eq. (50), the master stability function can be obtained analytically, and some conclusions may be drawn about the patterns that correspond to given topologies. It can be shown that the mode that corresponds to the graph eigenvalue with the most negative real part dominates the dynamics. In the example of Fig. 62 all connections are reciprocal, and therefore the graph adjacency matrix is symmetric and eigenvalues are real. The most negative eigenvalue corresponds to the eigenvector

$$\mathbf{v} = (0.33, -0.05, 0.12, 0.37, 0.32, -0.09, 0.34, -0.29, -0.08, -0.34, 0.20, 0.03, 0.07, -0.27, -0.17, -0.40).$$

The signs of each component of the eigenvector indicate the direction of evolution of the variables of each neuron when they are close to the fixed point. Observe that the two groups of neurons of Fig. 62 correspond to eigenvector elements of the same sign. Neuron 12, which was inactive in both cases, has the smallest component; it is only weakly excited with this mode, and the suprathreshold pattern of the network prevents it from bursting. The eigenvector components sum up to zero; this holds for any symmetric matrix with constant row sums because of orthogonality with respect to the all-ones eigenvector. Therefore there will be about the same number of negative and positive components in the dominant eigenvector of any symmetric network, and neurons will split into two groups of similar size, one or the other being active depending on initial conditions.

When a network has an additional degree of symmetry, it is reflected in its spectrum, and activity patterns conform to it. For example, in a two-dimensional lattice the symmetry produces a pair of identical, dominant eigenvalues, and their combinations explain the activity patterns of neurons synchronized either in rows or in columns, depending on initial conditions.

When connections are not reciprocal, eigenvalues of the connectivity matrix will generally be complex. Fig. 63(a) shows a randomly generated balanced network of $N = 16$ neurons with unidirectional connections and total input degree $\nu = 6$ for each neuron. Its dominant mode is defined by a pair of complex conjugate eigenvalues, which share the most negative real part. As a consequence, the mode is defined by a pair of conjugate eigenvectors producing oscillations.

Fig. 64 shows the time evolution of the network of Fig. 63 for two values of g_c, one barely past the loss of stability of the fixed point of the network, and the other with slightly stronger inhibition. Oscillations just above the bifurcation are subthreshold, almost linear and stable (the bifurcation is supercritical). They are slow, and their frequency can be predicted analytically. Amplitude and phase of the oscillations is encoded in the modulus and angle of the complex components of any of the two eigenvectors; these are depicted in the left part of the figure. As inhibition grows the oscillations also grow and we should expect the neurons corresponding to the components of maximum modulus to be the first to burst. In the example, neurons 13 and 5 have the highest amplitudes but neuron 5 does not burst, while smaller amplitude neurons 10, 12 and (sometimes) 8 do. This is a clustering effect. Neurons 10 and 12 have high amplitudes and phases similar to neuron 13; when the latter bursts, it boosts neurons with a similar phase to do the same, and draws neurons in the opposite part of the cycle toward negative voltages (notice the notches in the voltage trace of neurons 5, 7, 14, 15 and 16). This lowers the subsequent maximum of their oscillation and prevents them from firing. If due to initial conditions neuron 5 fires first, it may carry neurons 7 and 16 with it, but their combination is weaker than that of neurons 13, 12 and 10 and unable to prevent their bursts. Interestingly, although all synapses are inhibitory, some neurons have indirect excitatory effects on each other due to mode formation.

When inhibition goes further beyond the instability threshold, oscillations grow in all neurons and different patterns emerge. Fig. 65 shows raster plots of network activity for three values of g_c. Notice how the phase sequence of eigenvector components in Fig. 64 is roughly observed, with neurons corresponding to low-amplitude components joining the pattern

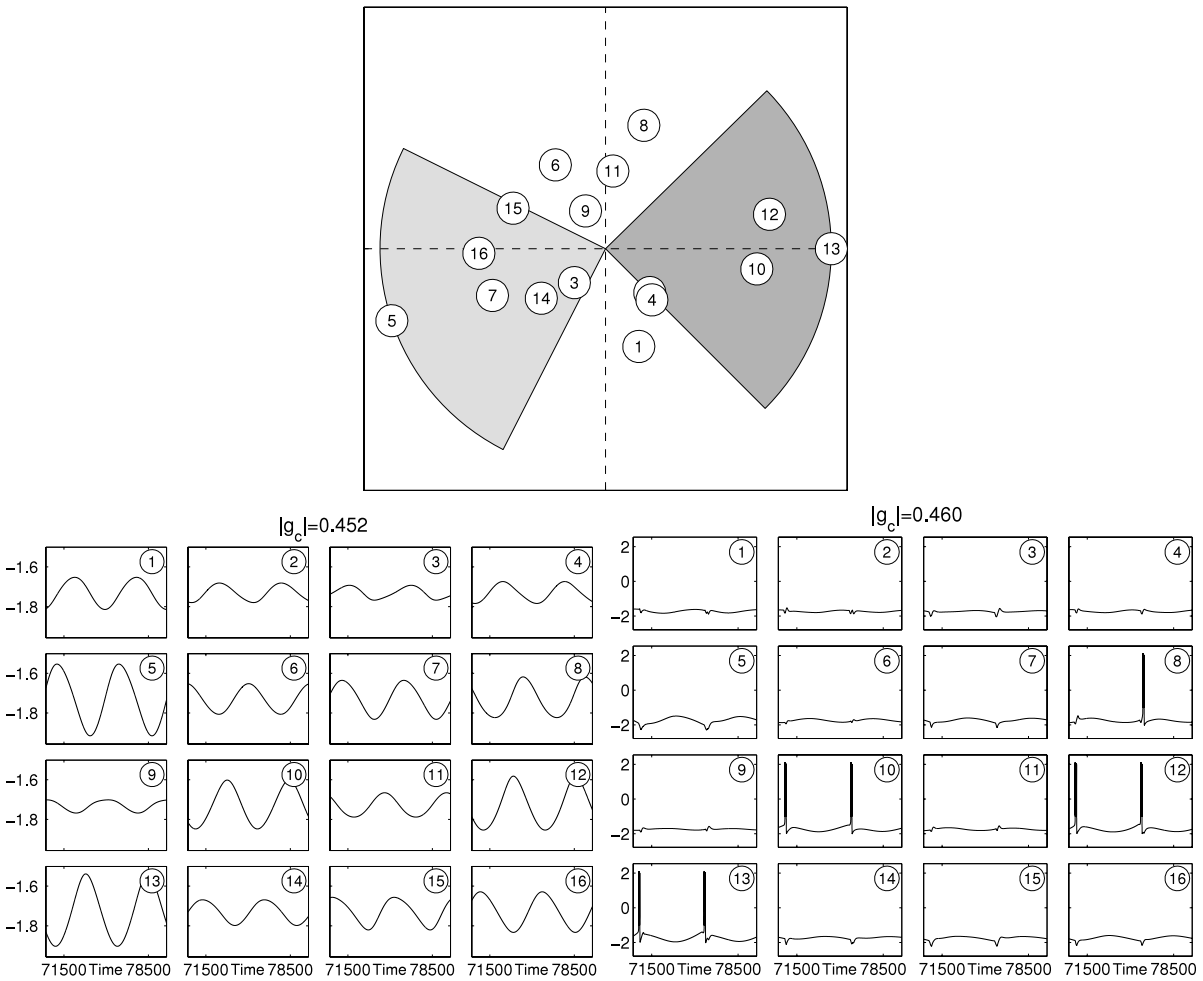

Fig. 64. Upper panel: complex plane with the components of one of the two conjugate eigenvectors of the dominant mode of the network in Fig. 63. The dark gray sector spans 90° around component 13, and light gray around component 5, to help see groups of neurons tending to burst together. Below, left: activity in the network barely past instability of the fixed point of the network. Note that amplitudes and phases correspond with the eigenvector component diagram. Right: activity for slightly stronger inhibition.
Source: From Ibarz et al. [162].

as inhibition increases. High-amplitude-component neurons may burst several times in each cycle, because their slow-wave oscillation remains above bursting threshold long enough to fit more than one burst.

Thus symmetry, balance and most importantly the spectral properties of the topology determine the activity patterns observed in networks of bursting inhibitory neurons. Networks with nonreciprocal connections may have a complex dominant mode and generate a rhythmic behavior marked by the slow subthreshold oscillations over which the bursts ride. This contrasts sharply with symmetric networks (or asymmetric with a real dominant mode) where the only rhythm present is the fast intrinsic bursting frequency, and where two mutually exclusive groups form and only one of them is active, depending on initial conditions.

A different collective pattern of interest in networks of map-based models is propagation of activity. In some of the previously reviewed studies dealing with synchronization, wave-like propagation has also been found in regimes and topologies that could not sustain global synchrony [145,136,135]. Rulkov et al. [53] used modified non-chaotic Rulkov neurons to build a biologically plausible model of cortical network and study the dependence of activity patterns on connection parameters. The synaptic model used in this study was described in Section 4.2; some more details about the model will be given in Section 5.1. The networks have two types of neurons: regular-spiking excitatory neurons, that play the role of pyramidal (PY) cells, and fast-spiking inhibitory neurons, that play the role of interneurons (IN). Each neuron type forms a layer, and both layers are reciprocally coupled: neurons in the PY layer send synapses to their immediate $L_{\mathrm{PY-PY}}$ neighbors, with conductance $g_{\mathrm{PY-PY}}$, and to the nearest $L_{\mathrm{PY-IN}}$ neurons in the IN layer, with conductance $g_{\mathrm{PY-IN}}$; neurons in the IN layer, in turn, send synapses to the nearest $L_{\mathrm{IN-PY}}$ neurons in the PY layer, with conductance $g_{\mathrm{IN-PY}}$. Two topologies are investigated: one-dimensional chains and two-dimensional lattices.

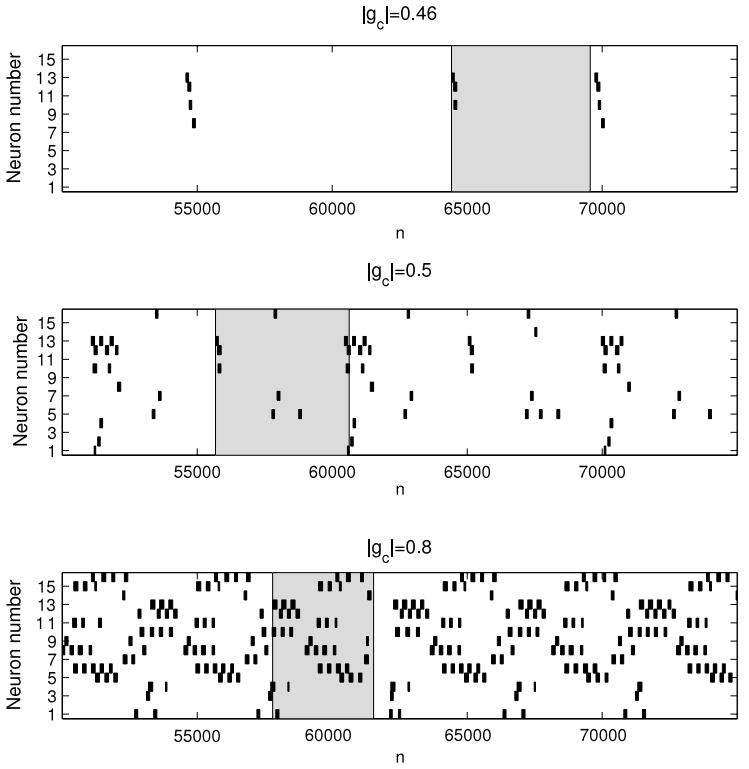

Fig. 65. Raster plots of the activity in the network of Fig. 63 for different strengths of inhibition. Black patches mark bursting periods of each neuron. Gray areas mark the length of the period predicted analytically.
Source: From Ibarz et al. [162].

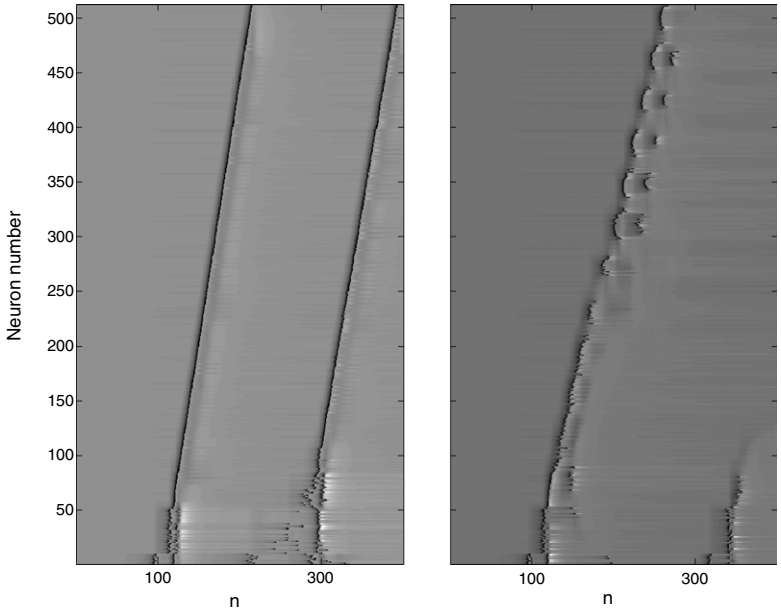

Fig. 66. Propagation of the wave front of excitation in a two-layer chain of interconnected PY and IN neurons. On the left, $g_{PY-IN} = 3.0$, and propagation takes place at constant velocity. On the right, $g_{PY-IN} = 6.0$, and the velocity is modulated periodically. All other parameters are identical in both cases, with $g_{PY-PY} = 5.4$ and $g_{IN-PY} = 6.0$. $L_{PY-PY} = 49$, $L_{PY-IN} = 51$, $L_{IN-PY} = 5$. The wave is triggered by an external stimulus applied for a brief period of time to the first few neurons in the chain. The value of the x variable of each PY neuron is color-coded, darker for higher values. Simulations performed with software used in Rulkov et al. [53].

In a one-dimensional chain, a stimulus delivered at a certain point in the network propagates with a velocity that depends on the coupling parameters, and in particular on the balance between excitatory and inhibitory interactions. Two different modes of propagation are represented in Fig. 66: in Fig. 66(a), where synapses from excitatory neurons to inhibitory neurons

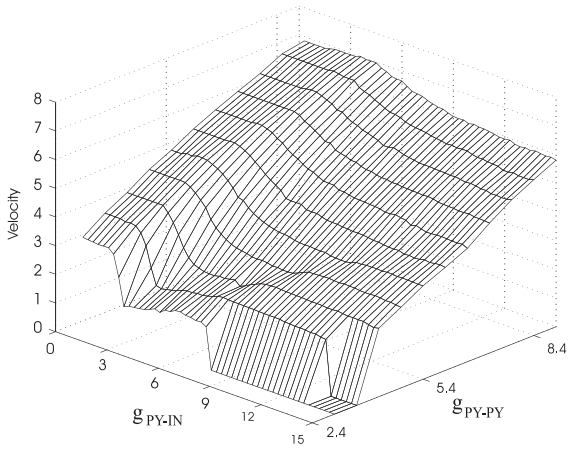

Fig. 67. Velocity of the wave front propagation of an excitation burst in a two-layer chain of interconnected PY and IN neurons, as a function of the coupling parameters g_{PY-PY} and g_{PY-IN}, with $g_{IN-PY} = 4.2$, $L_{PY-PY} = L_{PY-IN} = 50$ and $L_{IN-PY} = 12$. Units of velocity are sites per iteration.
Source: From Rulkov et al. [53].

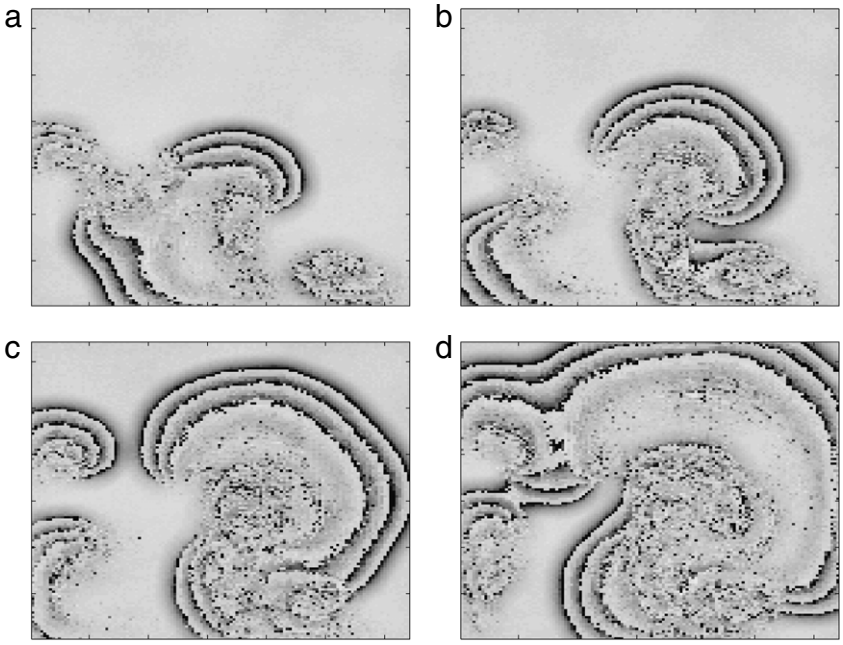

Fig. 68. Four consecutive snapshots of the activity of PY neurons in a two-layer lattice of 128×128 PY and 64×64 IN neurons, with $L_{PY-PY} = L_{PY-IN} \approx 200$ neurons and $L_{IN-PY} \approx 12$ neurons. Conductances are $g_{PY-PY} = 11$, $g_{PY-IN} = 4.2$ and $g_{IN-PY} = 1.2$. Other parameters are described in Section 5.1. The value of the x variable of each PY neuron is color-coded, darker for higher values. Snapshots are separated by 30 time steps. Boundary conditions are open. Simulations performed with software used in Rulkov et al. [53].

are relatively weak, the wave of activity propagates at a constant velocity. But with increased PY-IN coupling, as in Fig. 66(b), the propagation front becomes uneven, with periodic variations in velocity. The relationship between propagation velocity and coupling parameters can be numerically investigated. Some interesting trends, such as the monotonous increase of propagation speed with PY-PY coupling, or its non-monotonous dependence with PY-IN coupling, are apparent in Fig. 67. These phenomena can be reproduced as well with classical Hodgkin–Huxley models, at a much higher computational cost.

Finally, when the network topology is two-dimensional new propagation modes are possible, such as the rotating spiral waves generally observed in excitable media. An example can be seen in Fig. 68. As in the case of the chain, the properties of the two-dimensional waves are affected by the coupling parameters, as well as by the size of the network. The results do not differ qualitatively from those obtained in models of Hodgkin–Huxley neurons. Rulkov and Bazhenov [54] further investigated the relationship between patterns and coupling, showing that globally synchronized modes are possible as well solely by means of PY–IN and IN–PY coupling. Bazhenov et al. [165] studied the origin of these patterns with extensive simulations – feasible thanks to the map-based nature of the models – with different topologies (1D, 2D with various

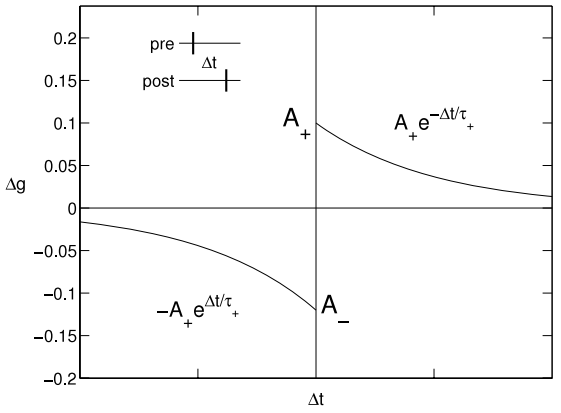

Fig. 69. The STDP rule used by Izhikevich [168]. Excitatory chemical synaptic conductances increase after each postsynaptic spike when it comes after a presynaptic spike, and decrease after each presynaptic spike when it arrives later than the postsynaptic one, by the amounts depicted. Parameters used are $A_+ = 0.1, A_- = 0.12, \tau_+ = \tau_- = 20$ ms.

connection neighborhoods). These provide support to the hypothesis that global synchrony or near-synchrony, as opposed to wave-like patterns, is not so much favored by extensive or long-range connections as by the existence of several connecting paths between any pair of neurons in the network. It may be interesting to attempt to link this criterion to topology-based theoretical criteria for synchrony, such as the connection graph stability method [166] or the master stability function method [134]. A brief study of the influence of noise on 2D spatially correlated patterns can be found in [167].

The above-mentioned works study the dynamics resulting from a fixed network topology. However, nervous systems are eminently plastic, the conductance of synapses being dependent on the activities of pre- and postsynaptic neurons. The dynamic interplay between topology and activity constitutes an additional level of complexity and is a rich source of new phenomena. Izhikevich [168] investigates a sparsely connected (10% probability) network of 1000 Izhikevich neurons, 800 excitatory and 200 inhibitory, evolves in time subject to a spike-timing-dependent plasticity (STDP) rule [169]. STDP has been experimentally demonstrated in a number of different preparations [170] and is a proven mechanism for Hebbian learning [171,3]. It consists in reinforcing (potentiating) a synapse when a presynaptic spike arrives a short time before a postsynaptic spike, and weakening (depressing) it when the postsynaptic spike precedes the presynaptic one. In this way, synapses increase their efficacy if they consistently cause the postsynaptic neuron to fire. The rule can be represented as a function that maps the time difference between presynaptic and postsynaptic spikes to increments in conductance, as in Fig. 69. The plasticity effect decays exponentially with the delay between pre- and post-synaptic neurons, with a time constant of the order of tens of milliseconds. Hard limits are imposed upon the conductance to avoid explosive behavior.

The dramatic effects of plasticity upon network dynamics can be appreciated in Fig. 70. The STDP rule (Fig. 69) is slightly biased towards negative increments, so that random spikes lead to weakening of synapses; this has an important homeostatic effect, and quickly leads the network to a state of balance between excitation and inhibition, irrespective of initial connection weights. As different synapses compete to activate the same postsynaptic neuron, the most successful ones (either by chance or through correlated activation via sensory stimuli, for example) strengthen to maximum, while the unsuccessful synapses die out; the ratio of strong versus weak synapses depends on global external excitation. All this is in accordance with theoretical results [172]. At the same time, a rhythmic behavior sets in in the gamma band of frequencies; it is suggested that its mechanism is that of the so-called pyramidal-interneuron network gamma oscillations (PING) [173]. Considerations by Izhikevich [168] go further in studying the effect of random delays of up to 20 ms at every synapse. Strong synapses build tightly interconnected groups of neurons that tend to fire in sequence; the existence of delays allows neurons to belong to many such groups that may be activated independently by different stimuli, encoded in the temporal sequence of a few triggering spikes. The emergence of these so-called *polychronous groups* had been noticed before in a larger, more ambitious model of cortex [174]; this model would, on the one hand, be enlarged to produce a complete, detailed thalamo-cortical model [175], commented in Section 5.1, and, on the other hand, simplified [168] in order to study polychrony. Although some observations are made there as to the combinatorial potential of such groups, their computational consequences deserve further study, and map-based models allow the extensive simulations necessary.

Masuda and Kori [176] contributed another study that explores the consequences of STDP for network synchronization. Here theoretical considerations using phase models are supplemented by simulations with Izhikevich neurons. In both cases it is shown that STDP with nearly balanced potentiation and depression can facilitate the assimilation of the firing frequencies of an ensemble of neurons to that of a driving pacemaker neuron, and stimulate the formation of feed-forward chains originating from the pacemaker, depressing backward connections.

At a more abstract level, the interplay between plasticity and synchronization has been studied using logistic-map netlets as nodes [177,85]. Interaction between the netlets takes the coupled-map lattice form of Eq. (35). The connections are initially random, with a 10% probability between any given pair. A Hebbian plasticity rule is implemented: every 1000 iterations of the system, a node is randomly chosen and one of its connections is rewired depending on synchrony. The

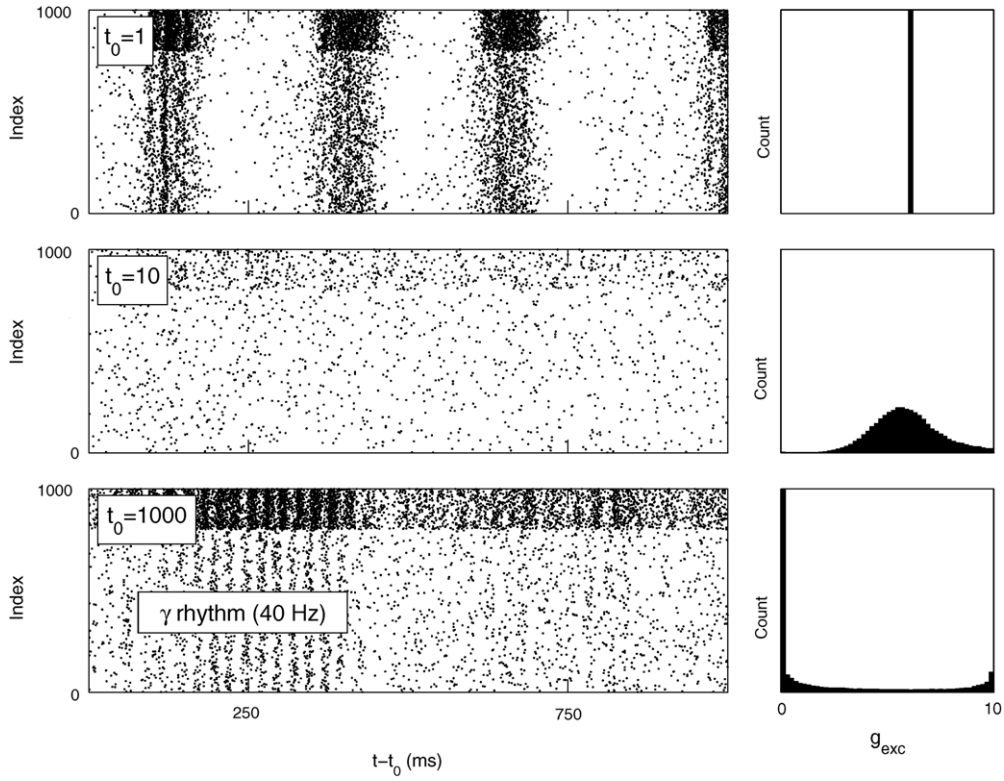

Fig. 70. Rasters of one second of activity (left), and histogram of the synaptic conductances of the excitatory connections (right) at different moments of a single simulation of a network with STDP [168]. Neurons 1 to 800 are excitatory, 801 to 1000 are inhibitory. Initial weights, arbitrarily set to make all excitatory synapses strong ($g_e = 6$), produce a marked 3-Hz rhythm during the first second (top). Soon the STDP rule redistributes the weights (middle) and activity becomes uncorrelated and sparse. Competition among synapses polarizes the synaptic weight, so that after some time most are either very weak or maximally strong. After some time, a regime of correlated activity, with a rhythm in the range of 30 to 70 Hz, emerges (bottom). The input to the network is random. Following Izhikevich [168] using code by E.M. Izhikevich, downloadable at www.izhikevich.com.

connected node whose orbit has been least similar to the one selected is disconnected, and the link redirected to the non-connected node with the most similar orbit. As a result, the initial random architecture develops into a highly clustered [113] and modular [178] network. This evolution takes place preferentially when the netlets are in a chaotic regime. The modular network is characterized by sets of highly interconnected, and synchronous, nodes. Few links are established across modules. Interestingly, the structural role of a node can be assessed from its return map. Because the netlets are not isolated, a plot of the return map of a node does not fall in a line, but has a thickness that depends on how heterogeneous its inputs are. As shown in Fig. 71, network hubs, that is, netlets connected to nodes in different modules, have noisy return maps that reveal the variety of desynchronized inputs they received, while peripheral nodes, connected mostly inside their own module, have low-dimensional dynamics.

5. Modeling with map-based neurons

Studies on the dynamical properties of map-based neuron models, as those reviewed in the previous sections, are intended to provide guidance for modeling actual phenomena and properties of nervous systems. In this section we comment on representative modeling studies that have employed the map-based neuron models described.

5.1. Fitting the models to real neurons

A major challenge of modeling with map-based neurons is relating the phenomenological parameters of the models to biophysical parameters. This can be done by fitting model behavior to experimental data or, more conveniently, to other neuron models with parameters that directly reflect biophysical properties. The latter approach is exemplified in the above-mentioned study [53] of modeling of cortical dynamics, where previous work based on Hodgkin–Huxley type neurons [179] is reproduced with non-chaotic Rulkov maps. Three classes of cortical neurons are modeled: regular-spiking (RS), fast-spiking (FS), and intrinsically bursting (IB), although only the first two are used in the network model. The classification is based on the firing patterns of the neurons in response to injection of a DC current pulse. RS neurons display an initial high frequency response followed by spike frequency adaptation, a typical behavior of excitatory pyramidal (PY) neurons.

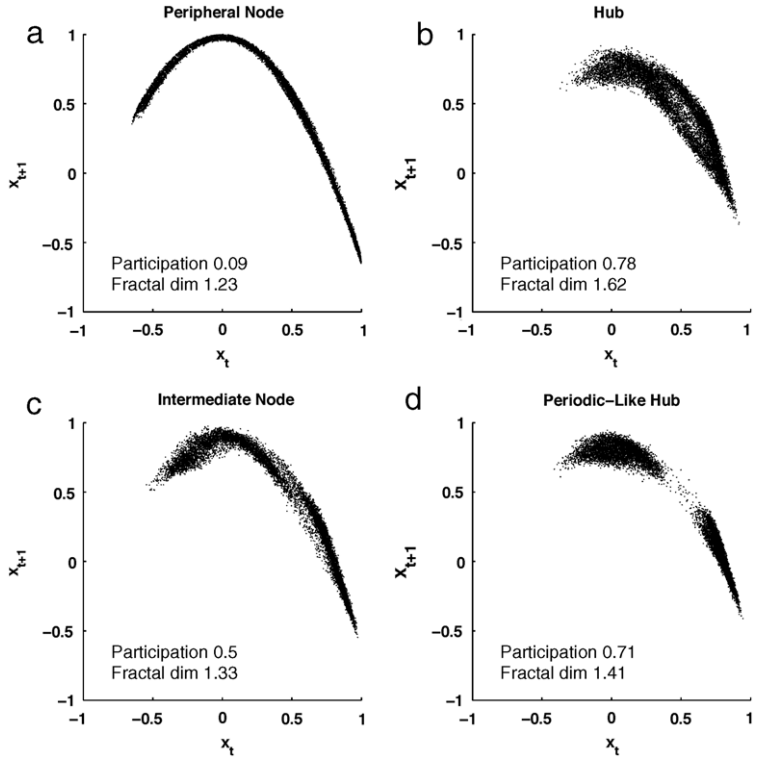

Fig. 71. Return maps of logistic netlets at different positions in a network that has evolved according to an unsupervised Hebbian rule. Peripheral nodes are connected mostly to neurons in their own module; the synchronized inputs result in one-dimensional chaotic dynamics. For hubs the opposite is true. Participation is a measure of centrality that assesses the modular heterogeneity of a node's links. All nodes have chaotic dynamics, except D, which is periodic.
Source: From Rubinov [85].

Meanwhile, FS neurons are characterized by constant spiking frequency without adaptation over the duration of the pulse, and include many cortical inhibitory interneurons (IN). Lastly, IB neurons fire an initial burst of very fast spikes followed by non-adaptive spiking, a response also observed in pyramidal neurons. A comparison of *in-vivo* recordings of the three types of patterns with the corresponding Hodgkin–Huxley models and map-based models is displayed in Fig. 72. A fourth type, the low-threshold spiking (LTS) interneuron, is modeled in [54] to include rebound responses to hyperpolarizing pulses.

In order to control spike frequency adaptation, a slightly modified form of Eqs. (13), already suggested in Rulkov [50], is used for the RS and IB cases:

$$\begin{aligned} x(n+1) &= F[x(n), y(n) + \beta^e I(n)], \\ y(n+1) &= y(n) - \mu[x(n) - \sigma - \sigma^e I(n)]. \end{aligned} \tag{51}$$

The modification consists in injecting external currents $I(n)$ simultaneously in the fast and slow variable equations, scaled by different constants: β^e, for the fast subsystem, controls the transient adaptation effect, as described in Section 3.1, while σ^e controls the sensitivity of the firing rate to the stimulus. Detailed phase diagrams and indications for modeling with these parameters are given by Rulkov and Bazhenov [54]. In the case of FS neurons the model is extended to include a different property, spike afterhyperpolarization. This effect finds expression as a negative excursion of voltage, below baseline, after each spike of the neuron. In order to capture it, and since this neuron class does not exhibit bursting or adaptation, the slow variable y in Eq. (13) is replaced by a negative phenomenological current I^{hp}, yielding

$$\begin{aligned} x(n+1) &= F[x(n), y^0 + \beta^{hp} I^{hp}(n) + \beta^e I(n)], \\ I^{hp}(n+1) &= \gamma^{hp} I^{hp}(n) - g^{hp} \sum_k \delta(n - n_{sp,k}), \end{aligned} \tag{52}$$

where $n_{sp,k}$ is the time step of the k-th spike of the neuron. Thus every time the neuron fires it gets a negative, exponentially decaying current pulse that pulls it towards hyperpolarized voltages.

The dynamic phenomena observed in the cortical network built with the modified models, described in Section 4.3, is similar to the slow-wave sleep (SWS) oscillations that dominate cortical activity during natural sleep and under some types of anesthesia [126]. These oscillations are linked to transitions between so-called *up* and *down* states. Up states are characterized by depolarized, highly noisy, near-threshold membrane potential, while down states consist of lower, less

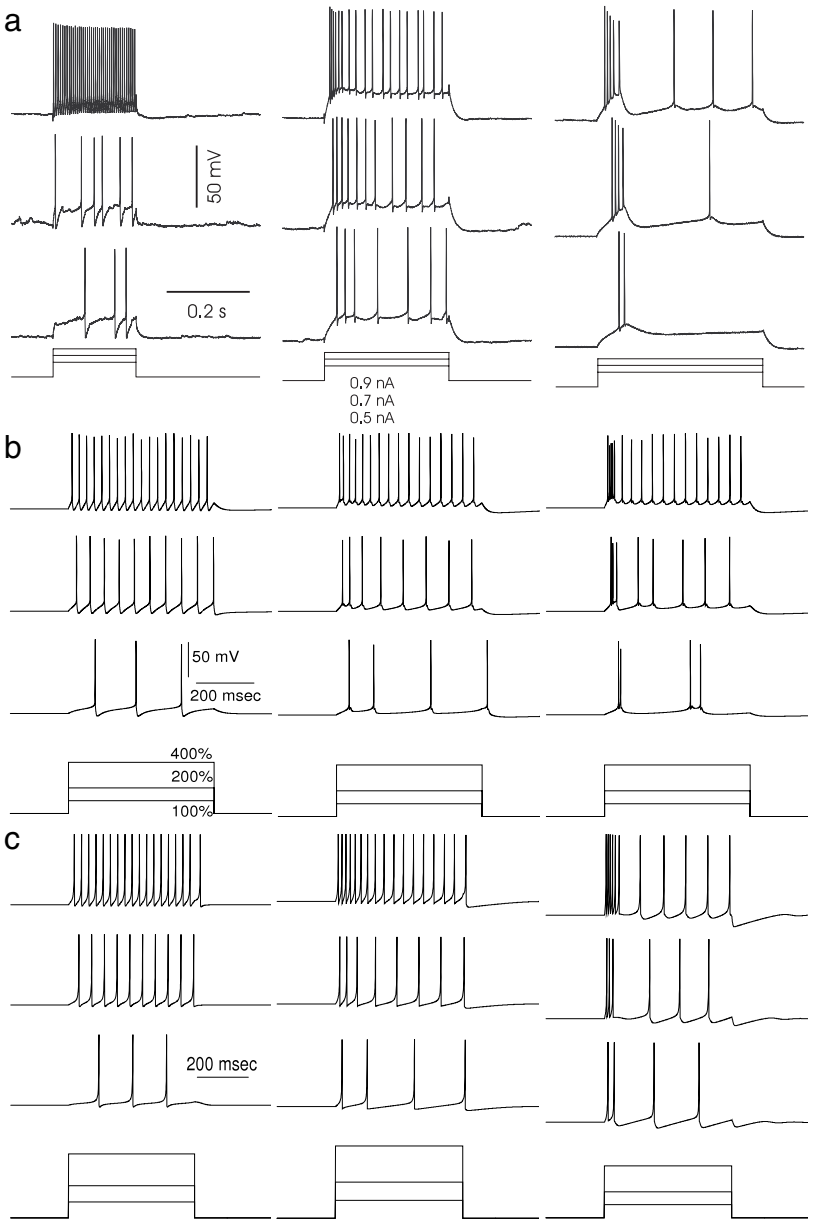

Fig. 72. Comparison of (a) *in vivo* data, (b) Hodgkin–Huxley models, and (c) map-based models of intrinsic firing patterns of cortical neurons. Left panels, fast-spiking (FS) neuron; middle panel, regular-spiking (RS) neuron; right panel, intrinsically-bursting (IB) neuron. The map-based model of the FS neuron, Eqs. (52), has $\alpha = 3.8$, $y^0 = 2.9$, $\beta^{hp} = 0.5$, $\gamma^{hp} = 0.6$, $g^{hp} = 0.1$, $\beta^e = 0.1$, and pulse amplitude $A = 0.016$ at 100%. The map-based model of the RS neuron follows Eqs. (51), with $\alpha = 3.65$, $\sigma = -0.94$, $\mu = 0.0005$, $\sigma^e = 1.0$, $\beta^e = 0.133$ and pulse amplitude $A = 0.03$ at 100%. Same equations for the IB neuron, with $\alpha = 4.1$, $\sigma = -1.036$, $\mu = 0.001$, $\sigma^e = 1.0$, $\beta^e = 0.1$ and $A = 0.01$ at 100%.
Source: From Rulkov et al. [53].

noisy, quiescent intervals. Switching between the two states at rates of the order of 1 Hz occurs synchronously in ensembles of cortical neurons. In Fig. 73 this regime is shown to be present in the lattice of Fig. 66: as the spiral waves of activity propagate, activated neurons go into a coordinated *up* state, which shows up in the local field potential.

In a similar vein, the Izhikevich model can be tuned to reproduce a staggering variety of neuronal behaviors, as revealed in Fig. 9 and described by Izhikevich [43]. The most comprehensive guide to modeling with Izhikevich neurons, and probably with any single kind of model, can be found in [180], where detailed discussions of parameter choices, model modifications and involved dynamic issues are given for RS, IB, FS and LTS neurons, but also for some other dozen cases including cortical, thalamic and brainstem classes. All this information was put to use in a mammoth model of the thalamo-cortical system [175] that can be seen as a extended version of the cortical model in [174]. It includes a million neurons belonging to 12 different classes, almost half a billion synapses, and short and long-term plasticity. A diagram of the microcircuit

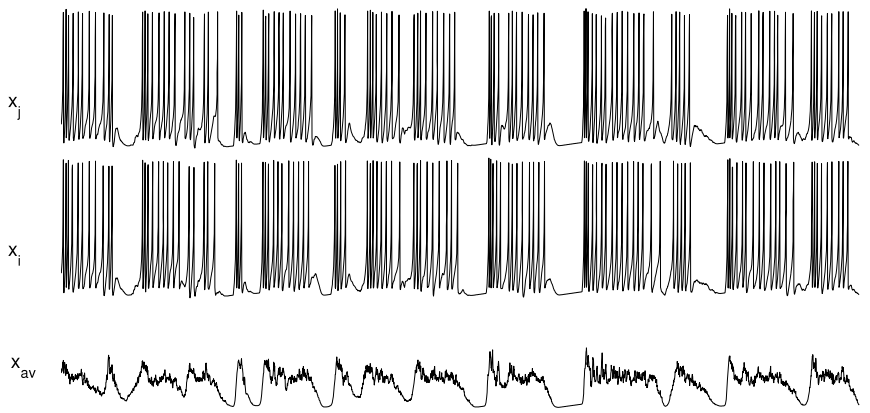

Fig. 73. Top and center traces, evolution in time of the x variables of two PY neurons in the center of a 128 × 128 lattice with the same parameters as in Fig. 68 except $g_{\text{PY–PY}} = 12$. States of irregular activity (*up* states) are separated by periods of hyperpolarized voltage values (*down* states). Bottom trace, average value of the x variables of the neurons in a 10 × 10 square at the center of the lattice, imitating the local field potential (LFP). The up and down states are clearly reflected in the LFP, indicating that the states are strongly correlated in all neurons. The traces are 4000 time steps long. Following Rulkov et al. [53].

architecture of the model is depicted in Fig. 74. All neurons have a somatic compartment and a number of dendritic compartments that depends on the number of synaptic inputs; however, both somatic and dendritic compartments are modeled with the Izhikevich equations, and the multicompartment neurons can be seen as electrically coupled assemblies of Izhikevich point neurons. The Izhikevich neurons are integrated with a submillisecond time step, in some cases with a semi-implicit Euler method for better stability, and therefore they do not exactly conform to Eq. (11). Anatomical DTI data were used to project and assign delays to cortico-cortical and thalamo-cortical connections. Several features of brain activity that had not been specifically built-in in the model emerged from simulations, including collective oscillations of local field potentials with rhythms in the alpha, beta and delta bands. Interestingly, the rhythms were different in different regions of cortex, even though they shared exactly the same microscopic circuits, pointing to a fundamental role of white matter in shaping local oscillations. The model, in a spirit similar to that of the Blue Brain project, is intended as a powerful workbench on which manifold simulated experiments can be designed; Izhikevich and Edelman [175] just provide a sample.

5.2. Modeling learning and behavior

A class of neuronal systems that typically tax computational resources to the maximum are those that implement learning tasks. Learning takes place in time scales that are usually orders of magnitude longer than electrical neuronal activity, and require large networks to accommodate significant sets of patterns or responses. Therefore, map-based neuron models are particularly well-suited for these modeling endeavors. Some studies address learning tasks from a purely dynamical or computational point of view; for example, Cazelles [181] shows how a network of chaotic Chialvo neurons can learn to synchronize to a pacemaker cell by tuning their parameters with an extended Kalman filter algorithm. Kumagai et al. [182] devised a method to store patterns of activation in networks of modified Nagumo-Sato neurons that can hardly be realized in a biological setting.

Biologically oriented efforts in modeling learning using map-based models are well exemplified by Izhikevich [183], where the author extends a previous network model [168] – described in Section 4.3 – to include a reward mechanism mimicking dopamine (DA) secretion [184]. This turns plasticity, beyond its homeostatic role, into an effective reinforcement learning mechanism [185]. In this setting, the STDP rule is not directly used to update synaptic conductances, but rather acts as an *eligibility trace* [186], and plastic effects take place only in the presence of DA. This can be implemented in the following way: for each synapse, an eligibility variable c_{ij} is updated continuously as

$$c^{ij}(n+1) = k_c c^{ij}(n) + \sum_{i,j} \text{STDP}(\Delta t_{i,j})\delta(t - t_{i,j}),$$

where $0 < k_c < 1$ is a slow decay constant, $t_{i,j}$ represents the later of either a pre or postsynaptic spike in the pair of neurons connected by the synapse, and $\text{STDP}(\Delta t)$ is the STDP rule function of Fig. 69 — with both positive and negative values. The synaptic conductances $g_c^{i,j}$ vary at a rate $c^{i,j}$ *modulated by the presence of dopamine*:

$$g_c^{i,j}(n+1) = S[g_c^{i,j}(n) + c^{i,j}(n) \cdot d(n)].$$

$S(x)$ is a clipping function that avoids both negative or excessively high values for the conductances, and $d(n)$ represents the extracellular concentration of DA, common to all neurons, which indicates the presence of a reward. The author shows how this simple scheme reinforces spike sequences that are systematically correlated with rewards, even if the reward comes several seconds (the scale being set by the eligibility trace time constant) after the spike sequence. In fact, if the release of

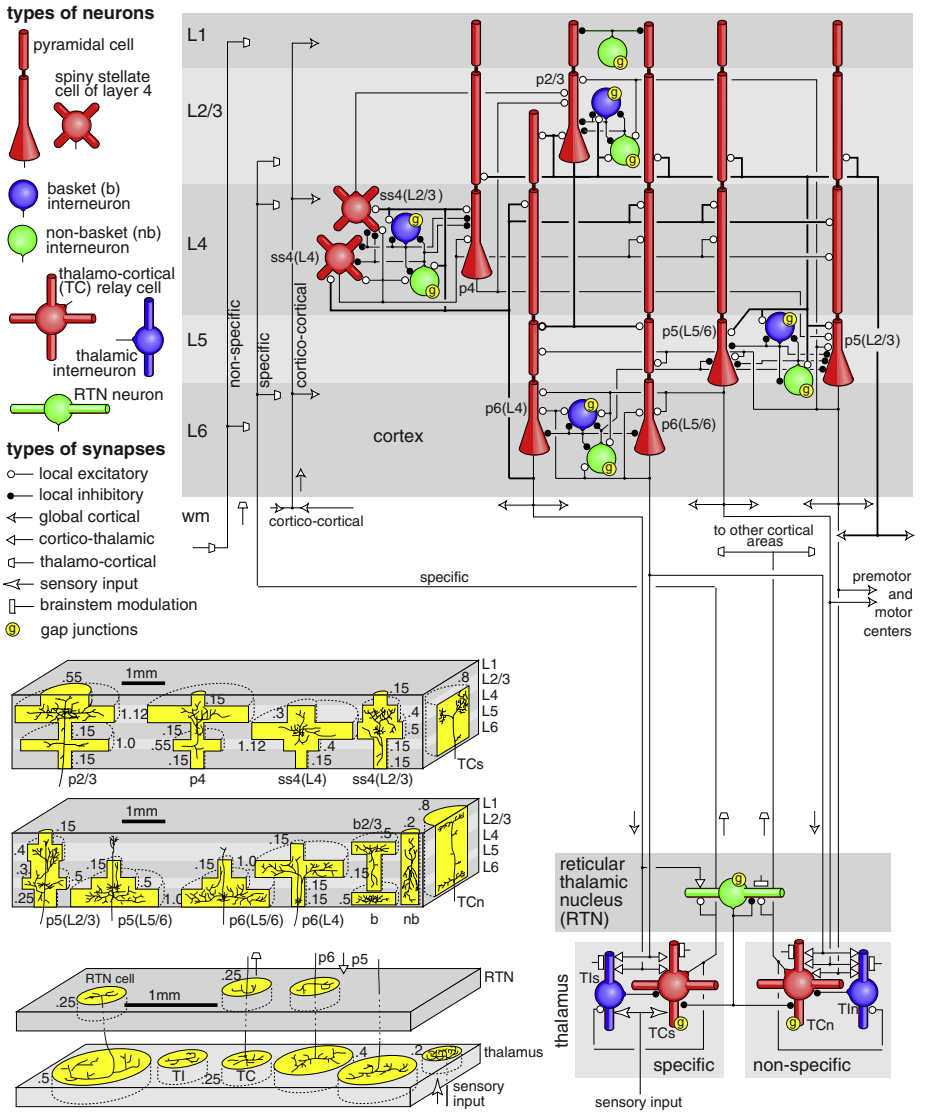

Fig. 74. Simplified diagram of the microcircuitry of a thalamo-cortical model built with Izhikevich neurons, indicating the types of neurons and synapses. Only major pathways are shown. Self-synapses denote synaptic connections within the populations. L1–L6 refer to cortical layers, wm stands for white-matter. Arrows indicate types and directions of projections. The lower-left diagram represents the extent of the axonal arborizations of each neuronal type, with their radii in millimeters; synapses exist onto neurons inside the corresponding radius.
Source: From supplementary information in Izhikevich and Edelman [175].

DA is coupled to the firing of certain neurons in the network (representing cortical neurons projecting to the dopaminergic neurons in the midbrain), and these in turn are reliably activated by a chain of assemblies of neurons, the anteriormost ensemble's synapses onto the midbrain-projecting neurons will be reinforced; this can be read as a shift from unconditional to conditional stimulus in the release of DA and is a prerequisite for implementing the temporal-difference (TD) reinforcement model that is hypothetically embodied in the dopamine reward system [187]. Lastly, the scheme can emulate instrumental conditioning [188] by coupling some neurons to output units whose actions determine the delivery of rewards.

A different kind of learning, which may be classified as *unsupervised* [189] because it does not include reward signals to label correct answers, has been modeled by Nowotny et al. [55,190,191]. Here the focus is on the odor recognition system of insects. Represented structures include the antennal lobe (AL), the mushroom body (MB) and the mushroom body lobes (LB). Odors are detected by receptor cells in the antennae that synapse upon neurons in the AL, where each odor gets represented by a spatio-temporal pattern of active neurons, called projection neurons (PN) [192]. PNs project via sparse excitatory synapses upon the much more numerous neurons in the MB [193] called intrinsic Kenyon cells (iKCs). The authors hypothesize that projections from the MB to the LB are plastic and self-organize to classify input patterns in the activity of the mutually inhibiting neurons of the LB, called extrinsic Kenyon cells (eKCs). Thus the AL–MB–LB system would classify odors in two stages: first a transformation from the AL to the MB, which separates the patterns in the PNs into sparse patterns

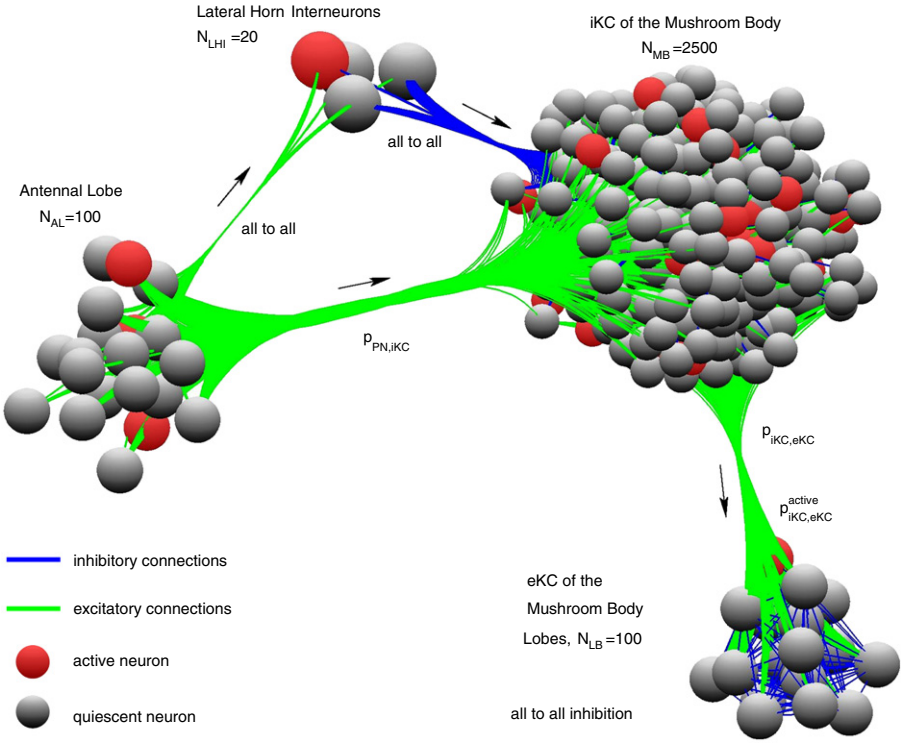

Fig. 75. Schematic, scaled 1:5, of antennal lobe and mushroom body model used to investigate odor recognition in insects. Active and quiescent neurons refer to activity during the 50 ms window following odor presentation in AL. STDP is implemented for synapses between the mushroom body and the mushroom body lobes. iKC and eKC stand for intrinsic and extrinsic Kenyon cells, PN for projection neurons. N represents number of neurons in each part of the model, $p_{\mathrm{PN,iKC}}$ and $p_{\mathrm{iKC,eKC}}$ probabilities of connection between pairs of neurons, $p^{\mathrm{active}}_{\mathrm{iKC,eKC}}$ probability of strong versus weak initial synaptic conductances. The lateral horn interneurons (LHIs) are included in some simulations to assess the effect of gain modulation on system performance.
Source: From Nowotny et al. [55].

in the iKCs, and then a classification of iKC activity patterns by eKCs by means of spike-timing-dependent plasticity and mutual inhibition between eKCs, the combination of which leads to self-organized, simple representations of odors suitable for association and memory. The full system is depicted in Fig. 75.

All neurons in the model except PNs are one-variable versions of the non-chaotic Rulkov model, with a frozen slow variable as in the FS neuron model of Eqs. (52) because no bursting or adaptation is intended. The model is dimensionalized and each iteration made to correspond to $\Delta t = 0.5$ ms. The model map is

$$v(t+\Delta t) = \begin{cases} v_{sp}\left(\dfrac{\alpha}{1-\frac{v(t)}{v_{sp}}-\frac{I_{\mathrm{syn}}(t)}{I_0}}+\gamma\right) & \text{if } v(t)\le 0, \\ v_{sp}(\alpha+\gamma) \quad \text{if } 0 < v(t) < v_{sp}(\alpha+\gamma), \\ -v_{sp} \quad \text{otherwise.} \end{cases} \tag{53}$$

Parameter values are $v_{sp} = 60$ mV, $\alpha = 3$, $\gamma = -2.468$ and $I_0 = 22.7$ nA. $I_{\mathrm{syn}}(t)$ is the total synaptic input to the neuron, and is calculated according to a chemical synaptic scheme similar to Eq. (48). The PNs in AL are modeled as mere voltage pulses from −60 mV to 50 mV with 1.5 ms duration when active in the input pattern; a finer exploration of the dynamics of PNs by means of Rulkov neurons can be found in [191]. As already mentioned, synapses from the MB to the LB are plastic and follow a triangular-shaped STDP rule. Connections between AL and MB and between MB and LB are created randomly for each PN-iKC or iKC-eKC pair with probabilities $p_{\mathrm{PN,iKC}} = 0.15$ and $p_{\mathrm{iKC,eKC}}$ ranging between 0.2 and 1 in different simulations. No lateral connections inside each module exist except for the *LB*, with all-to-all inhibitory connections.

Each odor is represented as a class of patterns of activation of 20 out of the 100 PNs. Each class has a basic pattern chosen randomly, and other members of the class are created by adding or eliminating a small number of neurons to or from the basic pattern. A normalized distance between 0 and 1 is defined to measure the similarity between the patterns; intra-class distances are close to zero while inter-class distances are close to one. The same distance is used for comparing resulting patterns of activity in MB and LB. The presentation of a pattern to the network consists in simultaneously activating the corresponding PN neurons, as shown in Fig. 75, and the response is registered as the set of neurons in the network that fire inside a 50 ms window. With the initial random connectivity, both the intra-class similarity and the inter-class dissimilarity degrade as the pattern is transmitted through MB to LB, as seen in the results of Fig. 76 marked as $\mathrm{LB}_{\mathrm{naive}}$. However, as

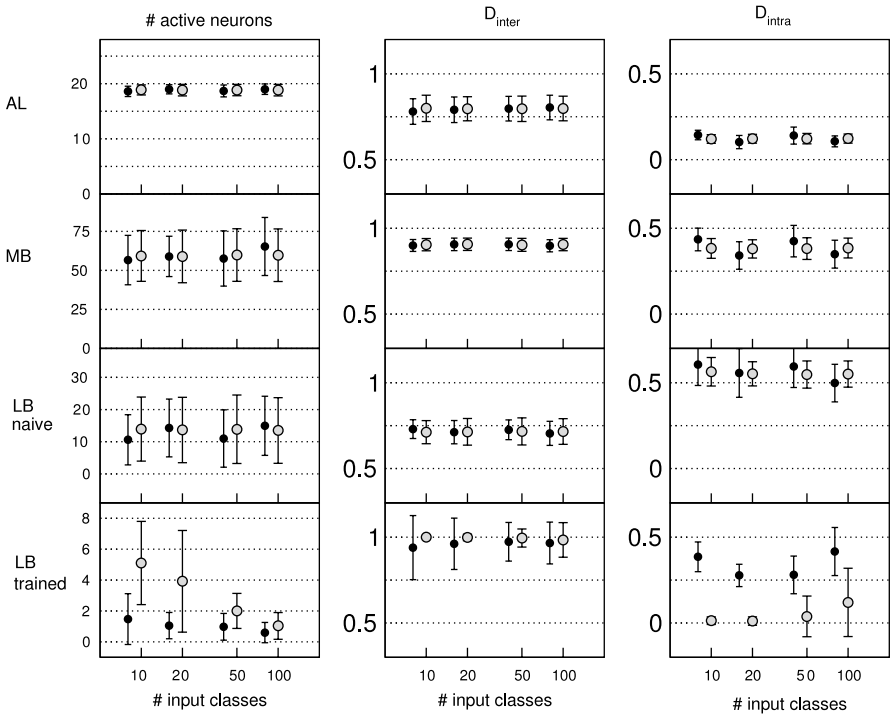

Fig. 76. Results of odor pattern classification in the three modules of the model depicted in Fig. 75, for different numbers of pattern classes. D_{inter}, average distance between patterns of different classes; D_{intra}, idem for patterns of the same class. LB_{naive} refers to the response in LB before training, LB_{trained} after training. White symbols represent the response for the classes used during training. Note that in the naive LB inter and intra-class distances become similar (between 0.5 and 0.7), while in the trained LB the inter-class distance is almost one and the intra-class distance for trained classes almost goes to zero, except when 100 classes are used. Also notice how increasing the number of classes decreases the number of neurons recruited by each pattern in LB: the code becomes spontaneously sparser. The black symbols show the response to inputs of a new class, not used for training. The clearly reduced activity and the large intra-class distance in the MB lobes for the new inputs show that the system classifies the new input as unknown rather than as a member of a known class.
Source: Simplified from Nowotny et al. [55].

more patterns of the same class and of different classes are presented, MB–LB synapses evolve, without any supervision, until representations in LB get sharper than the input (Fig. 76, results for $\text{LB}_{\text{trained}}$): intra-class distance in the trained LB gets very close to zero and inter-class distance very close to one. Of course, the performance degrades when the number of classes grows beyond the capacity of the system; the degradation is visible in the results for 100 pattern classes. However, the degradation is graceful in the sense that excess patterns, to a great extent, are not misclassified; the network responds to them with very low activity in LB. Thus excess patterns are not remembered by the system, rather than confused with previously stored ones.

Finally, it is of some interest to take a look at the evolution of the plastic synaptic conductances, displayed in Fig. 77(a). As in the homeostatic system of Fig. 70, STDP polarizes synaptic conductances. The strongest conductances carry the transformation of coding between MB and LB, and constitute a small fraction of the total connections, as shown in Fig. 77(b). This makes the system robust against limitations in the number of available MB–LB synapses. Results very similar to those of Fig. 76, which correspond with all-to-all connections between MB and LB ($p_{\text{iKC,eKC}} = 1$), are obtained with $p_{\text{iKC,eKC}}$ as low as 0.2.

An element of the insect olfactory pathway that is shown to have little impact on the performance of the classifying system implemented in Nowotny et al. [55] is the group of lateral horn inhibitory interneurons (LHIs) that can be seen in Fig. 75. Its role, which is to modulate the gain of the AL–MB connection by feed-forward inhibition of the iKCs, was very limited in the model because the input from AL was extremely rigid: there was no room for variation of the intensity of the olfactory patterns presented. However, it is known from experiments that the activity of PNs is highly sensitive to the concentration of odorants, particularly in terms of synchrony [194]. A high degree of synchrony of the PNs should raise the firing probability of the postsynaptic iKCs and would compromise the sparseness of coding in MB, but this is not found to be the case in the experiments. Assisi et al. [195] propose that the role of the LHIs is precisely to preserve the sparseness of the code in spite of increased synchrony across thousand-fold changes in odor concentration. To support the hypothesis, a model is built that includes AL, LH and MB, very much as in [55]. However, since in this case the behavior of PNs is critical to the model, AL is modeled as an ensemble of 400 relatively complex Hodgkin–Huxley type neurons. LH and MB, on the other hand, are made up of 100 and 15 000 Rulkov neurons, so that complete simulations can be performed in reasonable time. The model succeeds in showing that feed-forward inhibition by LHIs limits the integration window of the iKCs when odor

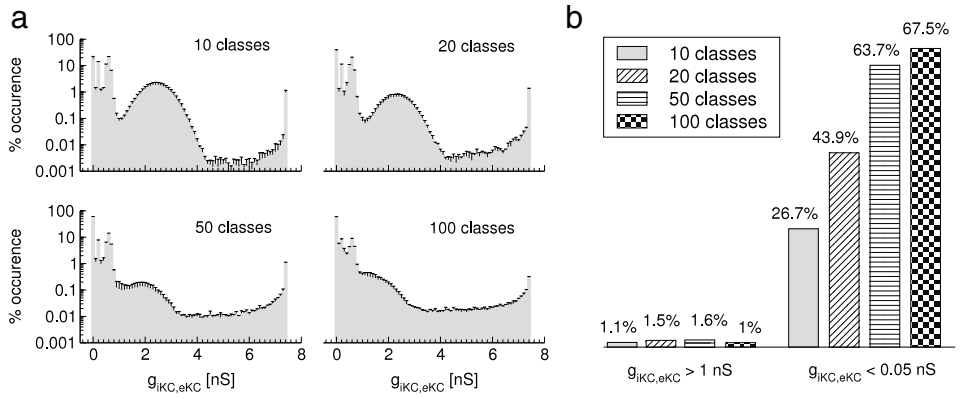

Fig. 77. (a) Distribution of synaptic conductances from MB to LB after training, for different numbers of pattern classes. In all cases most of the synapses are depressed, while a small but significant number of synapses are strengthened to the maximal conductance ($g_{max} = 7.5$ nS). (b) Percentages of strong and weak synapses. The more classes that need to be formed, the sparser the coding becomes, with a higher number of very weak synapses.
Source: From Nowotny et al. [55].

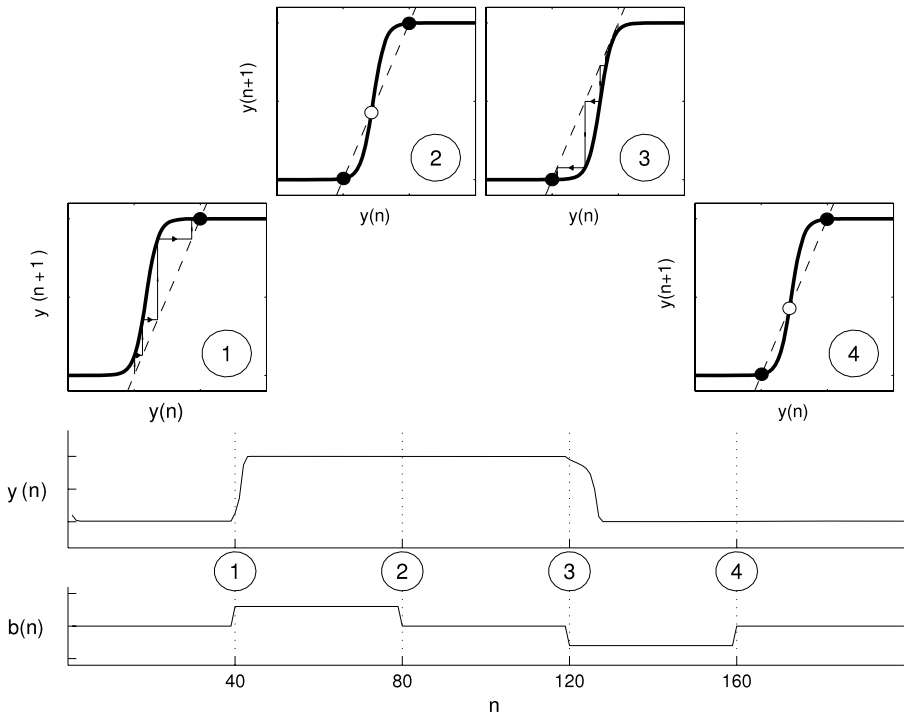

Fig. 78. Return maps and response to pulsed inputs of the bistable unit proposed by Nakahara and Doya [196], Eq. (54). The insets represent the first return maps and a cobweb of the orbit around the time steps where the input switches. Parameter $a = 11$, and b switches from $b_0 = -5$ to $b_{up} = -2$ and $b_{down} = -8$.

concentration is high, compensating for the increased synchrony of PNs. This hybrid model is a beautiful example of how the virtues of different types of models can be exploited to combine physiological detail with computational convenience.

Other studies do not focus so much in the plastic processes that shape the neural networks towards a given behavioral goal, but on the optimal configurations that, possibly emerging through a combination of evolutionary adaptation and learning, are the substrate of animal behavior. Such is the case of Nakahara and Doya [196], where a toy model of working memory is built with map-based units closely related to the Aihara model, and put to work in a simulated environment to investigate the parameters that optimize foraging behavior. The unit model is

$$y(n+1) = F[ay(n) + b], \tag{54}$$

where $F(x)$ is the sigmoidal function in Eqs. (24) with $\sigma = 1$. The absence of the linear terms of the Aihara model operates a sort of rotation in the return map and transforms the spiking neuron into a bistable switch; the return map is depicted in Fig. 78 for different values of b, which can be regarded as a bias or excitation parameter. By increasing or decreasing b, the

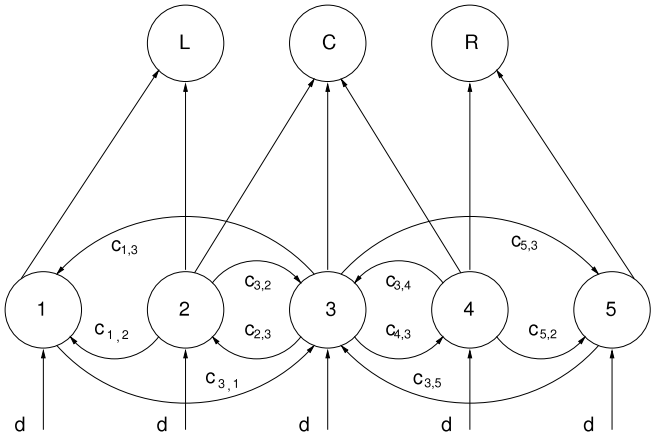

Fig. 79. The network of sensory (1–5) and motor (L, C, R) units of the creatures proposed by Nakahara and Doya [196]. Sensory units follow Eqs. (55), and their coupling coefficients $c_{i,j}$ are constrained in simulations to be symmetric with respect to the longitudinal axis. The motor units simply weigh their inputs and their output codes the probability of turning 45° to the left (L), stepping forward (C) or turning 45° to the right (R).

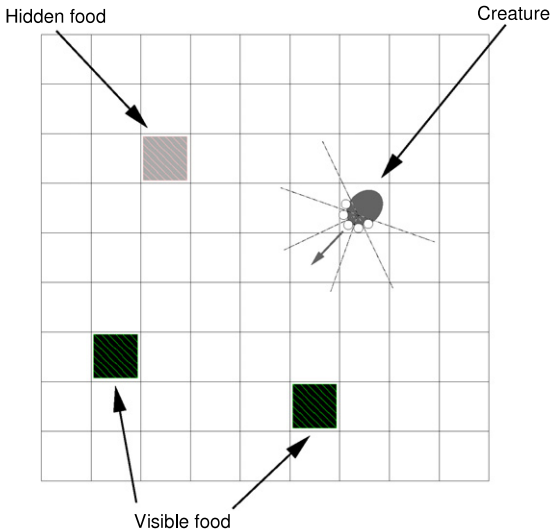

Fig. 80. The foraging task in a grid-like world. Each of the 5 sensory units [Eqs. (55)] receives visual input from a 45° sector of the world. Food items are at fixed grid locations, but randomly switch from visible to hidden following a Markov process. At each time step, the creature decides whether to move one step forward or turn 45° left or right, depending on the command of its three motor units. Following Nakahara and Doya [196].

return map shifts leftwards or rightwards, the upper or lower stable state can be destabilized through a saddle–node bifurcation, and switching may take place. The substrate for memory lies in hysteresis: the system may switch upon an input pulse and not return to its original state when the pulse ends, as seen at event 2 of Fig. 78. The unit does not necessarily represent a single neuron; it might represent a neural network with bistability, such as, for example, a group of coupled inhibitory neurons (see Fig. 62). Once again, the map-based model is an abstraction of the fundamental properties of the system.

A sensory network is built with five of the bistable units and embodied in a toy creature with three possible motor outputs. The network equations are

$$y_i(n+1) = F\left[ay_i(n) + b + \sum_{j\neq i} c_{i,j}y_j(n) + d\,I_{\mathrm{ext},i}(n)\right] \tag{55}$$

for $i = 1\ldots5$. The coefficients $c_{i,j}$ represent coupling to other units, and d is the sensitivity to external stimulation. In this context, parameter a of the isolated unit can also be regarded as self-coupling. The network structure is depicted in Fig. 79. The output of the sensory units is weighed in three motor units, which decide whether to turn 45° left (L motor unit, innervated by the two leftmost sensory units), step forward (C motor unit, innervated by the three central sensory units), or turn 45° right (R motor unit, innervated by the two rightmost sensory units).

The creature seeks food in a grid-like world [197], represented in Fig. 80. Food is distributed at random in the grid, and at each time step each food item can switch between a visible and a hidden state following a Markov process.

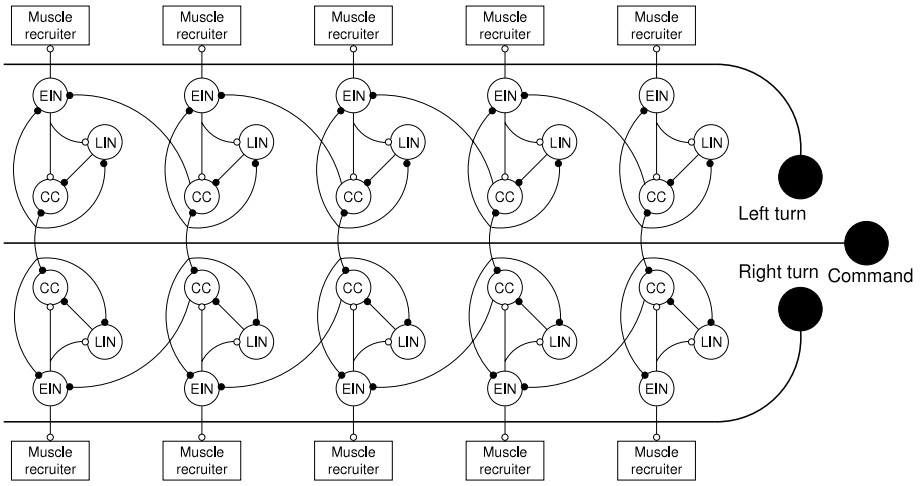

Fig. 81. Swimming control circuit of a robot lamprey. Five segments are represented. EIN, excitatory interneuron; LIN, lateral interneuron; CC, contralateral caudal projecting neuron. Empty circles are excitatory, filled circles inhibitory synapses.
Source: Adapted from Ayers and Rulkov [200].

This setup, when the probability for an item to remain hidden for long intervals is high, especially favors creatures capable of maintaining memory traces of previously visible food items. The external stimulation $I_{\text{ext},i}$ to each sensory unit depends on the existence of visible food inside a corresponding 45° sector of the grid centered in the creature, as shown in the figure. To be precise, $I_{\text{ext},i} = \sum_j 1/r_j$, where r_j is the distance to each visible food item within the sector. The performance of a creature is measured by the average number of food items it is able to reach within a given time.

It is easy to understand that the network in Fig. 79 has been designed to perform the required task: the presence of food to the left of the creature, for example, will raise (d being positive) the bias of sensory units 1 or 2 and with it the probability of turning left; after that, food will be in front of the creature and the C motor unit will be most activated, and so on. However, the best performance will only be obtained for optimal choices of the parameters, particularly of the connection weights $c_{i,j}$, and these in turn depend on the world parameters. An evolutionary algorithm [198] is implemented to optimize performance, and the top performing creatures' parameters are examined in relation to world parameters. The outcome is interesting: top scorers implement a working memory by means of inhibitory connections ($c_{i,j} < 0$) between sensory units and, particularly in harsh environments (where food items remain invisible for long intervals), are biased *close to the saddle–node bifurcation*. This makes the units most sensitive to stimulation and strikes the best balance between robustness and flexibility of the memory traces. Proximity of bifurcation points as a condition for richer behavior and wider computational capabilities seems to be a common feature of neuronal dynamics [199].

Map-based neurons can also be used to control not virtual but real creatures. Ayers and Rulkov [200], Ayers et al. [201] describe control systems of ambulatory and swimming robots implemented with Rulkov neurons. At the core of these systems are small networks of neurons that implement central pattern generators (CPGs), as described in Section 4.3. Fig. 81 represents the model for the control of swimming in an undulatory robot based on the sea lamprey. The robot is segmented and has bilateral symmetry. In each segment, a CPG consisting of six coupled neurons, three on each side of the body, ensures that muscle actuators are engaged rhythmically to produce undulations. To this end, the left and right halves of each CPG must be in phase opposition, and the CPG in each segment must have a certain phase delay with respect to the previous one. The CPGs are activated by a command neuron in the head, which sends excitatory synapses to all neurons to stimulate bursting. Turning is controlled by two other command neurons that modulate the strength of the synapses onto actuator circuits on each side of the body.

Fig. 82 shows one segment CPG in action. Notice how the EIN neurons, which activate the muscles on each side, burst in phase opposition. This ensures that one side is released while the other contracts, producing the curvature necessary for undulatory movements. As explained in Section 4.3, the eigenvector associated with the complex dominant eigenvalue of the network graph of Fig. 82 predicts the bursting pattern, even though this network is not balanced. The parameters of each neuron in the CPG, and the strengths of the synapses, can be fine-tuned to modify the ordering, period and duty cycle of the bursts. In particular, the strength of the inhibitory synapses from the CC neurons in each segment to the EIN neurons in the next one (not included in Fig. 82) determines the phase relation between consecutive segments on which swimming direction and speed mostly depends. Indeed the whole control system can be implemented with map-based Rulkov neurons, resulting in a fast, easy to implement biomimetic controller.

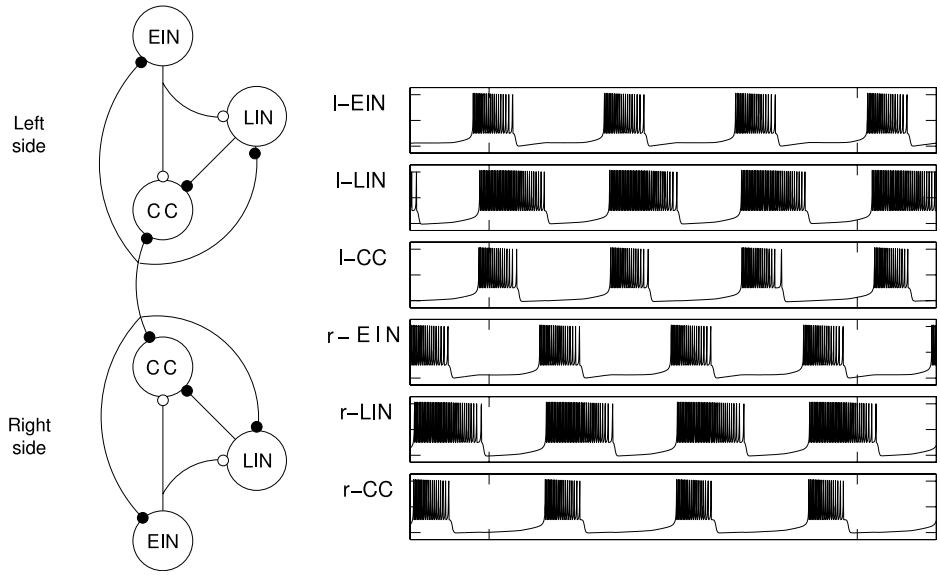

Fig. 82. The CPG of one segment of the circuit of Fig. 81, and the rhythmic pattern it generates. The contralateral inhibitory connections sent by the CC neurons ensure that the three neurons on each side burst in phase opposition. Non-chaotic Rulkov neurons with $\alpha = 6$, $\mu = 0.001$ and $\sigma = 0$ have been used; coupling is linear through the slow variable.

5.3. Modeling cognitive processes

Finally, an example of modeling of higher cognitive powers with map-based models can be found in [202], which offers a so-called global workspace model as a substrate for nothing less than consciousness [203]. The idea is that the physical substrate of consciousness is a number of ensembles of neurons distributed across the entire brain, interwired by long-range connections, each ensemble being part or connected locally to several cortical columns. This substrate is called a global workspace because the activity induced in one ensemble of the substrate is broadcast, by means of the long-range connections, across all the other ensembles, reverberating globally. Cortical columns, or groups thereof, performing unconscious processing, compete to gain access to their neighboring workspace ensembles and, through them, to the global workspace. Processes that manage to access the workspace become conscious. An implementation of such workspace, as substrate of this cognitive model, should be able to sustain patterns of activation over several tens of milliseconds; disseminate them throughout cortex, preserving the information in their spatio-temporal structure; be sensitive to new patterns of activation, allowing for consecutive replacements of patterns; and implement the competitive interaction between cortical modules to gain access to it. A schematic of the simple architecture proposed by Shanahan [202] to this end is displayed in Fig. 83. Five workspace ensembles and three cortical columns are included; both kinds of modules consist of excitatory and inhibitory pools of Izhikevich neurons, following the example of Izhikevich [43], and coupling is linear and limited to the instant of the presynaptic spike; delays are also included. The workspace ensembles are interconnected in such a way that activity in one node quickly spreads into the others, effecting a form of broadcast; the cortical columns can influence the pattern in the workspace and vice versa. Three columns are enough to demonstrate the basic mechanism proposed in the study; C1 has access to workspace ensemble W1, while C2 and C3 compete for access to W2.

The excitatory connections between workspace modules and between the modules and the columns are rigidly structured in a one-to-one fashion. Intra-columnar connections, on the other hand, are all-to-all, as are the inhibitory connections from the W^- pools of each workspace module to the other modules. In order to differentiate the information carried by the different columns, they are trained separately from the workspace via STDP to respond to stimulation at certain neurons of their input pools with activity in certain neurons of their output pools, different for each column. The one-to-one connections to the workspace make it possible to recognize what column has gained access at any given moment.

A demonstration of the model is shown in Fig. 84. To initiate activity, neurons 1–64 of W1 are stimulated at $t = 20$ ms. This activity quickly propagates to the other nodes of the workspace (it can also be seen in W2 in the figure) and reverberates globally for more than 100 ms thanks to the recurrent connections. The activity in W1 stimulates the input pool of C1 that has been trained to respond precisely to that pattern; thus, around $t = 60$ ms the output pool of C1 becomes active in neurons 65–128, and this pattern is transmitted to W1 and broadcast from there to the whole workspace and to the input pools of all columns. The all-to-all inhibitory connections in the workspace terminate the previous pattern. The new pattern, in turn, is detected by columns C2 and C3, because of their training, and both try simultaneously to access the workspace through different output sets: this is obvious in C2, but notice also the timid spikes in the output pool of C3 around $t = 130$ ms. However, only one of the two columns, C2 in the example, prevails, due to the lateral inhibition between them. Interestingly,

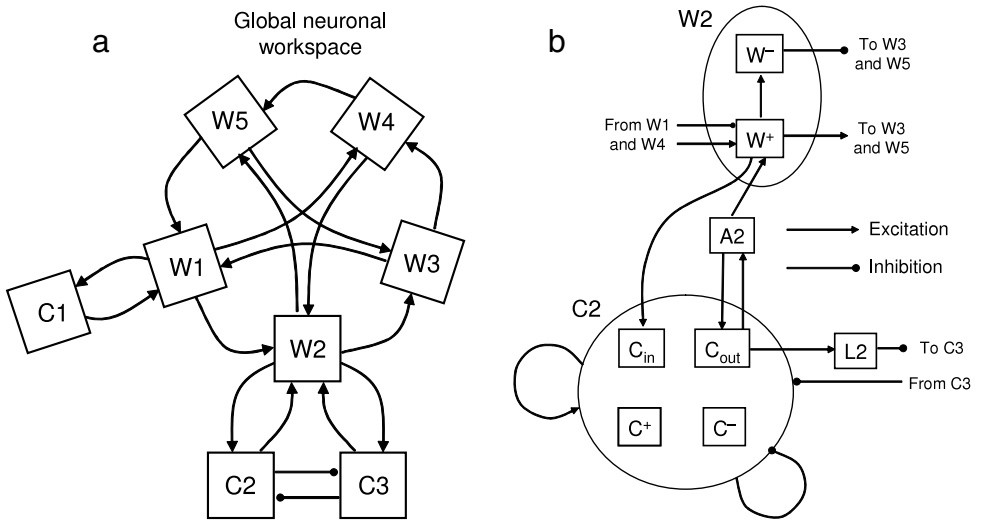

Fig. 83. (a) Model of global workspace implemented with Izhikevich neurons by Shanahan [202]. W1–W5 are workspace modules, while C1–C3 represent cortical columns, most relevant for the model are the lateral, inhibitory connections between C2 and C3 that support the competition for access to their neighboring workspace module, W2. (b) Detail of the modules W2 and C2 in (a). L2, C^- and W^- are pools of inhibitory neurons, all others are excitatory. C2 consists of 1024 neurons distributed in an input pool (C_{in}, 256 neurons), an output pool (C_{out}, 256 neurons), an intrinsic excitatory pool (C^+, 320 neurons) and an intrinsic inhibitory pool (C^-, 192 neurons); connections are all-to-all between and inside the four pools. C_{out} projects on W^+ via an access buffer (A2), while W^+ projects back directly to C_{in}. All the C_{out}–A2–W^+–C_{in} connections are one-to-one; A2, W^+ and W^- have 256 neurons each. Lateral inhibition, both between columns through L2 and between workspace areas through W^-, is always all-to-all.
Source: From Shanahan [202].

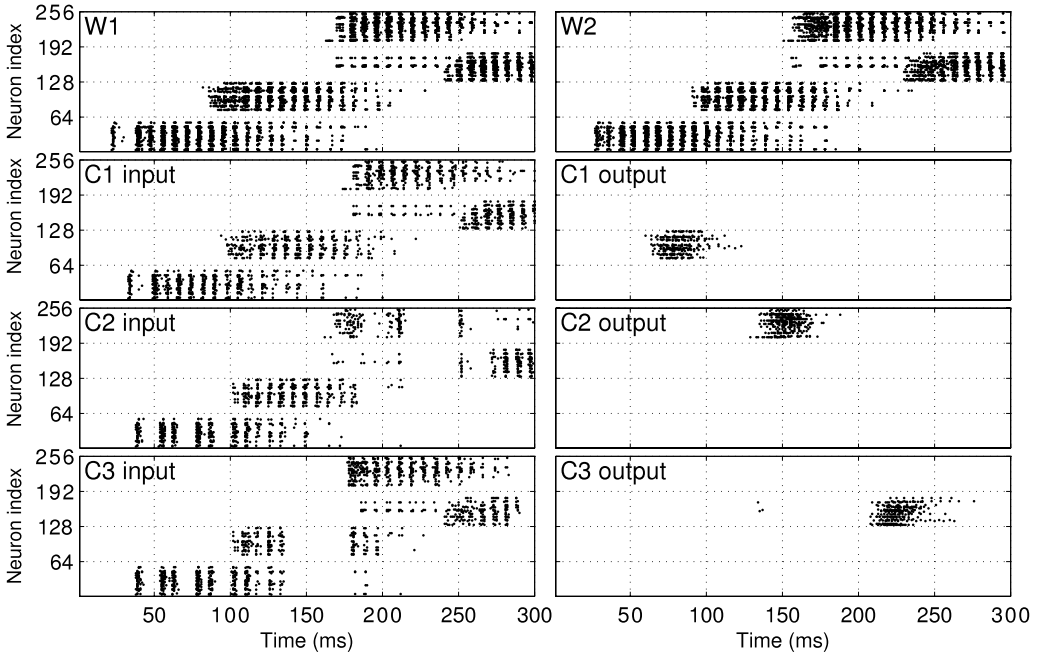

Fig. 84. The global workspace model at work. Neuron numbers 1–256 in the input and output pools of columns C1, C2 and C3 have one-to-one incoming and outgoing synapses, respectively, from and to neurons 1–256 of the workspace modules they connect to (W1 for C1 and W2 for C2 and C3). C1 has been trained to respond to stimulation in neurons 1–64 of its input pool by activating neurons 65–128 of its output, while columns C2 and C3 both respond to 65–128 input stimulation, with 193–256 activity in the case of C2 and 129–192 activity in the case of C3. Activity begins at $t = 20$ ms by external excitation of neurons 1–64 of W1; from that point on, patterns in W1 and W2 reveal how exclusive access to the workspace is gained sequentially by columns C1, C2 and C3, in that order. Simulations made with code from [202].

this victory is only temporary, because lingering activity of neurons 65–128 of the workspace stimulates C3 to try to access it again beginning at $t = 210$ ms, which it succeeds in doing around $t = 240$ ms. The order of access, C2 before C3, is very sensitive to initial conditions.

Table 1
Main classes of discrete neuron models found in the literature. Refer to Section 2 for details.

Model reference	Equations	Variables	Abstr. level	Remarks
Izhikevich [44]	$v(t+1) = F[v(t), I - u(t)]$ $u(t+1) = \begin{cases} u(t) + a[bv(t) - u(t)]; & v(t) < 30 \\ u(t) + d; & v(t) \geq 30 \end{cases}$ $F[v, I] = \begin{cases} \min(0.04v^2 + 6v + 140 + I, 30); & v < 30 \\ c; & v \geq 30 \end{cases}$	v, membrane voltage in mV u, slow recovery variable.	Low	Discretization of an ODE model. t is the discretized time
Rulkov models	$x(n+1) = F[x(n), y(n) + I]$ $y(n+1) = y(n) - \mu[x(n) - \sigma] \quad (\mu \ll 1)$	x, spiking activity. y, slow recovery variable. I and σ, external inputs.		
Rulkov [50]	$F[x, y] = \begin{cases} \alpha(1-x)^{-1} + y; & x \leq 0 \\ \alpha + y; & 0 < x \leq y + \alpha \\ -1; & x \geq y + \alpha \end{cases}$		Low	Spiking and bursting. Subcritical Neimark–Sacker bifurcation.
Shilnikov and Rulkov [52]	$F[x, y] = \begin{cases} \frac{\alpha^2}{4} - \alpha + y; & -1 - \frac{\alpha}{2} \leq x \leq 0 \\ \alpha x + (x+1)^2; & 0 < x \leq y + \alpha \\ 1 + y; & x \geq y + \alpha \\ -1; & x \geq 1 + y \end{cases}$		Low	Supercritical Neimark–Sacker bifurcation. Sustained subthreshold oscillations.
Rulkov [49]	$F[x, y] = \frac{\alpha}{1+x^2} + y$		Medium	Chaotic bursts
Courbage et al. [36]	$x(n+1) = x(n) + F[x(n)] - y(n) - \beta H[x(n) - d]$ $y(n+1) = y(n) + \epsilon[x(n) - J] \quad (\epsilon \ll 1)$	x, spiking activity. y, slow recovery variable.	Medium	Lorenz-type dynamics for x
Chialvo [35]	$x(n+1) = x^2(n)\exp(y(n) - x(n)) + I$ $y(n+1) = ay(n) - bx(n) + c$	x, spiking activity,y,non-slow recovery variable	Medium	Model of excitability
1D bursters [181,38]	Discontinuous piecewise-linear maps.	x represents spiking activity.	High	Lack of separate control of spike and burst dynamics.
Caianiello [27], Nagumo and Sato [28]	$x(n+1) = H\left[S(n) - \alpha \sum_{j=0}^{n} b^{-j} x(n-j) - \theta\right]$	x is the *state* of the neuron. S is external input.	High	Hard threshold. Inspired in the McCulloch–Pitts model. Non-chaotic.
Aihara et al. [29]	$y(n+1) = ky(n) - a(n) - F[y(n)]$, $F(y) = (1 + e^{-y/\sigma})^{-1}$	y is the *state* of the neuron. a is external input	High	Soft threshold. Chaotic
Netlet models [75,73,39]	$\alpha(n+1) = [1 - \alpha(n)]P[\alpha(n)]$	α is the average activity of neurons in the netlet.	Very high	Hysteresis. Only stable orbits with absolute refractoriness.

Thus a spiking model has been built that reproduces the dynamic properties required by global workspace theory. It extends previous models [204] to include the dynamic two-way interaction between workspace and columns, and, by using map-based neurons, allows intensive exploration and enlargement to assess its computational properties.

6. Summary and conclusion

Table 1 summarizes the map-based models described in this review. They are ordered by increasing level of abstraction: at the lower end are the single-neuron models with a variable that can be translated into actual membrane voltage; here the frontier between map-based and continuous-time models becomes fuzzy, as the latter turn into the former for numerical integration. At an intermediate level we find models that, while retaining the basic features of two-dimensional IF neurons, lack continuous-time counterparts, because they capture a particular dynamic property by means of a suitable mapping: irregular bursting, in the case of the chaotic Rulkov or the Courbage–Nekrorkin–Vdovin model; excitability, in the Chialvo model. At the high-abstraction end, models just attend to the presence or absence of spikes, or the average activity of an entire population. The appropriate level of abstraction, and the right choice of model, depend on the amount of information we have, and the generality of the question we wish to address. While there is no universal recipe for this, it is helpful to bear in mind the merits common to all map-based models:

- Map-based models are very efficient computationally. If action potential duration and shape are not relevant to a particular modeling task, the threshold and reset mechanism shared – with variants – by all map-based models saves an order of magnitude of integration time, while subthreshold dynamics in those that are conductance-inspired is integrated with a generous time step. A direct comparison of the number of floating point operations required to simulate a second of activity of an Izhikevich versus a Hodgkin–Huxley model gives a rough ratio of 1 to 100 [205]. Naturally, when map-based models are viewed as explicit numerical integrations of ODE-based counterparts, misgivings emerge as to the accuracy or stability of the coarse discretization. However, once the map-based equations have been established, the model should be evaluated on its own merits and faults, analyzed with the rich array of tools available for map dynamics, and compared to experiments as any other model would be. In a sense, as far as numerical simulation is concerned, ODE-models may

be regarded as less transparent than map-based ones, in that the necessary discretization is usually not contemplated in their analysis.

- Map-based models are simple and flexible. The two-dimensional spiking-bursting models that have taken up the greater part of this review span a whole zoo of different neuronal types with just a few parameters. The models we have reviewed are lean, compact abstractions of dynamical properties, and shed light over the mechanisms that give rise to neuronal phenomena ranging from chaotic spike trains to synchronized oscillations.
- Map-based models are backed by specific mathematical methods and paradigms, bringing with them points of view and strategies that expand the modeler's toolbox. A Poincaré section of an ODE-based spiking model may result in a map resembling a Nagumo–Sato neuron; chaotic regimes in a network of neurons can be characterized with entropy measures developed for coupled map lattices; symbolic dynamics can help understand the complexity of the spike trains generated by a given model.

Most of the map-based neuron models we have reviewed have been around for just a few years, and they are only beginning to meet wide recognition as powerful tools for the neuroscientist. With this review we have tried to convey to a wide audience the idea that map-based neuron models belong in the toolbox of the computational neuroscientist as much as any other kind of model. We hope it will be useful in guiding the difficult task of building meaningful models of neuronal systems.

Acknowledgements

We appreciate the fruitful comments and advice we have received from numerous colleagues during the writing of this manuscript. Among them we would like to mention Hongjun Cao, Ricardo Viana, Nikolai Rulkov, Michail Rabinovich, Maurice Courbage, Vladimir Nekorkin, Kazuyuki Aihara, Jie Zhang, Jason Gallas, Jorge Duarte, Hugues Berry, Bernard Cazelles, and Bruno Cessac. The authors acknowledge financial support from the Spanish Ministry of Science and Technology under Project Number BFM2003-03081 (BI and MAFS), from the Spanish Ministry of Education and Science under Project Numbers FIS2008-04120 (JMC) and FIS2006-08525 (BI and MAFS), from the Spanish Ministry of Science and Innovation under Project Number FIS2009-09898 (MAFS), and from the Fundación Ramón Areces (BI). MAFS acknowledges the hospitality of the Beijing Jiaotong University under the "Key Invitation Program for Top-Level Experts" of the "State Administration of Foreign Experts Affairs" of China.

References

[1] C. Koch, I. Segev, Methods in Neuronal Modeling: From Synapses to Networks, MIT Press, Cambridge, MA, 1989.
[2] W. Gerstner, W.M. Kistler, Spiking Neuron Models, Cambridge University Press, New York, NY, 1999.
[3] P. Dayan, L.F. Abbott, Theoretical Neuroscience: Computational and Mathematical Modeling of Neural Systems, MIT Press, Cambridge, MA, 2001.
[4] M.A. Arbib, The Handbook of Brain Theory and Neural Networks, second edition, MIT Press, Cambridge, MA, 2003.
[5] M.I. Rabinovich, P. Varona, A.I. Selverston, H.D.I. Abarbanel, Dynamical principles in neuroscience, Rev. Modern Phys. 78 (2006) 1213–1265.
[6] A.L. Hodgkin, A.F. Huxley, A quantitative description of membrane current and its application to conduction and excitation in nerve, J. Physiol. 117 (1952) 500–544.
[7] K. Ikeda, H. Daido, Optical turbulence: chaotic behavior of transmitted light from a ring cavity, Phys. Rev. Lett. 45 (1980) 709–712.
[8] T. Kai, K. Tomita, Statistical mechanics of deterministic chaos. The case of one-dimensional discrete process, Progr. Theoret. Phys. 64 (1980) 1532–1550.
[9] H. Fujisaka, Theory of diffusion and intermittency in chaotic systems, Progr. Theoret. Phys. 71 (1984) 513–523.
[10] K. Kaneko, Theory and Applications of Coupled Map Lattices, Wiley, New York, NY, 1993.
[11] K. Kaneko, I. Tsuda, Complex Systems: Chaos and Beyond. A Constructive Approach with Applications in Life Sciences, Springer, Berlin, Heidelberg, 2001.
[12] S. Haykin, Neural Networks: A Comprehensive Foundation, second edition, Prentice Hall, Upper Saddle River, NJ, 1998.
[13] G.A. Ascoli, Mobilizing the base of neuroscience data: the case of neuronal morphologies, Nat. Rev. Neurosci. 7 (2006) 318–324.
[14] K.L. Briggman, W. Denk, Towards neural circuit reconstruction with volume electron microscopy techniques, Curr. Opin. Neurobiol. 16 (2006) 562–570.
[15] H.C. Lai, L.Y. Jan, The distribution and targeting of neuronal voltage-gated ion channels, Nat. Rev. Neurosci. 7 (2006) 548–562.
[16] B. Sakmann, E. Neher, Single-channel Recording, second edition, Plenum Press, New York, NY, 1995.
[17] N.T. Carnevale, M.L. Hines, The NEURON Book, Cambridge University Press, New York, NY, 2006.
[18] J.M. Bower, D. Beeman, The Book of GENESIS: Exploring Realistic Neural Models with the GEneral NEural SImulation System, second edition, Springer, New York, NY, 1998.
[19] M. Bazhenov, I. Timofeev, M. Steriade, T.J. Sejnowski, Model of thalamocortical slow-wave sleep oscillations and transitions to activated states, J. Neurosci. 22 (2002) 8691–8704.
[20] A. Destexhe, D. Contreras, M. Steriade, Cortically induced coherence of a thalamic-generated oscillation, Neuroscience 92 (1999) 427–443.
[21] D.H. Terman, E.M. Izhikevich, State space, Scholarpedia 3 (2008) 1924.
[22] J. Rinzel, A formal classification of bursting mechanisms in excitable systems, in: A.M. Gleason (Ed.), Proceedings of the International Congress of Mathematics, AMS, Providence, RI, 1987, pp. 1578–1593.
[23] S. Wiggins, Introduction to Applied Nonlinear Dynamical Systems and Chaos, in: Texts in Applied Mathematics, vol.2, Springer, New York, NY, 1990.
[24] R. Brette, W. Gerstner, Adaptive exponential integrate-and-fire model as an effective description of neuronal activity, J. Neurophysiol. 94 (2005) 3637–3642.
[25] R. Jolivet, A. Rauch, H.R. Luscher, W. Gerstner, Predicting spike timing of neocortical pyramidal neurons by simple threshold models, J. Comput. Neurosci. 21 (2006) 35–49.
[26] W.S. Mcculloch, W.H. Pitts, A logical calculus of the ideas immanent in nervous activity, Bull. Math. Biophys. 5 (1943) 115–133.
[27] E.R. Caianiello, Outline of a theory of thought-processes and thinking machines, J. Theoret. Biol. 1 (1961) 204–235.
[28] J. Nagumo, S. Sato, On a response characteristic of a mathematical neuron model, Kybernetik 10 (1972) 155–164.
[29] K. Aihara, T. Takabe, M. Toyoda, Chaotic neural networks, Phys. Lett. A 144 (1990) 333–340.

[30] G.S. Medvedev, Reduction of a model of an excitable cell to a one-dimensional map, Physica D 202 (2005) 37–59.
[31] J. Touboul, R. Brette, Spiking dynamics of bidimensional integrate-and-fire neurons, SIAM J. Appl. Dyn. Syst. 8 (2009) 1462–1506.
[32] D. Hansel, G. Mato, C. Meunier, L. Neltner, On numerical simulations of integrate-and-fire neural networks, Neural Comput. 10 (1998) 467–483.
[33] S.H. Strogatz, Nonlinear Dynamics and Chaos: With Applications to Physics, Biology, Chemistry and Engineering, Addison-Wesley, Reading, MA, 1994.
[34] K. Alligood, T. Sauer, J.A. Yorke, CHAOS: An Introduction to Dynamical Systems, Springer Verlag, New York, NY, 1997.
[35] D.R. Chialvo, Generic excitable dynamics on a two-dimensional map, Chaos Solitons Fractals 5 (1995) 461–479.
[36] M. Courbage, V.I. Nekorkin, L.V. Vdovin, Chaotic oscillations in a map-based model of neural activity, Chaos 17 (2007) 043109.
[37] B. Cazelles, M. Courbage, M. Rabinovich, Anti-phase regularization of coupled chaotic maps modelling bursting neurons, Europhys. Lett. 56 (2001) 504–509.
[38] C. Aguirre, D. Campos, P. Pascual, E. Serrano, Neuronal behavior with sub-threshold oscillations and spiking/bursting activity using a piecewise linear two-dimensional map, in: Artificial Neural Networks: Biological Inspirations ICANN 2005, Springer, Berlin, Germany, 2005, pp. 103–108.
[39] M. Usher, H.G. Schuster, E. Niebur, Dynamics of populations of integrate-and-fire neurons, partial synchronization and memory, Neural Comput. 5 (1993) 570–586.
[40] H. Soula, G. Beslon, O. Mazet, Spontaneous dynamics of asymmetric random recurrent spiking neural networks, Neural Comput. 18 (2006) 60–79.
[41] B. Cessac, A discrete time neural network model with spiking neurons, J. Math. Biol. 56 (2008) 311–345.
[42] B. Cessac, T. Viéville, On dynamics of integrate-and-fire neural networks with conductance based synapses, Front. Comput. Neurosci. 2 (2008) 311–345.
[43] E.M. Izhikevich, Simple model of spiking neurons, IEEE Trans. Neural Netw. 14 (2003) 1569–1572.
[44] E.M. Izhikevich, Bursting mappings, Internat. J. Bifur. Chaos 14 (2004) 3847–3854.
[45] J. Touboul, Bifurcation analysis of a general class of nonlinear integrate-and-fire neurons, SIAM J. Appl. Math. 68 (2008) 1045–1079.
[46] J.A. Sanders, F. Verhulst, Averaging Methods in Nonlinear Dynamical Systems, in: Applied Mathematical Sciences, vol. 59, Springer, New York, NY, 1985.
[47] J. Rubin, D. Terman, Geometric singular perturbation analysis of neuronal dynamics, in: B. Fiedler (Ed.), Handbook of Dynamical Systems, vol. 2, North-Holland, Amsterdam, 2002, pp. 93–146.
[48] J. Rinzel, G.B. Ermentrout, Analysis of neural excitability and oscillations, in: C. Koch, I. Segev (Eds.), Methods in Neuronal Modeling: From Synapses to Networks, MIT Press, Cambridge, MA, 1989, pp. 135–169.
[49] N.F. Rulkov, Regularization of synchronized chaotic bursts, Phys. Rev. Lett. 86 (2001) 183–186.
[50] N.F. Rulkov, Modeling of spiking-bursting neural behavior using two-dimensional map, Phys. Rev. E 65 (2002) 041922.
[51] B. Ibarz, G. Tanaka, M.A.F. Sanjuán, K. Aihara, Sensitivity versus resonance in simple map-based conductance neuron models, Phys. Rev. E 75 (2007) 041902.
[52] A.L. Shilnikov, N.F. Rulkov, Subthreshold oscillations in a map-based neuron model, Phys. Lett. A 328 (2004) 177–184.
[53] N.F. Rulkov, I. Timofeev, M. Bazhenov, Oscillations in large-scale cortical networks: map-based model, J. Comput. Neurosci. 17 (2004) 203–223.
[54] N.F. Rulkov, M. Bazhenov, Oscillations and synchrony in large-scale cortical network models, J. Biol. Phys. 34 (2008) 279–299.
[55] T. Nowotny, R. Huerta, H.D.I. Abarbanel, M.I. Rabinovich, Self-organization in the olfactory system: one shot odor recognition in insects, Biol. Cybern. 93 (2005) 436–446.
[56] J. Aguirre, E. Mosekilde, M.A.F. Sanjuán, Analysis of the noise-induced bursting-spiking transition in a pancreatic β-cell model, Phys. Rev. E 69 (2004) 041910.
[57] V.I. Nekorkin, L.V. Vdovin, Diskretnaya model" nejronnoj aktivnosti, Izvest. vys. ucheb. zaved. Prikladnaya nelinejnaya dinamika 15 (2007) 36–60.
[58] V.S. Afraimovich, S. Hsu, Lectures on Chaotic Dynamical Systems, in: Studies in Advanced Mathematics, AMS, Providence, RI, 2003.
[59] H. Nagashima, Y. Baba, Introduction to Chaos: Physics and Mathematics of Chaotic Phenomena, Institute of Physics Publishing, Bristol, UK, 1998.
[60] E.M. Izhikevich, Neural excitability, spiking, and bursting, Internat. J. Bifur. Chaos Appl. Sci. Engrg. 10 (2000) 1171–1266.
[61] R. Fitzhugh, Mathematical models of excitation and propagation in nerve, in: H.P. Schwan (Ed.), Biological Engineering, McGraw-Hill, New York, NY, 1969, pp. 1–85.
[62] C. Aguirre, D. Campos, P. Pascual, L. Vázquez, Pattern formation and encoding rhythms analysis on a spiking/bursting neuronal network, Eur. Phys. J. Special Topics 146 (2007) 169–176.
[63] K.S. Cole, R. Guttman, F. Bezanilla, Nerve membrane excitation without threshold, Proc. Natl. Acad. Sci. 65 (1970) 884–891.
[64] G. Matsumoto, K. Aihara, Y. Hanyu, N. Takahashi, S. Yoshizawa, J. Nagumo, Chaos and phase locking in normal squid axons, Phys. Lett. A 123 (1987) 162–166.
[65] F. Pasemann, A simple chaotic neuron, Physica D 104 (1997) 205–211.
[66] H. Tanaka, T. Ushio, S. Kawanami, A high-dimensional chaotic discrete-time neuron model and bursting phenomena, Phys. Lett. A 308 (2003) 41–46.
[67] H. Tanaka, Design of bursting in a two-dimensional discrete-time neuron model, Phys. Lett. A 350 (2006) 228–231.
[68] S.M. Kuva, G.F. Lima, O. Kinouchi, M.H.R. Tragtenberg, A.C.R. da Silva, A minimal model for excitable and bursting elements, Neurocomput. 38–40 (2001) 255–261.
[69] M. Copelli, M.H.R. Tragtenberg, O. Kinouchi, Stability diagrams for bursting neurons modeled by three-variable maps, Physica A 342 (2004) 263–269.
[70] H. Kitajima, T. Yoshinaga, K. Aihara, H. Kawakami, Chaotic bursts and bifurcation in chaotic neural networks with ring structure, Int. J. Bifur. Chaos 11 (2001) 1631–1643.
[71] T.R. Chay, Chaos in a three-variable model of an excitable cell, Physica D 16 (1984) 233–242.
[72] E.M. Harth, T.J. Csermely, B. Beek, R.D. Lindsay, Brain functions and neural dynamics, J. Theoret. Biol. 26 (1970) 93–120.
[73] P.A. Anninos, B. Beek, T.J. Csermely, E.M. Harth, G. Pertile, Dynamics of neural structures, J. Theoret. Biol. 26 (1970) 121–148.
[74] A. Rapoport, Ignition phenomena in random nets, Bull. Math. Biol. 14 (1952) 35–44.
[75] D.R. Smith, C.H. Davidson, Maintained activity in neural nets, J. ACM 9 (1962) 268–279.
[76] V.B. Mountcastle, Modality and topographic properties of single neurons of cat's somatic sensory cortex, J. Neurophysiol. 20 (1957) 408–434.
[77] D. Hubel, T. Wiesel, Receptive fields binocular interaction and functional architecture in the cat's visual cortex, J. Physiol. 160 (1962) 106–154.
[78] E. Fournou, P. Argyrakis, B. Kargas, P.A. Anninos, A gaussian approach to neural nets with multiple memory domains, Conn. Sci. 7 (1995) 331–340.
[79] A. Kotini, P.A. Anninos, Dynamics of noisy neural nets with chemical markers and gaussian-distributed connectivities, Conn. Sci. 9 (1997) 381–404.
[80] J. Lücke, C. von der Malsburg, Rapid processing and unsupervised learning in a model of the cortical macrocolumn, Neural Comput. 16 (2004) 501–533.
[81] P. Anninos, M. Kokkinidis, A neural net model for multiple memory domains, J. Theoret. Biol. 109 (1984) 95–110.
[82] G. Lee, G.S. Yi, The chaotic netlet map, in: Advances in Neural Networks, vol. 4492, ISNN 2007, Berlin, 2007, pp. 104–112.
[83] N.H. Farhat, Corticonic models of brain mechanisms underlying cognition and intelligence, Phys. Life Rev. 4 (2007) 223–252.
[84] R. Pashaie, N.H. Farhat, Self-organization in a parametrically coupled logistic map network: a model for information processing in the visual cortex, Trans. Neur. Netw. 20 (2009) 597–608.
[85] M. Rubinov, O. Sporns, C. van Leeuwen, M. Breakspear, Symbiotic relationship between brain structure and dynamics, BMC Neurosci. 10 (2009) 55.
[86] R.L. Devaney, An Introduction to Chaotic Dynamical Systems, second edition, Westview Press, Boulder, CO, 2003.
[87] M. Breakspear, J.R. Terry, K.J. Friston, Modulation of excitatory synaptic coupling facilitates synchronization and complex dynamics in a biophysical model of neuronal dynamics, Network 14 (2003) 703–732.
[88] R.J. Butera, J. Rinzel, J.C. Smith, Models of respiratory rhythm generation in the pre-bötzinger complex. I. Bursting pacemaker neurons, J. Neurophysiol. 82 (1999) 382–397.
[89] M. Bazhenov, N.F. Rulkov, J. Fellous, I. Timofeev, Role of network dynamics in shaping spike timing reliability, Phys. Rev. E 72 (2005) 041903.
[90] M.J.E. Richardson, N. Brunel, V. Hakim, From subthreshold to firing-rate resonance, J. Neurophysiol. 89 (2003) 2538–2554.

[91] H. Korn, P. Faure, Is there chaos in the brain? II. Experimental evidence and related models, C. R. Biologies 326 (2003) 787–840.
[92] G. Zheng, A. Tonnelier, Chaotic solutions in the quadratic integrate-and-fire neuron with adaptation, Cogn. Neurodyn. 3 (2009) 197–204.
[93] J.L. Hindmarsh, R.M. Rose, A model of neuronal bursting using three coupled first order differential equations, Proc. R. Soc. Lond. B 221 (1984) 87–102.
[94] A.L. Shilnikov, N.F. Rulkov, Origin of chaos in a two-dimensional map modelling spiking-bursting neural activity, Int. J. Bifur. Chaos 13 (2003) 3325–3340.
[95] J. Guckenheimer, K. Hoffman, W. Weckesser, Numerical computation of canards, Int. J. Bifur. Chaos 10 (2000) 2669–2687.
[96] N. Fenichel, Geometric singular perturbation theory, J. Differential Equations 31 (1979) 53–98.
[97] E. Benoît, J.L. Callot, F. Diener, M. Diener, Chasse au canard, Collect. Math. 31–32 (1981) 37–119.
[98] P. Swain, A. Longtin, Noise in genetic and neural networks, Chaos 16 (2006) 026101.
[99] L.J. Defelice, Introduction to Membrane Noise, Springer, New York, NY, 1981.
[100] C. Koch, Biophysics of Computation: Information Processing in Single Neurons, Oxford University Press, New York, NY, 1999.
[101] R.B. Stein, E.R. Gosen, K.E. Jones, Neuronal variability: noise or part of the signal? Nat. Rev. Neurosci. 6 (2005) 389.
[102] D.R. Chialvo, A.V. Apkarian, Modulated noisy biological dynamics: three examples, J. Stat. Phys. 20 (1993) 375–391.
[103] A. Longtin, A. Bulsara, F. Moss, Time-interval sequences in bistable systems and the noise-induced transmission of information by sensory neurons, Phys. Rev. Lett. 67 (1991) 656–659.
[104] L. Gammaitoni, P. Hänggi, P. Jung, F. Marchesoni, Stochastic resonance, Rev. Modern Phys. 70 (1998) 223.
[105] C.W. Gardiner, Handbook of Stochastic Methods, Springer, Berlin, Germany, 1985.
[106] R.C. Hilborn, A simple model for stochastic coherence and stochastic resonance, Amer. J. Phys. 72 (2004) 528–533.
[107] R.C. Hilborn, R.J. Erwin, Coherence resonance in models of an excitable neuron with noise in both the fast and slow dynamics, Phys. Lett. A 322 (2004) 19–24.
[108] R.C. Hilborn, R.J. Erwin, Fokker-planck analysis of stochastic coherence in models of an excitable neuron with noise in both fast and slow dynamics, Phys. Rev. E 72 (2005) 031112.
[109] W. Singer, Neuronal synchrony: a versatile code for the definition of relations? Neuron 24 (1999) 49–65.
[110] P.J. Uhlhaas, W. Singer, Neural synchrony in brain disorders: relevance for cognitive dysfunctions and pathophysiology, Neuron 52 (2006) 155–168.
[111] H.D.I. Abarbanel, M.I. Rabinovich, A. Selverston, M.V. Bazhenov, R. Huerta, M.M. Suschchik, L.L. Rubchinskii, Synchronisation in neural networks, Phys. Usp. 39 (1996) 337–362.
[112] M.P.K. Jampa, A.R. Sonawane, P.M. Gade, S. Sinha, Synchronization in a network of model neurons, Phys. Rev. E 75 (2007) 026215.
[113] D.J. Watts, S.H. Strogatz, Collective dynamics of small-world networks, Nature 393 (1998) 440–442.
[114] D.Q. Wei, X.S. Luo, Ordering spatiotemporal chaos in discrete neural networks with small-world connections, Europhys. Lett. 77 (2007) 68004.
[115] Q.Y. Wang, Z. Duan, M. Perc, G. Chen, Synchronization transitions on small-world neuronal networks: effects of information transmission delay and rewiring probability, Europhys. Lett. 83 (2008) 50008.
[116] Q.Y. Wang, M. Perc, Z. Duan, G. Chen, Delay-induced multiple stochastic resonances on scale-free neuronal networks, Chaos 19 (2009) 023112.
[117] M. Girvan, M.E.J. Newman, Community structure in social and biological networks, Proc. Natl. Acad. Sci. USA 99 (2002) 7821–7826.
[118] M. Shanahan, Dynamical complexity in small-world networks of spiking neurons, Phys. Rev. E 78 (2008) 041924.
[119] A.K. Seth, Causal connectivity analysis of evolved neural networks during behavior, Network 16 (2005) 35–54.
[120] J. Güémez, M.A. Matías, Synchronous oscillatory activity in assemblies of chaotic model neurons, Physica D 96 (1996) 334–343.
[121] L.M. Pecora, T.L. Carroll, Synchronization in chaotic systems, Phys. Rev. Lett. 64 (1990) 821.
[122] R.E. Mirollo, S.H. Strogatz, Synchronization of pulse-coupled biological oscillators, SIAM J. Appl. Math. 50 (1990) 1645.
[123] N. Masuda, K. Aihara, Synchronization of pulse-coupled excitable neurons, Phys. Rev. E 64 (2001) 051906.
[124] Q.Y. Wang, Q.S. Lu, G.R. Chen, Subthreshold stimulus-aided temporal order and synchronization in a square lattice noisy neuronal network, Europhys. Lett. 77 (2007) 10004.
[125] H. Chen, J. Zhang, J. Liu, Enhancement of neuronal coherence by diversity in coupled rulkov-map models, Physica A 387 (2008) 1071–1076.
[126] M. Steriade, D.A. Mccormick, Thalamocortical oscillations in the sleeping and aroused brain, Science 262 (1993) 679–685.
[127] M. Bevan, P. Magill, D. Terman, J. Bolam, C. Wilson, Move to the rhythm: oscillations in the subthalamic nucleus-external globus pallidus network, Trends Neurosci. 25 (2002) 525–531.
[128] E. Marder, D. Bucher, Central pattern generators and the control of rhythmic movements, Curr. Biol. 11 (2001) R986–R996.
[129] J. Duarte, L. Silva, J.S. Ramos, The influence of coupling on chaotic maps modelling bursting cells, Chaos Solitons Fractals 28 (2006) 1314–1326.
[130] M. Morse, G.A. Hedlund, Symbolic dynamics, Am. J. Math. 60 (1938) 815–866.
[131] J.C.A. de Pontes, R.L. Viana, S.R. Lopes, C.A.S. Batista, A.M. Batista, Bursting synchronization in non-locally coupled maps, Physica A 387 (2008) 4417–4428.
[132] G. de Vries, Bursting as an emergent phenomenon in coupled chaotic maps, Phys. Rev. E 64 (2001) 051914.
[133] G. de Vries, From spikers to bursters via coupling: help from heterogeneity, Bull. Math. Biol. 63 (2001) 371–391.
[134] L.M. Pecora, T.L. Carroll, Master stability functions for synchronized coupled systems, Phys. Rev. Lett. 80 (1998) 2109–2112.
[135] G. Tanaka, B. Ibarz, M.A.F. Sanjuán, K. Aihara, Synchronization and propagation of bursts in networks of coupled map neurons, Chaos 16 (2006) 013113.
[136] M.V. Ivanchenko, G.V. Osipov, V.D. Shalfeev, J. Kurths, Network mechanism for burst generation, Phys. Rev. Lett. 98 (2004) 108101.
[137] M.V. Ivanchenko, G.V. Osipov, V.D. Shalfeev, J. Kurths, Phase synchronization in ensembles of bursting oscillators, Phys. Rev. Lett. 93 (2004) 134101.
[138] C.A.S. Batista, A.M. Batista, J.A.C. de Pontes, R.L. Viana, S.R. Lopes, Chaotic phase synchronization in scale-free networks of bursting neurons, Phys. Rev. E 76 (2007) 016218.
[139] C.A.S. Batista, A.M. Batista, J.C.A. de Pontes, S.R. Lopes, R.L. Viana, Bursting synchronization in scale-free networks, Chaos Solitons Fractals 41 (2009) 2220–2225.
[140] J.Y.K. Lee, D. Kondziolka, Thalamic deep brain stimulation for management of essential tremor, J. Neurosurgery 103 (2005) 400–403.
[141] L.B. Good, S. Sabesan, S.T. Marsh, K. Tsakalis, D. Treiman, L. Iasemidis, Control of synchronization of brain dynamics leads to control of epileptic seizures in rodents, Int. J. Neural Syst. 19 (2009) 173–196.
[142] M. Rosenblum, A. Pikovsky, Delayed feedback control of collective synchrony: an approach to suppression of pathological brain rhythms, Phys. Rev. E 70 (2004) 041904.
[143] M. Rosenblum, N. Tukhlina, A. Pikovsky, L. Cimponeriu, Delayed feedback suppression of collective rhythmic activity in a neuronal ensemble, Int. J. Bifur. Chaos 16 (2006) 1989–1999.
[144] C.A.S. Batista, S.R. Lopes, R.L. Viana, A.M. Batista, Delayed feedback control of bursting synchronization in a scale-free neuronal network, Neural Netw. 23 (2010) 114–124.
[145] G.V. Osipov, M.V. Ivanchenko, J. Kurths, B. Hu, Synchronized chaotic intermittent and spiking behavior in coupled map chains, Phys. Rev. E 71 (2005) 056209.
[146] M.V. Ivanchenko, G.V. Osipov, V.D. Shalfeev, J. Kurths, Phase synchronization of chaotic intermittent oscillations, Phys. Rev. Lett. 92 (2004) 134101.
[147] H. Cao, M.A.F. Sanjuán, A mechanism for elliptic-like bursting and synchronization of bursts in a map-based neuron network, Cogn. Process. (2008).
[148] K. Kaneko, I. Tsuda, Chaotic itinerancy, Chaos 13 (2003) 926–936.
[149] H.P.C. Robinson, N. Kawai, Injection of digitally synthesized synaptic conductance transients to measure the integrative properties of neurons, J. Neurosci. Methods 49 (1993) 157–165.
[150] A.A. Sharp, M.B. O'neil, L.F. Abbott, E. Marder, The dynamic clamp: artificial conductances in biological neurons, Trends Neurosci. 16 (1993) 389–394.
[151] F.K. Skinner, N. Kopell, E. Marder, Mechanisms for oscillation and frequency control in reciprocally inhibitory model neural networks, J. Comput. Neurosci. 1 (1994) 69–87.

[152] D. Somers, N. Kopell, Rapid synchronization through fast threshold modulation, Biol. Cybern. 68 (1993) 393–407.
[153] B. Ibarz, H. Cao, M.A.F. Sanjuán, Bursting regimes in map-based neuron models coupled through fast threshold modulation, Phys. Rev. E 77 (2008) 051918.
[154] X. Shi, Q. Lu, Burst synchronization of electrically and chemically coupled map-based neurons, Physica A 388 (2009) 2410–2419.
[155] I. Franović, V. Miljković, Power law behavior related to mutual synchronization of chemically coupled map neurons, Euro. Phys. J. B 76 (2010) 613–624.
[156] I. Franović, V. Miljković, The effects of synaptic time delay on motifs of chemically coupled rulkov model neurons, Commun. Nonlinear Sci. Numer. Simul. 16 (2011) 623–633.
[157] H. Cao, B. Ibarz, Hybrid discrete-time neural networks, Phil. Trans. Royal Soc. A 368 (2010) 5071–5086.
[158] M. Tsodyks, K. Pawelzik, H. Markram, Neural networks with dynamic synapses, Neural Comput. 10 (1998) 821–835.
[159] P. Meyrand, M. Moulins, Phylogenetic plasticity of crustacean stomatogastric circuits I. Pyloric patterns and pyloric circuit of the shrimp palaemon serratus, J. Exp. Biol. 138 (1988) 107–132.
[160] J.M. Casado, Transient activation in a network of coupled map neurons, Phys. Rev. Lett. 91 (2003) 208102.
[161] J.M. Casado, B. Ibarz, M.A.F. Sanjuán, Winnerless competition in networks of coupled map neurons, Mod. Phys. Lett. B 18 (2004) 1347–1367.
[162] B. Ibarz, J.M. Casado, M.A.F. Sanjuán, K. Aihara, Patterns in inhibitory networks of simple map neurons, Phys. Rev. E 75 (2007) 041911.
[163] C. van Vreeswijk, H. Sompolinsky, Chaos in neuronal networks with balanced excitatory and inhibitory activity, Science 274 (1996) 1724–1726.
[164] V.L. Girko, Circular law, Theory Probab. Appl. 29 (1984) 694–706.
[165] M. Bazhenov, N.F. Rulkov, I. Timofeev, Effect of synaptic connectivity on long-range synchronization of fast cortical oscillations, J. Neurophysiol. 100 (2008) 1562–1575.
[166] V.N. Belykh, I.V. Belykh, M. Hasler, Connection graph stability method for synchronized coupled chaotic systems, Physica D 195 (2004) 159–187.
[167] X. Sun, Q. Lu, J. Kurths, Correlated noise induced spatiotemporal coherence resonance in a square lattice network, Physica A 387 (2008) 6679–6685.
[168] E.M. Izhikevich, Polychronization: computation with spikes, Neural Comput. 18 (2006) 245–282.
[169] H. Markram, J. Lubke, M. Frotscher, B. Sakmann, Regulation of synaptic efficacy by coincidence of postsynaptic aps and epsps, Science 275 (1997) 213–215.
[170] G. Bi, M. Poo, Synaptic modification of correlated activity: Hebb's postulate revisited, Ann. Rev. Neurosci. 24 (2001) 139–166.
[171] D. Hebb, The Organization of Behavior, John Wiley & Sons, New York, NY, 1949.
[172] S. Song, K.D. Miller, L.F. Abbott, Competitive hebbian learning through spike-timing-dependent synaptic plasticity, Nat. Neurosci. 3 (2000) 919–926.
[173] M.A. Whittington, R.D. Traub, N. Kopell, B. Ermentrout, E.H. Buhl, Inhibition-based rhythms: experimental and mathematical observations on network dynamics, Int. J. Psychophysiol. 38 (2000) 315–336.
[174] E.M. Izhikevich, J.A. Gally, G.M. Edelman, Spike-timing dynamics of neuronal groups, Cereb. Cortex 14 (2004) 933–944.
[175] E.M. Izhikevich, G.M. Edelman, Large-scale model of mammalian thalamocortical systems, Proc. Natl. Acad. Sci. USA 105 (2008) 3593–3598.
[176] N. Masuda, H. Kori, Formation of feedforward networks and frequency synchrony by spike-timing-dependent plasticity, J. Comput. Neurosci. 22 (2007) 327–345.
[177] P. Gong, Evolution to a small-world network with chaotic units, Europhys. Lett. 67 (2004) 328–333.
[178] M.E.J. Newman, Modularity and community structure in networks, Proc. Natl. Acad. Sci. USA 103 (2006) 8577–8582.
[179] I. Timofeev, F. Grenier, M. Bazhenov, T.J. Sejnowski, M. Steriade, Origin of slow cortical oscillations in deafferented cortical slabs, Cereb. Cortex 10 (2000) 1185–1199.
[180] E.M. Izhikevich, Dynamical Systems in Neuroscience: The Geometry of Excitability and Bursting, The MIT Press, Cambridge, MA, 272–319.
[181] B. Cazelles, Synchronization of a network of chaotic neurons using adaptive control in noisy environments, Int. J. Bifur. Chaos 8 (1998) 1821–1830.
[182] T. Kumagai, R. Hashimoto, M. Wada, Learning of limit cycles in discrete-time neural network, Neurocomputing 13 (1996) 1–10.
[183] E.M. Izhikevich, Solving the distal reward problem through linkage of stdp and dopamine signaling, Cereb. Cortex 17 (2007) 2443–2452.
[184] W. Schultz, Predictive reward signal of dopamine neurons, J. Neurophysiol. 80 (1998) 1–27.
[185] R.S. Sutton, A.G. Barto, Reinforcement Learning: An Introduction (Adaptive Computation and Machine Learning), The MIT Press, Cambridge, MA, 1998.
[186] W.X. Pan, R. Schmidt, J.R. Wickens, B.I. Hyland, Dopamine cells respond to predicted events during classical conditioning: evidence for eligibility traces in the reward-learning network, J. Neurosci. 25 (2005) 6235–6242.
[187] W. Schultz, P. Dayan, P.R. Montague, A neural substrate of prediction and reward, Science 275 (1997) 1593–1599.
[188] J.E.R. Staddon, Y. Niv, Operant conditioning, Scholarpedia 3 (2008) 2318.
[189] G. Hinton, T. Sejnowski, Unsupervised Learning, The MIT Press, Cambridge, MA, 1999.
[190] T. Nowotny, Sloppy engineering and the olfactory system of insects, in: Biologically inspired signal processing for chemical sensing, Springer, New York, NY, 2009, pp. 3–32.
[191] B. Raman, J. Joseph, J. Tang, M. Stopfer, Temporally diverse firing patterns in olfactory receptor neurons underlie spatiotemporal neural codes for odors, J. Neurosci. 30 (2010) 1994–2006.
[192] G. Laurent, M. Stopfer, R.W. Friedrich, M.I. Rabinovich, H.D.I. Abarbanel, Odor encoding as an active, dynamical process: experiments, computation, and theory, Annu. Rev. Neurosci. 24 (2001) 263–297.
[193] M. Garcia-Sanchez, R. Huerta, Design parameters of the fan-out phase of sensory systems, J. Comput. Neurosci. 15 (2003) 5–17.
[194] M. Stopfer, V. Jayaraman, G. Laurent, Intensity versus identity coding in an olfactory system, Neuron 39 (2003) 991–1004.
[195] C. Assisi, M. Stopfer, G. Laurent, M. Bazhenov, Adaptive regulation of sparseness by feedforward inhibition, Nat. Neurosci. 10 (2007) 1176–1184.
[196] H. Nakahara, K. Doya, Near-saddle–node bifurcation behavior as dynamics in working memory for goal-directed behavior, Neural Comput. 10 (1998) 113–132.
[197] S. Nolfi, D. Parisi, J.L. Elman, Learning and evolution in neural networks, Adapt. Behav. 3 (1994) 5–28.
[198] D. Ashlock, Evolutionary Computation for Modeling and Optimization, Springer Verlag, New York, NY, 2006.
[199] F.C. Hoppensteadt, E.M. Izhikevich, Weakly Connected Neural Networks, Springer, New York, NY, 1997.
[200] J. Ayers, N. Rulkov, Controlling biomimetic underwater robots with electronic nervous systems, in: Bio-mechanisms of Swimming and Flying, Springer, Japan, 2008, pp. 295–306.
[201] J. Ayers, N. Rulkov, D. Knudsen, Y. Kim, A. Volkovskii, A. Selverston, Controlling underwater robots with electronic nervous systems, Appl. Bionics Biomech. 7 (2010) 57–67.
[202] M. Shanahan, A spiking neuron model of cortical broadcast and competition, Consciousness Cognition 17 (2008) 288–303.
[203] B.J. Baars, The conscious access hypothesis: origins and recent evidence, Trends Cogn. Sci. 6 (2002) 47–52.
[204] S. Dehaene, C. Sergent, J. Changeux, A neuronal network model linking subjective reports and objective physiological data during conscious perception, Proc. Natl. Acad. Sci. USA 100 (2003) 8520–8525.
[205] E.M. Izhikevich, Which model to use for cortical spiking neurons? IEEE Trans. Neural Netw. 15 (2004) 1063–1070.